A study of Collective effects and Dark state based localization protocols in cold atoms.

by

Diptaranjan Das

A dissertation submitted in partial fulfillment of the requirements for the degree of

Doctor of Philosophy

(Physics)

at the

UNIVERSITY OF WISCONSIN, MADISON

2020

Date of final oral examination: 05/08/2020

The dissertation is approved by the following members of the Final Oral Committee:

Prof. Deniz Yavuz, Physics

Prof. Mark Saffman, Physics

Prof. Shimon Kolkowitz, Physics

Prof. Randall Goldsmith, Chemistry

To my parents

Abstract

Diptaranjan Das

A study of Collective effects and Dark state based
localization protocols in cold atoms.

We study collective effects, namely subradiance and superradiance in dilute atomic samples. Previous experiments focused on the weak excitation regime where a single photon is absorbed by an ensemble and most theoretical studies have been carried out in this regime. We explore collective effects when there are multiple excitations in the cloud and detect signatures of a fast initial decay (faster than single atom decay rate) followed by a slow decay at longer times. We observe a clear signature of a superradiance to subradiance transition. We use a combination of fast photodiodes and photon counters to observe the probe pulse and fluorescence signal respectively. We ensure fast turnoff of the probe light using tight focusing in Acousto-Optic Modulators. The main challenges were low signal to noise ratio, long integration times that required laboratory conditions to be stable over several hours, precise time resolved measurements and a lack of theoretical models for collective effects beyond the single photon excitation limit in an extended sample. In the later chapters we discuss coherent effects in cold atoms under the conditions of Electromagnetically induced transparency (EIT). Specifically, we discuss experimental demonstration of subwavelength localization of atomic excitation by using Electromagnetically induced transparency in Rubidium atoms in a dipole trap. The experiment demonstrates the localization of excitation between hyperfine ground states of ^{87}Rb atoms to as small

as $\lambda/13$ wide spatial regions using ultracold atoms trapped in a dipole trap. The localization is achieved by combining a spatially varying coupling laser (standing-wave) with the intensity dependence of EIT. To measure the spatial extent of excitation region we use an auto-correlation method where we perform two EIT sequences separated by a time delay, during which we move the standing wave. A scheme and numerical analysis of extending the localization protocol to implement quantum gates with subwavelength resolution is discussed.

Acknowledgements

The person to whom I owe the greatest thanks is my advisor, Prof. Deniz Yavuz. He has been of great help and inspiration both on academic as well as non-academic fronts. I am really grateful to him for his help, patience and support throughout my graduate career. I would also like to thank my colleagues in Yavuz Lab Jared Miles who was immensely helpful in early stages of my project They have helped me in a lot of things, including carrying out the experiments, the analysis of which forms a major part of the thesis. Dr. Ben Lemberger, a theorist was involved in several theoretical collaborations which form a part of the thesis. I'd like to thank other labmates Nick, Josh Zach, Josh, Zach, David for organizing weekly lab lunch. I've received help, at various stages, from students and postdocs in Saffman and Walker labs. I am also grateful to Mr. Billy Gates at the electronics shop for his help and everyone at the physics machine shop.

Courses at UW Madison have been a great intellectual experience though I have to admit I've been pushed to my limits at times. I am indebted to Dr. A. Chubukov, Dr. Lisa Everett, Dr. Bruch, Dr. Chung ,Dr. Hashimoto, Dr. Perkins and Dr. Wolfe my supervisor Prof. Yavuz for their efforts in teaching their respective courses.

Teaching at UW Madison presented a fair amount of challenges. Dr. Jim Reardon have been very helpful at several stages of my graduate career, helping me become better at teching. I learned a lot from Prof. Peter Timbe, Prof. Nossal and several other Professors for whom I was a TA.

I'm also grateful for Renee Lekfow, Rita Knox, Aimee Lekfow and Ann Austin for their help.

I would like to thank Prof. Prasanta Panigrahi, Prof. Chiranjib Mitra and Prof. Bhavtosh Bansal for their help during my stay at IISER Kolkata

Last but not the least I've to thank all my friends for the beautiful (though turbulent) years in Madison and my parents for their patient support.

Contents

List of Figures

Chapter 1

Introduction

The field of quantum technology has seen great progress over the last couple of decades. Initially inspired by the idea of simulating quantum systems and the potential of high performance computing that exploits the fundamental nature of the quantum world, the field has expanded into the domains of secure communications, high precision metrology and quantum sensing. Some of these fields have seen rapid progress over the years and are now on the verge of being developed into commercial quantum technologies.

Quantum technologies have their own set of challenges. Issues with scalability and coherence times are well know and there has always been a lot of skepticism among some scholars who believe these issues make the dream of a commercial quantum computing device fundamentally untenable. Although a quantum computer that replaces our home desktop computer is far from reality, a lot of progress in dealing with the issues mentioned above have been made on both theoretical and experimental fronts.

A system where quantum technologies can be studied and implemented is laser cooled neutral atoms. Development of laser cooling technology in late 1980s, initially motivated by the prospect of better spectroscopy, has opened to door to a system with long coherence times in which fast and precise quantum gates can be implemented.

In this thesis we study coherent effects in a cloud of cold neutral atoms in the

context of large scale quantum computing and quantum information processing. We cool ^{87}Rb atoms using standard techniques of laser cooling and trapping. The thesis is divided into two parts. In the first part of the thesis we study collective effects in a cloud of neutral atoms. These effects scale with system size and can lead to decoherence in individual qubits with decoherence rates scaling with system size. We study neutral atoms with collective excitations and observe decay rates and study how they differ from single atom decay rates. It is vital to have an estimate of how these rates vary with system size and the number of excitations as this will lead to an understanding of how qubit dephasing rates depend on these factors. For a large neutral atom quantum computer the scale dependent dephasing can determine how large a quantum computer we can have with neutral atoms in free space. The key results are summarized in Chapter 4. We observe signatures of collective effects, superradiance and subradiance at low optical depths. In the second part of the thesis we study Electromagnetically induced transparency (EIT) in ultracold atoms. We discuss subwavelength localization of excitations and a scheme to implement quantum gate with subwavelength resolution. The quantum gate and localization schemes are based on what we call the 'Dark state' of the system. A three level system, with two metastable ground states and an excited state can be adiabatically driven to a superposition of the ground states. This is known as the dark state because the quantum state of the atom has no component in the excited state and is hence immune to errors due to spontaneous emission. The superposition has a nonlinear dependence on the beam intensities, a feature that is exploited in localization experiments described in the thesis. The key experimental results in this section is the demonstration of excitations localized in spatial extent of $\lambda/13$ using the dark state and a spatially varying coupling laser.

The organization of the rest of the thesis is as follows:

Part I:

Chapter 2:

We describe the MOT system in our lab, creation of cold atomic ensemble and optical dipole traps using standard techniques. This is our experimental test-bed. A detailed description of the laser cooling and trapping setup in our lab is discussed. We also discuss a non-conventional MOT to implement a high N.A imaging setup for single atom imaging.

Chapter 3:

In this chapter we describe experiments on collective effects carried out in the MOT. We carry out our experiments in the dilute sample regime where the optical depth of the sample is of the order of ~ 1. To put things in perspective spatially the separation between atoms in the spherical cloud is, on average, approximately 5λ. This is much larger than the Dicke limit in which several atoms are placed within a wavelength It is also much more dilute than recent experiments in the Kaiser group that had atoms separated by λ. This is a regime that has not been explored before as previous studies have focused on a weakly excited and relatively dense sample with optical depths of the order of 40 and larger.

Chapter 4:

We dive a bit deeper into the theory of collective effects and how it relates to our experiments. We discuss other effects like directional emission that are interesting future directions for experimental studies. First, we discuss the well studied Coupled Dipole model that has been successful in describing collective effects in the single excitation limit. For our experiments we needed to move beyond the single excitation limit and this leads to a very complicated and intractable many body problem. We discuss our heuristic model briefly introduced in the previous chapter. We also briefly discuss the interesting effect of directional emission though we do not perform any experiments.

In the rest of the thesis we switch gears to a different subject that we studied in our lab prior to our work on subradiance. The details are discussed in chapter 6 which introduces the subject.

Part II:

Chapter 5:

Introduces part II.

Chapter 6:

In this chapter we introduce the subject of EIT (Electromagnetically induced transparency) and discuss possible applications in coherent quantum control. We discuss progress towards implementing EIT/dark state based qubit addressing, gate implementation and localized readout scheme. Experimental results and strategies are discussed. Simulations and theoretical schemes are analyzed.

Chapter 7:

We discuss theoretical and numerical studies of quantum gates with nanoscale resolution in cold atoms. The dark state of EIT and it's nonlinear dependence on the beam intensities can exploited to implement gates with subwavelength resolution. We describe a phase gate protocol that applies a phase on a qubit in an array of neutral atom qubits. The key feature of this protocol is its operation with subwavelength spatial resolution and minimal error due to spontaneous emission. We discuss experimental progress and strategies to implement such a gate in our system.

Chapter 8:

An experiment to localize atomic excitation with subwavelength resolution if discussed. This experiment can, moving forward, be extended to an atomic qubit array to implement quantum gate protocol discussed in the previous chapter.In this chapter we describe the experimental demonstration of localization of excitation between hyperfine ground states of ^{87}Rb atoms to as small as $\lambda/13$ wide spatial regions. We

use ultracold atoms trapped in a dipole trap and utilize electromagnetically induced transparency (EIT) for the atomic excitation.

Chapter 2

Part I: Introduction to collective effects

2.1 Collective effects in spontaneous emission.

Collective effects on rates of spontaneous decay of radiation in an ensemble has been studied over the past several decades both theoretically and experimentally. In 1954 Robert Dicke published his seminal work on Coherence in Spontaneous emission in which he made an elegant application of group theory and angular momentum algebra of quantum mechanics to treat a dense collection of N-emitters as a single quantum system. By treating the number of atoms in the system as the total angular momentum and the difference between the number of excited atoms and the number of ground state atoms as the Z-component of the total angular momentum, he predicted states of the system radiating faster than a single atom decay rate. The rate of decay can be shown to be proportional to N^2 and not N as in the case of independent decay. Dicke coined the term "super-radiant" to describe the enhanced rate of emission. In the same paper he predicted states which does not radiate at all, "subradiant" states that are equivalent to an even number of classical dipoles radiating perfectly out of phase with each other and hence interfering destructively resulting in zero electric

field. The key point was the atoms being indistinguishable, clumped together in a gas of dimensions smaller than the wavelength of light making them fundamentally indistinguishable due to the Heisenberg Uncertainty Principle. The spacing between atoms were much smaller than the wavelength so if a radiated photon from the sample is detected it is impossible to determine which atom emitted the photon. This is a key factor in the analysis of the problem as this allows to treat the ensemble as a large atom with several levels of excitation.

Until recently the subject of subradiance did not receive much attention. It is understandable, the state does not couple to radiation fields and does not offer the richness in spatio-temporal emission profiles of a superradiant state and experimentally it is also very difficult to observe as it requires maintaining positions of emitters for long timescales.

As mentioned above, in the Dicke limit the superradiant state can be thought of a collection of dipoles oscillating in phase and subradiance can be thought of dipoles oscillating out of phase. Beyond the Dicke limit this simplified picture does not hold though subradiant states can be thought of dipoles interfering destructively leading to reduced emission. Beyond the Dicke limit collective states are formed by complicated superpositions of atomic states with complex phases that depends on relative position of atoms. Long lived states are therefore susceptible to dephasing by relative changes in atomic position induced by motion. We show in chapter 5 that collective effects depend on relative separation between atoms in an ensemble, i.e a term in the Hamiltonian that goes as $\sim \sum_{ij} 1/|r_i - r_j|$, with $|r_i - r_j|$ being the spacing between atoms i and j. Though the actual eigenstates are difficult to compute it is clear that atomic motion over long time scales will lead to dephasing. In our studies of long lived states, we are therefore limited by motional dephasing rates. An ensemble of cold atoms has limited atomic motion over the timescale of microseconds, thereby maintaining coherence of collective states over a longer period of time.

Our experiments are motivated by results in the theoretical analysis of the problem beyond the Dicke limit, in the context of quantum computing [12]. It was believed that collective effects are prominent only in very dense ensembles and with good reason. The term driving collective effects, $\sim \sum_{ij} 1/|r_i - r_j|$, does seem to become weaker in the dilute regime. However if we scale the system to a larger size we increase the number of terms in the summation and this leads to prominent collective effects even in a dilute sample. For 3-D geometries for a large enough sample this the errors induced by dephasing can no longer be corrected by standard error correction codes. The collective decay rates are a measure of this unwanted environment-system coupling that scales with the system size as well as the number of excitations. We must, therefore have an estimate of this effect to have an understanding of collective dephasing in a neutral atom qubit array. Our experiments are an attempt to measure these rates, how they scale with system size and number of excitations in the ensemble. We use standard atomic physics techniques to isolate a two level system in ^{87}Rb atomic species in a Magneto-optical Trap (MOT). Excitations are created by a beam close to resonance.

In important prior work: collective decay effects have been studied experimentally in a wide range of physical systems such as cold molecules [13], a system of two trapped ions [14], on multi-level transitions in hot Gallium atoms [15], in cold atoms at the vicinity of a single mode nanofiber [16], and in planar metamaterial arrays [17]. Subradiant atomic momentum states were recently observed in a Bose-Einstein Condensate (BEC) [18]. Studies of superradiant emission have been carried out in cold atoms in the weak excitation limit [19, 10, 20] as well as in diamond nanocrystals [21] and hybrid solid state devices [22] where it is possible to study the system in the Dicke limit. Recently switching between superradiant and subradiant states was demonstrated in a 10-qubit superconducting circuit [23]. With regard to recent theoretical work, most of these studies have focused on the weak excitation limit

where a macroscopic two level atomic ensemble absorbs a single photon [24, 25, 27, 28, 36, 31, 32, 33, 34, 35, 37, 29, 30, 26, 38]. Even though this restricts the problem to a small subspace of the total Hilbert space there are several interesting effects that can be explored, for example, directional emission [24, 25], photon localization [26], and collective Lamb shift [27, 28]. With subradiant states being analogous to decoherence free subspaces, exploitation of subradiant states and tuning between superradiant and subradiant states can have applications in quantum memory devices and quantum information processing [39, 40]. This has inspired a lot of work in studying subradiance in artificial structures like atomic arrays and with modified environments as in a cavity [41, 42, 43, 44, 45, 46, 47, 48, 49, 50, 51]. Other studies of cooperative emission include an analysis by the 'Polarium model' [52], a study of spatial profile of subradiance [53], emission characteristics of entangled sources [54], and a recent analysis of many atom emission by renormalized perturbation theory [55].

Chapter 3

Experimental setup

3.1 Laser Cooled atoms

For our experiments we cool atoms to temperatures close to absolute zero using techniques discussed below. So why do we need cold atoms and how does it help in our studies? A vapour of alkali metal will have a velocity distribution dictated by the Maxwell-Boltzman distribution, which, at standard room temperatures leads to Doppler broadening of the atomic spectra as well as fast dephasing of collective states. Coherent quantum state preparation becomes impossible. Ultracold atoms are slow and atomic motion is minimal over the timescales in which we conduct our experiments. State preparation can be carried out by frequency stabilised lasers. The slow atomic motion means atomic separation remains relatively stable over long timescales. Stability and coherence in long lived collective states (subradiant states) require relative separation of atoms in the cloud to remain constant over timescales that are long compared to atomic decay rates, allowing us to measure decay rates of subradiant states. Experiments described in Part II require trapping of atoms in optical dipole trap. Dipole traps require atoms to be laser cooled. The slow atomic motion enables us to carry out experiments that require precise spatial positioning of atoms relative to a laser standing wave. For this atomic motion over the timescales

of the experiment and measurement needs to be negligible, which is the case for laser cooled atoms in a dipole trap.

3.2 Magneto-optical trap (MOT)

The technology of laser cooling and trapping was implemented in late 1980s.The apparatus composed of counter-propagating Laser beams directed into a vacuum chamber containing a gas of the material to be trapped and cooled. The key idea behind a MOT is Doppler cooling and magnetic trapping. The apparatus has become commonplace as a gas of atoms, or now molecules cooled to extremely low temperatures are a valuable test-bed for studying quantum phenomena. In this chapter a very brief pedagogical description of the experimental setup is given, details regarding the physics of Laser cooling and trapping can be found in Metcalf's book on the subject [2].

3.2.1 Doppler cooling

Consider an atom having two energy levels (for now, the multilevel structure is going to be vital in sub-Doppler cooling and magnetic trapping). The atom can absorb radiation at a frequency $E/(\hbar)$, where E is the energy splitting and $\hbar$ is the Planck's constant divided by 2π. This is known as the resonance frequency of the system. However, if the atom is in motion it will see a Doppler shifted frequency, i.e a frequency lower or higher than the radiation source depending on whether the atom is moving away from or towards the direction of the beam respectively. Therefore by tuning the frequency of the source to a value less than the resonance frequency of the atom we can selectively address a velocity group that is moving in the direction of the beam as these group of atoms will see a beam closer to the resonance frequency and is thereby more likely to absorb a photon. Conservation of momentum dictates that

on absorption the atom will experience a recoil opposing it's motion, thereby slowing it down. Eventually the atom will emit the absorbed photon spontaneously over a characteristic timescale. This emission is isotropic and is accompanied by a recoil in a random direction. Over several cycles of absorption and emission, with absorption being in a specific direction and emission being isotopic, the atom experiences slowing down on average. Using this principle three pairs of counter-propagating beams, over several cycles of absorption and emission will cool an ensemble of atoms. These beams are red detuned from atomic resonance to ensure the atoms experience a recoil opposing it's motion. Laser cooling produces a compression in classical phase space with the energy from the atoms gradually transferred to the radiation field by the isotropic spontaneous emission. This results in the so called optical molasses and the flourescence of the spontaneous emission can be detected to observe these molasses. Next, we discuss spatial confinement using magnetic fields.

3.2.2 Magnetic trapping

Let us consider a real atom, with fine structure, hyperfine splitting and Zeeman sublevels. The Laser beams can be slightly red detuned from hyperfine groung states of an alkali atom. A magnetic field gradient can be used to generate a spatially varying detuning. Since the velocity class addressed by the beams strongly depends on the detuning of the beams this could create a spatial zone around the zero of the magnetic field where the slowest moving atoms are cooled. Atoms away from this trap center are more likely to get a kick towards the center. The atoms are therefore trapped near the zero of the magnetic field. Laser cooling and magnetic trapping are used to cool and trap atoms. The magnetic field is, in practice provided by a spatially varying quadrupole field.

3.2.3 Experimental set-up for MOT I: Conventional MOT.

The MOT apparatus is very standard but for our experiments we use a non-conventional MOT setup for reasons to be discussed later. A lot of details is described in the thesis of Jared Miles [81] who worked on the setup before me. Here I go through a basic description of our MOT setup we use in experiments described in Chapter 9. This is a conventional MOT setup. We have modified the MOT setup for greater optical access. We describe this in a later section (section 2.4). The modified MOT is used in experiments described in Chapter 4.

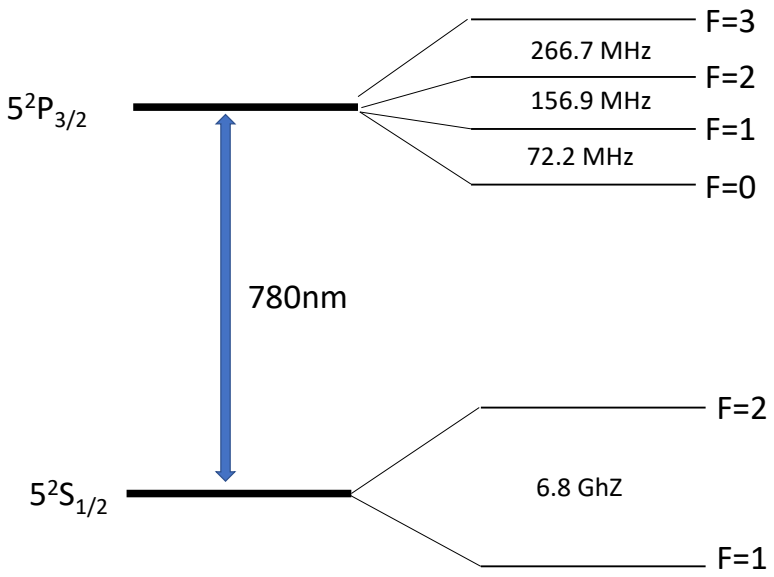

FIGURE 3.1: The relevant energy levels in Rb D2 line.

We trap ^{87}Rb alkali metal in our MOT. The atoms are Doppler cooled in a 14 port stainless steel vacuum chamber using 3 retro reflected beams. A good vacuum is necessary for the MOT. We pump the chamber down to 10^{-9} Torr using an ion pump. The rubidium vapor is obtained from a few grams of Rubidium in a valve controlled flange attached to the chamber.The magnetic field gradient for trapping is generated by a pair of coils in an anti-Helmholtz configuration, each have 250 turns

Beam	Diameter	Power
X	3cm	40mW
Y	3cm	40mW
Z	3cm	25mW

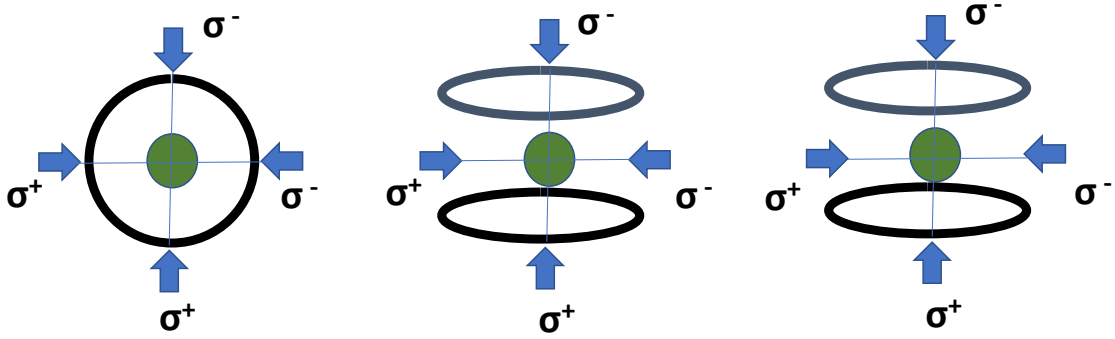

1

FIGURE 3.2: The MOT schematic, the rings indicate the Anti-Helmholtz coils. The vacuum chamber is not shown here.

each with a current of 2.16 A. The coils have their axis alone the vertical axis of the chamber. They are wrapped around the chamber coaxially, ensuring the magnetic field is zero at the center. We also have three pairs of shim coils to have a vanishing magnetic field at the center. The shims drive currents 4.0 A in the z-direction and $\sim$ 2.0 A and 6.0 A in the horizontal axis. The large currents drawn by the shim coils heat up the chamber mildly but does not seem to have an effect on the MOT once it is steady. However the chamber gets magnetized slowly. Because of this we keep the shims on all the time. The MOT cooling beams are 2 cms in diameter and have approximately 50 mW of power in the X and Y direction (saturation parameter $s = I/I_{sat} \sim 4.5$, with I_{sat} being the saturation intensity and I is the intensity of the MOT beam), which we define to be the directions perpendicular to the field generated by the anti-Helmholtz coils. We have a B-field gradient of $\sim$ 20 Gauss/cm with the

splitting being of the order of $\sim .7 * m_F$ MhZ/Gauss. The counter-propagating beam pairs are generated by retro-reflecting the beams. In the z-direction we have a beam with slightly lower power. In the conventional setup described here we have our Z beam orthogonal to the X-Y plane, vertical in the lab frame. This beam has a power of 26 mW ($s = 2.25$), significantly less than the X and Y beams. This is because this beam is alone the MOT gradient field axis. In the non-conventional setup described in section 2.4, however, we do not have a beam orthogonal to the other two beams in our set-up. The window is left free for high numerical aperture optics for imaging and collecting fluorescence. This window is closest to the MOT and has the largest diameter, ideal for imaging a weak signal, as emitted by a single or few atoms. Instead we have our third dimension of cooling from a beam pair 1 cm in diameter coming at an angle of about 30 degrees to the horizontal. This beam has a power of 3 mW ($s = 1.2$). As a result we have significantly less cooling in the z-direction and our MOT does not load a large number of atoms. Though the set-up is not ideal for trapping a large number of atoms, this does not affect our experiments as we work with very dilute samples.

The three pairs of MOT beams are from the output of a 2 W Eagleyard tapered amplifier (TA) seeded by an external cavity diode laser (ECDL) operating at 780 nm. The ECDL consists of a grating mounted on a piezo that forms an external cavity to the diode laser. This is a part of frequency selective feedback to narrow the diode laser linewidth and stabilize the frequency throughout the cooling cycle.

To cool the atoms we use the D2 line of ^{87} Rb. Fig. 3.1 is the energy diagram of the hyperfine levels for D2 line. The 'cooling transition' for the MOT is the $F = 2$ to $F' = 3$ transition of the hyperfine ground states of ^{87} Rb. To stabilize the laser on correct frequency we use a saturated absorption locking technique with a feedback circuit. We lock the laser to a cross over transition between the $F = 1$ and $F' = 3$ energy levels. This locks the frequency to around 212 MHz away from the $F = 1$ and

$F' = 3$ cooling transition. We use an acoustic optical modulator (AOM) to shift the laser to about 20 MHz red-detuned from the cooling transition (for stability we use a double passed AOM that shifts the first order 96 MhZ on one pass). This frequency was found to provide most efficient cooling. The cooling, as described in the first section of this chapter is driven by spontaneous emission. There is a finite probability of atoms being driven to $F' = 2$ level by the cooling lasers. Atoms here can decay to the $F = 1$ ground state which is a dark state. These atoms drop out of the cooling process. We use a separate ECDL is used as repumper and is resonant with the $F = 1$ to $F' = 2$ transition, optically pumping atoms in the $F = 1$ state back to $F = 2$ via the excited state $F' = 2$ (which can decay to both ground states) so they can be addressed by the cooling beams. We overlap the repumper beam with the Y-MOT beam and has a power of 1.1 mW. It is a resonant beam along the same optical path as the Y-MOT beam. The MOT atoms have a temperature of 200 μK, measured by time-of-flight method and has around to 10^6 atoms.

3.2.4 Sub-Doppler cooling

When the first experiments of laser cooling were carried out they were found to be surprisingly cooler than the expected theoretical limit that could be attained by the Doppler cooling process, known as the Doppler limit. The process of cooling involves a "slowing/cooling process" (photon absorption) versus a heating process (spontaneous emission) and the Doppler limit is calculated for a species by assuming a naive two level structure for the atom exchanging energy with the beam and reaching equilibrium. Sub-Doppler cooling was explained in a very elegant paper [1] by a mechanism now known as polarization gradient cooling. The counter-propagating beams, chosen to be circularly polarized because of selection rules in the species, form a polarization gradient. The cooling is caused by frictional processes by the

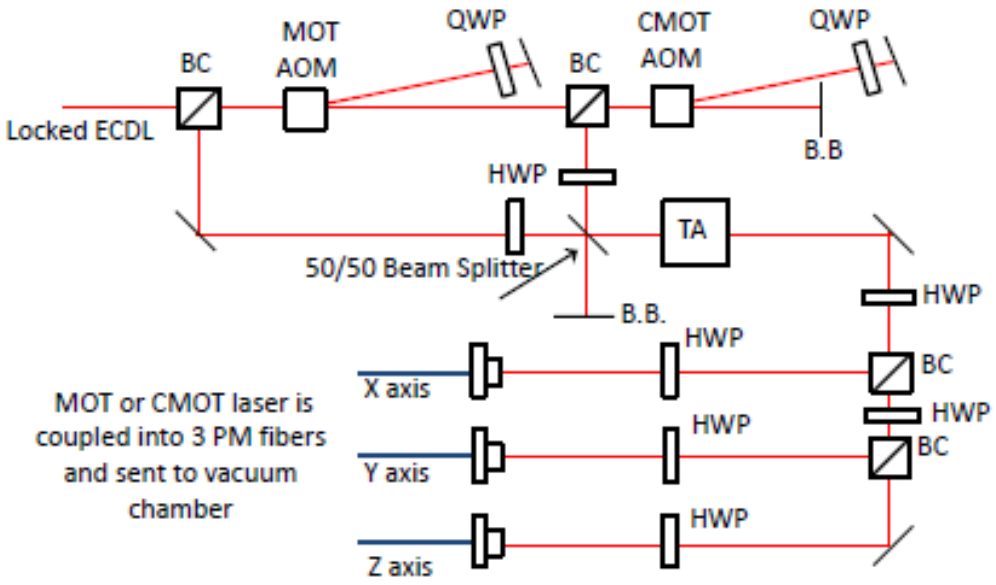

FIGURE 3.3: MOT/CMOT switching scheme: Output of the Locked ECDL is used to seed the 2 W Eagleyard tapered amplifier (TA). The AOMs are used in a double passed configuration with quarter wave plates (QWP) to allow the second pass to travel through the beam cube (BC). The beams are aligned together through a 50/50 beam splitter before entering the TA. Figure from Jared Miles' PhD thesis [81].

interaction of the multilevel atom moving in the polarization gradient. The process is complicated and too involved to be explained in details. We achieve polarization gradient cooling by detuning the beams further from resonance by another 26 Mhz (about 4 times the natural spontaneous decay rate) and reducing the power of the cooling to about a third. The repumper beam is also attenuated by about a factor of 0.4. This gives us a uniform spherical cloud with temperatures of about 40μK. We call this the CMOT (Cool MOT/compressed MOT). We can change the detuning with a separate AOM that is also aligned to the TA. In practice the TA can be seeded by either laser with both beams traveling through a 50/50 beam splitter. We cannot

use the same AOM because the frequency difference is so large that the beam becomes misaligned to the TA. Figure 3.3 shows the double AOM set up that implements the switching between MOT and CMOT settings. We achieve temperatures of 40 μK after a CMOT cooling stage of 40 ms. The atomic spatial distribution if more uniform and a smooth spherical Gaussian cloud of $1/e^2$ radius of 80 mm is obtained.

3.3 FORT

For our main experiments we work with a CMOT. However higher densities and tighter trapping can be achieved by a far off resonant trap (FORT). A FORT is a way of trapping without scattering using a spatially varying intensity of a far detuned laser. A FORT can produce a potential well large enough to trap atoms for seconds without the use of an external magnetic field and without scattering photons. This method of atom trapping can be used to achieve temperatures below 1μK and densities up to 10^{14} atoms/cm^3. The FORT uses the stark shift to create a spatially varying potential along a focused laser beam.

A laser beam that is far off resonant to the a level transition will shift the two energy levels depending on the laser intensity (I) and detuning (Δ) due to the AC Stark effect. We consider a two level system. A red detuned laser beam will Stark shift the ground state to a lower energy level. The shift is proportional to the intensity of the beam. A spatially varying intensity gives rise to a spatially varying energy profile and the gradient of the energy profile gives rise to a conservative force in the direction of maximum intensity.

This energy shift ΔE is defined as

$$\Delta E = \frac{3\pi c^2 \Gamma I}{(2\omega_0^3 \Delta)} \tag{3.1}$$

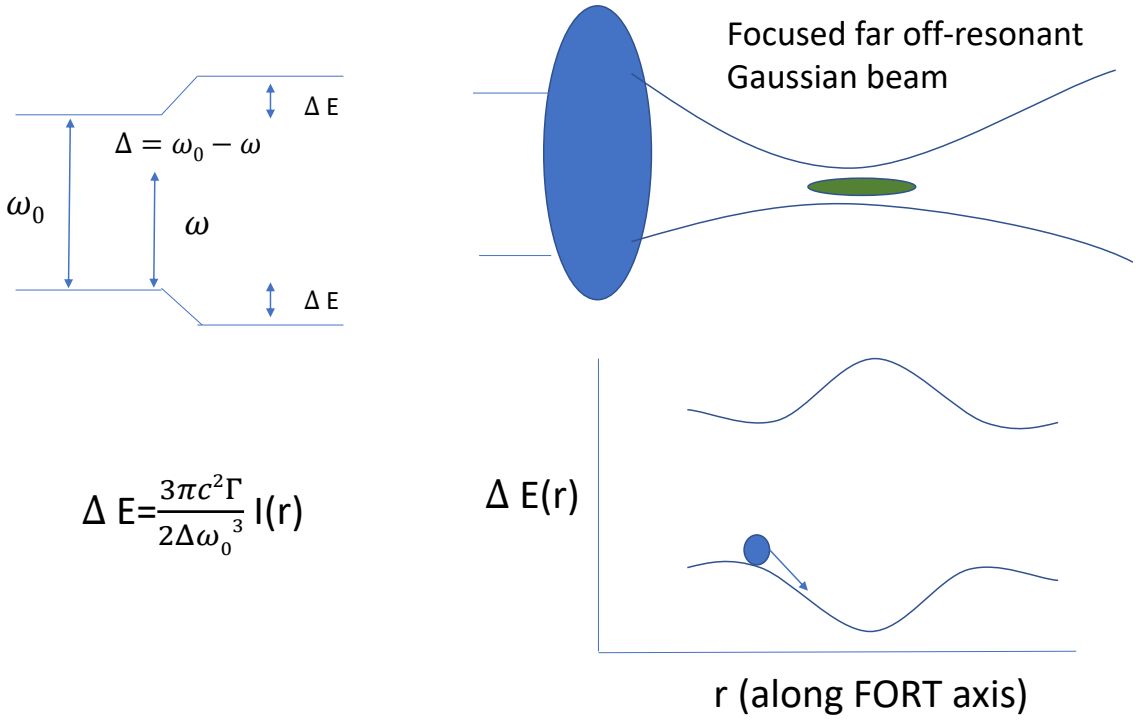

FIGURE 3.4: A red-detuned laser causes both energy levels to shift by an amount ΔE. A focused laser produces a spatially varying Stark shift, with the largest energy shift at the focus of the laser (intensity maxima). Atoms are trapped at the center of the laser.

where ω_0 is the on resonance transition frequency and Γ is the spontaneous emission rate from the upper state. The spatially varying Stark shift is obtained by the spatial variation in intensity $I(r)$. The dipole force is proportional to $\nabla I(r)$. By focusing a 1064 nm, far detuned from the D1 or D2 transition, Gaussian shaped laser, the intensity, and therefore the energy shift, can be made to vary spatially across the laser. This creates a potential well with the lowest energy at the center of the focused laser. Since this energy shift is small, atoms have to be first cooled by the MOT/CMOT cycle described above before being trapped by the FORT. After the MOT cycle the fort laser is turned on in the last 10ms of the CMOT cycle and the FORT laser waist is overlapped with the CMOT cloud. With the FORT beam left on, the MOT beams, repumper, and magnetic fields are turned off. This allows atoms not

trapped in the FORT to leave the zone. When the atoms are initially trapped in the FORT they can be in either the $F = 1$ or $F = 2$ ground state level. Optical pumping methods can be used to transfer the atoms to either of the metastable hyperfine ground states.

The FORT beam is generated from a 2 W tapered amplifier (TA)at 1055 nm that is seeded by a 1064 nm diode laser. The output of the tapered amplifier is not Gaussian and does not focus well to a small spot size. We shape it partially using cylindrical lenses. Due to reasons not well understood, the output is $\sim$ 1.8 W. We aling the output to an AOM that just acts as a fast switch. We pass the first order output of the AOM through a single mode polarization maintaining fiber to produce a smooth TEM00 mode. The fiber output is focused by a achromatic doublet lens of diameter 2 inches and a focal length of 20 cm. The $1/e^2$ radius of the beam waist is 11 μm. We lose a lot power through the fiber and an optical isolator protecting the amplifier from any back reflections. The output beam profile of the TA leads to inefficient coupling to the AOM and the fiber. We have about 150 mW in the dipole trap beam giving a trap depth of 0.1 mK We can, however, end up with a dipole trap with 700 atoms at a temperature of 5 μK.

We are going to discuss localization experiments in Chapter 8. The FORT used for localization experiments was obtained using a standard MOT configuration, not the one mentioned above. The only difference is the Z beam is orthogonal to the X-Y plane and not at an angle. The power in the Z-beam is about 24 mW and it's diameter is 2 cms, same as the other beams. The FORT obtained using the MOT has a larger number of atoms. The higher and more uniform atomic density in the FORT gives a good signal to noise ratio while imaging and also has other advantages. For instance, the B-fields are not necessary in trapping and can hence, be turned off.

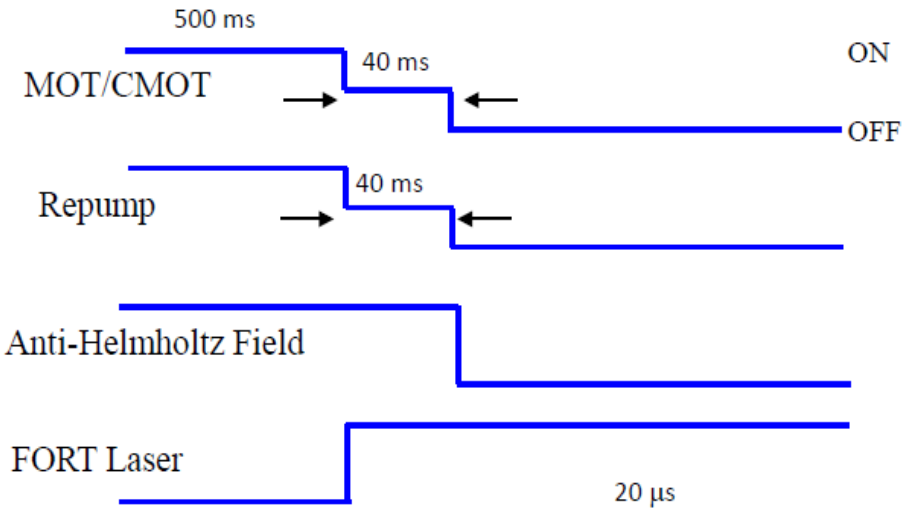

FIGURE 3.5: Pulse timings for the MOT-CMOT-FORT cycle

3.4 Imaging the atoms

In the MOT stage the scattering of MOT beams can be detected to image the atoms in a MOT. Further calibration of the scattering rate and collection efficiency can be used to make an estimate of the number of atoms in the cloud. The CMOT can be imaged in a similar way by illuminating the cloud with resonant beams and collecting the resultant fluorescence.

For continuous imaging we need several hundreds of photons to be scattered over the illumination period. The strategy is simple, illuminate the cloud with a resonant beam, this pumps the atom to the excited state. The atom now decays over a characteristic timescale, the decay partly stimulated by the beam already present as well as spontaneous emission over a characteristic timescale. The emitted photons are detected. The atom is now in the ground state and ready to absorb photons from the beam to be excited and repeat the process again. There is a chance the atom may decay to the ground state that is not addressed by the beam, this is the

dark state. A separate beam to address this state may be used to keep the atom in a cycling transition loop emitting and photons as long as the beams are present. For the imaging beams we can use the MOT beams with the repumper. We may also use a separate imaging beam. We use a 780 nm resonant beam of diameter 1.4 mm, much smaller than the MOT beams. The small beam reduces the background noise. We retroreflect the beam. This allows for longer imaging times and improves the signal by preventing atom losses due to undirectional heating. This is important for imaging the FORT which has a far lower number of atoms. The low signal can only be partially captured by the imaging optics. The emission is isotropic while the imaging lens can only capture a small fraction of the emitted light. There are mirrors and windows and though they are coated to be highly reflecting for the light of the emitted wavelength, we cannot avoid losses, about half the light captured by the lens reaches the camera.

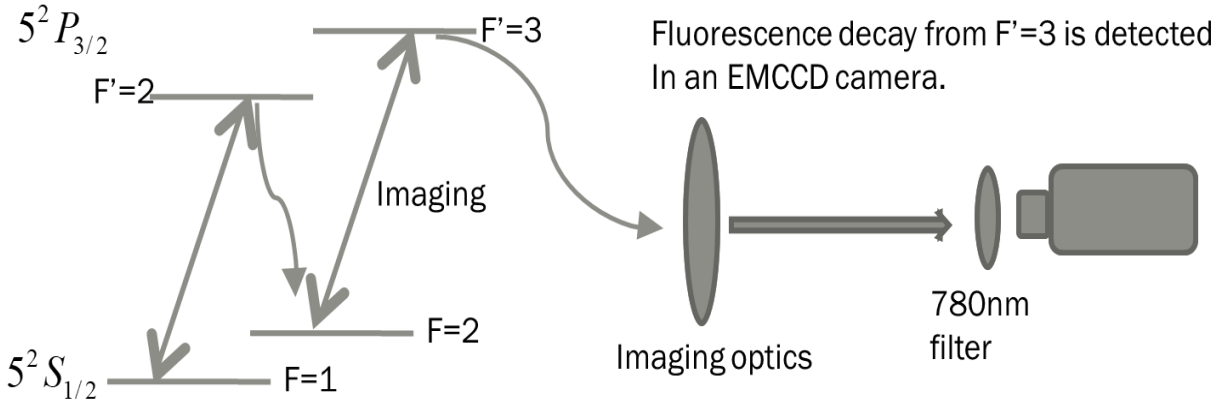

FIGURE 3.6: Imaging setup: Light scattered from the atoms are collected by the imaging optics and focused on the EMCCD camera via a 780 nm filter to block stray background light.

The Electron Multiplying CCD camera (EMCCD) is a highly sensitive camera.

The camera can image low light with a reduced electronic noise achieved by cooling the CCD sensors to $-20 celcius$. The pixels are 8 μm $\times 8 \mu$m. At 780 nm the sensors have a quantum efficiency of 50 percent. This means about two photons incident on a CCD sensor produces, on an average one photoelectron. This photoelectron then undergoes an electron multiplying process. This feature makes the camera very sensitive to low light though the discrete nature of photoelectron counts adds some inherent shot noise. For our experiments we use this camera to measure cloud diameter and make an estimate of the number of atoms in the cloud, to determine the density of the cloud. We can used a time of flight measurement to determine the temperature of the cloud as well. The camera can be triggered by an external trigger making it ideal for timed measurements thought this has some limitations that will be discussed later. For experiments discussed in chapter 4 we could have used the EMCCD setup with high NA optics. The issues with this is discussed in Appendix A

3.5 Modifying MOT to increase optical access

3.5.1 Motives

The size of the MOT chamber restricts optical access significantly. The imaging for experiments that were carried out using an optical dipole trap did not require a large collection angle. However, for single atom imaging we need a large solid angle. For that we need to get as close to the atoms as possible. In order to achieve this larger optical access we modified the MOT.

To this end we remove the MOT beams in the z-direction. The beam from this direction entered through the window that is closest to the atoms. This window is 4 inches in diameter and is $\sim$ 15 cms from the atoms. We obtained a customised

precision aspheric lens from Thorlabs. Aspheric Lens, diameter 100.0 nm, focal length=150.0 mm, AR Coating: $< 0.5\%$ from $650 - 1050$ nm.

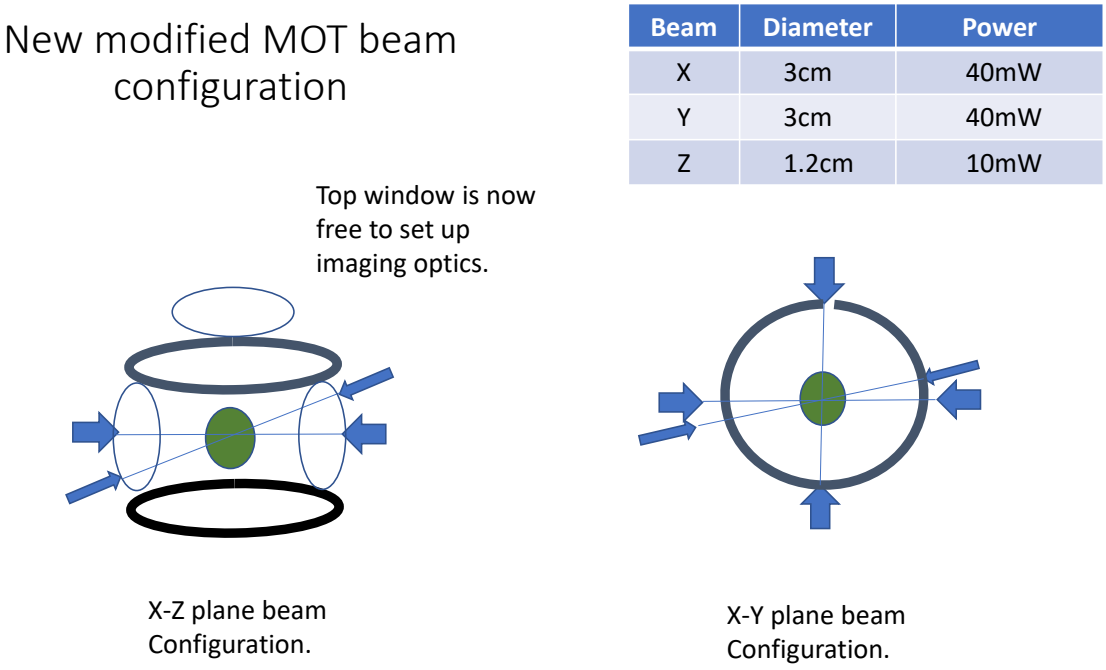

FIGURE 3.7: The new MOT configuration

[1]

We used this lens as the main collection lens. This improves the collection efficiency by a factor of 3, critical for single atom imaging. The Numerical aperture is ~ 0.36 after installing the new lens. The lens is located ~ 17 cms from the location of the MOT atoms, treated as a point source of the signal we intend to capture. From the top lens the collected light is slightly converging (the effective focal length of the lens is 15 cms). The converging light is then incident on an aspheric lens triplet (borrowed from Saffman lab). This shortens the working distance at the expense of losses due to additional optics. The working distance reduces from > 200 cm to ~ 36 cms. The light goes through a trigger operated mechanical shutter (Edmund optics shutter) and is focused on an EMCCD camera via a 10 nm bandpass filter centered at 780 nm. We managed to improve the signal by a factor of 3. This is obviously impacted by the losses from optics and the EMCCD detector quantum efficiency being

50% at 780 nm.The shutter and filter combination seems to reduce background noise significantly. We managed to improve the signal by a factor of 3. At this collection efficiency single atom imaging would need to collect about 300 photons during the imaging and this would produce a signal above the noise level. This would require imaging times of the order of $15 - 20$ ms. The key challenge is to ensure the atom does not escape the trap after several absorption and emission cycles. This requires a tight and deep optical dipole trap.

3.5.2 The new MOT

A schematic of the new MOT is given in the figure below. The beam in the z-direction has been removed. This removes cooling in the z-direction. We replace the vertical z-beam by a smaller beam entering the chamber at an angle of 30^0 with the vertical. This beam is circularly polarized and retro reflected like the X and Y MOT beams.

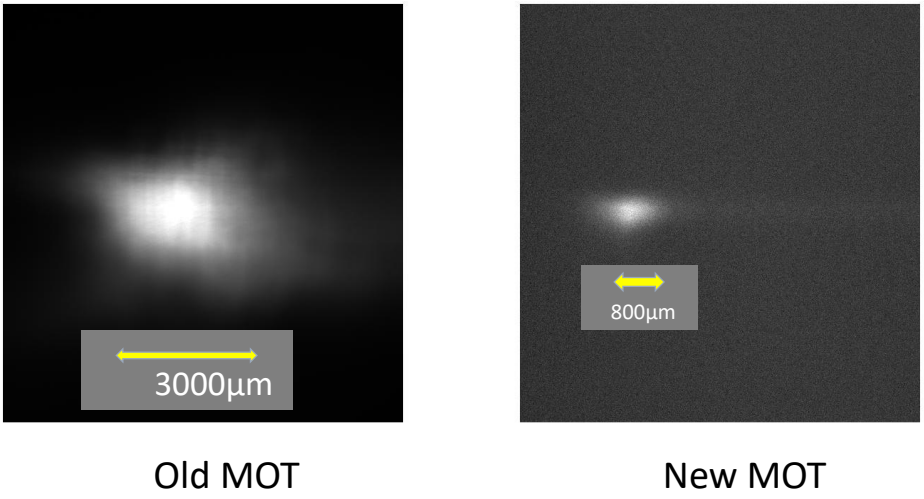

FIGURE 3.8: The new MOT configuration suffers a significant loss in the number of atoms cooled and atomic density

It is a Gaussian with $1/e^2$ diameter of 1.2 cms. Being a smaller beam we need much less power in it. While the X and Y beams have around 50 mW of power in each, the third beam has a power of 3 mW. There were several challenges in getting the new MOT working. The inefficient cooling in the z-direction meant we were getting weaker molasses and the small size of the third beam relative to the other two caused several issues with beam balance. A careful balancing of the beams were carried out to obtain a stable MOT.

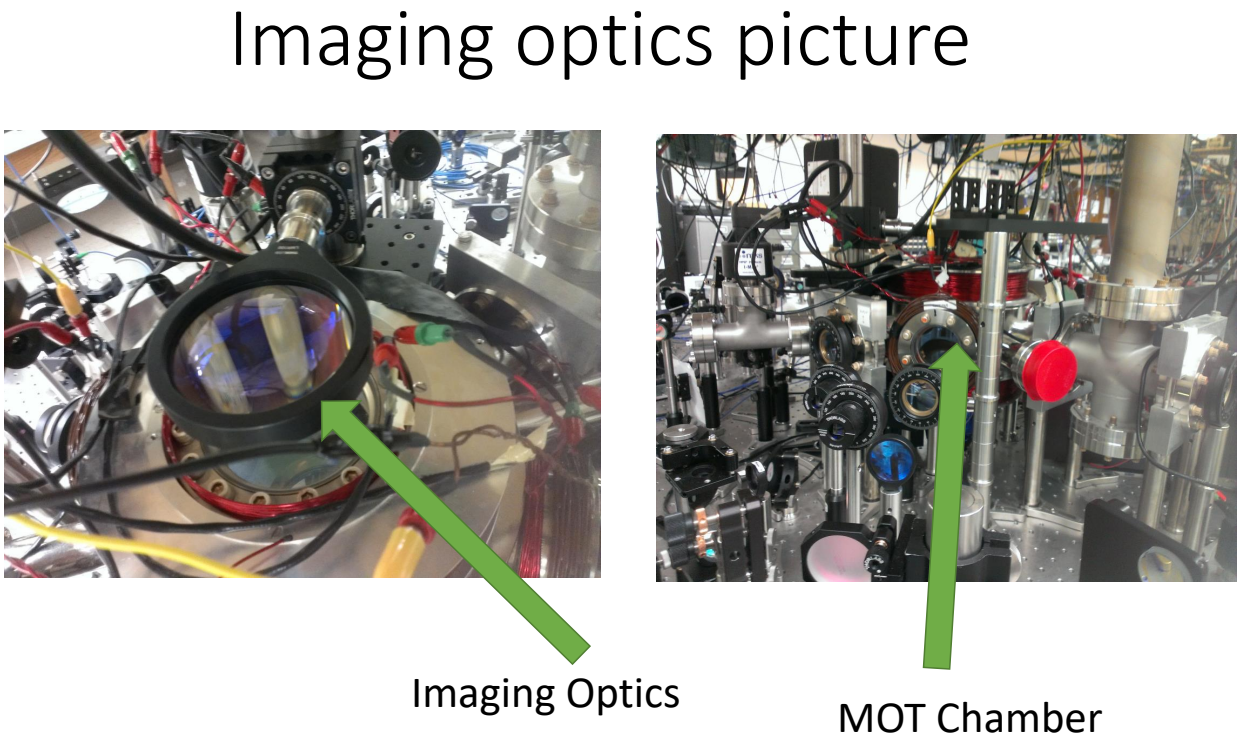

FIGURE 3.9: New Imaging optics can enable imaging weak fluorescence signals

3.5.3 Dipole trap using the new MOT

A functioning dipole trap (FORT) is the first step towards implementing quantum computing projects. The weak MOT made it difficult to obtain a large number of

atoms in the FORT. However, for implementing quantum computing protocols we need one atom, so the weak MOT is not an issue. The problem is the weak FORT laser. The low power in the FORT laser severely limits the imaging time which is a major handicap for single atom imaging where you need the same atom to absorb and emit photons over several cycles to emit enough photons that can be detected by the camera above noise level. The shallow trap means the atoms leave the trap after a few cycles of absorption and emission and a single atom trap cannot be consistently obtained.

We did, however, manage to trap and $\sim$ 300 atoms and imaged the atoms for $\sim 6\mu sec$ Figure 3.10 shows an image of atoms in the dipole trap taken with Andor Axon EMCCD camera. The temperature of atoms in the dipole trap was measure to be around 4 μK.

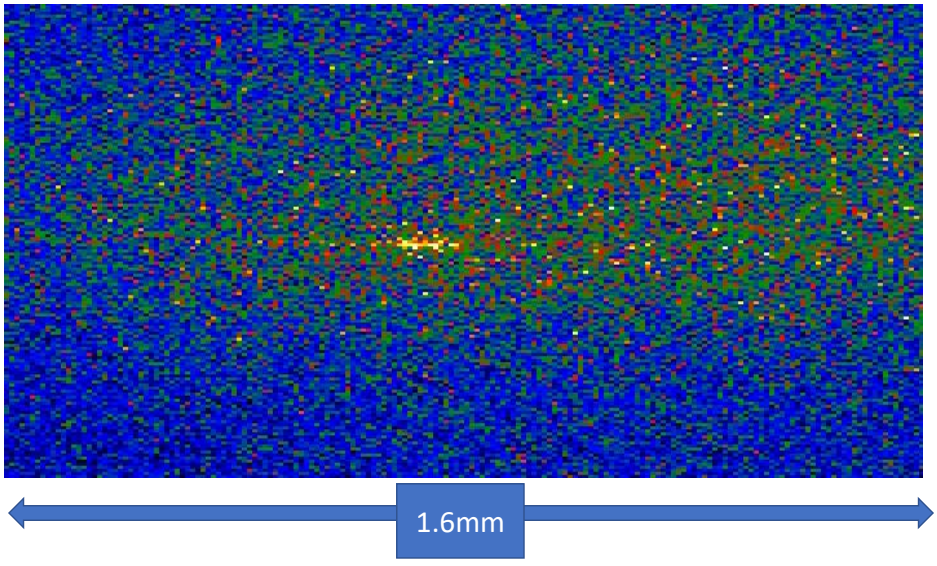

FIGURE 3.10: New Imaging optics can enable imaging weak fluorescence signals

So what can be done to create a single atom trap and image it? The imaging capacity at the moment seems to be good enough for reaching single atom limit. We need deeper traps. To that end we are making progress. The plan is to replace the existing Diode laser/Tapered Amplifier configuration by a Diode Laser/Fiber Amplifer one. The fiber amplifier output, with similar seed powers can reach up to $10W$. The mode is a nice Gaussian mode which leads to efficient first order diffracted beam from the AOM switch. The Gaussian profile also helps in a more efficient coupling to the single mode fiber. We expect to obtain a power of about 2 W in the trapping beam, enough for two or three deep dipole traps or possibly a crossed beam dipole trap.

Imaging can be improved and optimized by having multiple retro-reflecting imaging beam pairs. A 3-D retro-reflecting beam configuration, similar to the MOT can significantly improve imaging timescales.

Chapter 4

Experiments: Collective effects in atomic ensembles

4.1 Collective effects in a dilute sample

We carry out our experiments in the dilute regime where the optical depth of the sample is of the order of ~ 1. To put things in perspective spatially the separation between atoms in the spherical cloud is, on average, approximately 5λ. This is much larger than the Dicke limit in which several atoms are placed within a wavelength It is also much more dilute than recent experiments in the Kaiser group that had atoms separated by λ.

Prior to our experiments, studies of superradiant emission have been carried out in cold atoms in the weak excitation limit [19, 10, 20] as well as in diamond nanocrystals [21] and hybrid solid state devices [22] where it is possible to study the system in the Dicke limit. The work described in [22] beautifully replicates the expected superradiant bursts whose amplitude and escape rates depends on the excitation fraction as predicted by Dicke's model. Subradiance, however is difficult to observe due to reasons mentioned in 2. The cold temperature where atomic motion is very small helps maintain coherence over the time scales concerned. Atoms, on

average moves 1 nm/μs. It is not a perfect but a good start on studying effects in a dilute sample. We expect motion induced dephasing timescales to be longer than the subradiant timescales discussed in the experiments.

The experiments we carry out are fairly simple but there are subtleties we discuss later. We send a pulse of coherent radiation from a laser source through a cloud of atoms. We varied the laser pulse duration with pulses ranging from 20 ns to 200 ns. The pulses were either on resonant of detuned 4Γ, with Γ being the single atom spontaneous decay rate. We tried to make sure we achieve fast extinction of the pulse to ensure we do not have any lingering resonant light scattering photons. The fall time is around 9 ns, which is less than the spontaneous decay time of 27 ns. This is critical for the experiment as the relevant data are photons emitted after pulse extinction. The emitted fluorescence is collected by a set of high numerical aperture optics and coupled to a multi-mode fiber that goes into a photon counting module. The excitation signal, measured by a photodiode and the emitted fluorescence is timed by a fast oscilloscope.

4.2 Experimental schematic

A description of atom cooling and trapping is given in 3. The experiments take place in the atomic ensemble created by the standard methods of Magneto optical trapping and cooling. We have a description of dipole traps as well though experiments carried out in dipole traps were not very successful. A top view of our chamber is shown in Fig. 4.1. We start the experiment by cooling and loading the atoms into a magneto-optical trap (MOT). To construct the ^{87}Rb MOT, we use three counter-propagating beam pairs that are locked to the cycling $F = 2 \rightarrow F' = 3$ transition in the D2 line (transition wavelength of $\lambda_a = 780$ nm), each with a beam power of about 50 mW and a beam size of 2 cm in the X and Y direction. The oblique angled z-beam is

directed into the chamber at an angle. This beam is about 1.2 cm and has an optical power of around 3 mW.

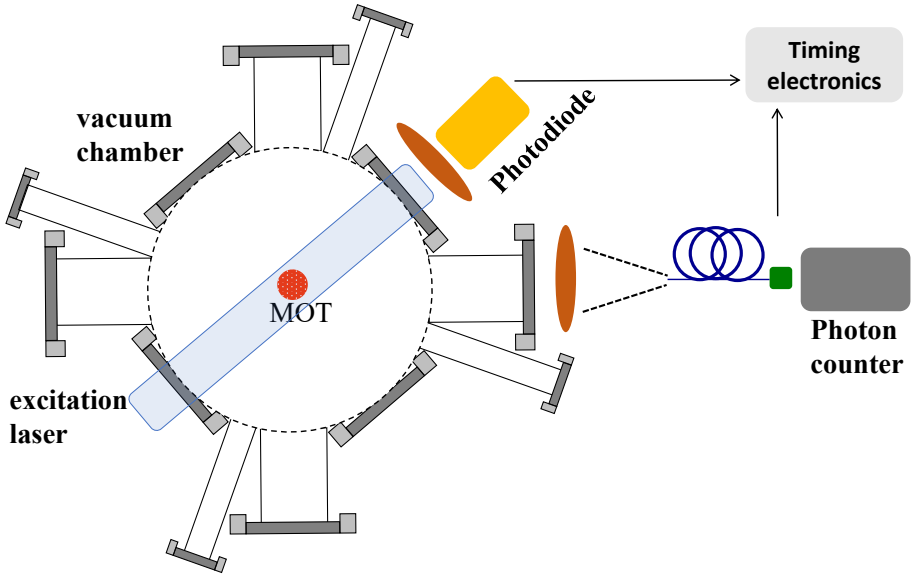

FIGURE 4.1: (Color online) (a) The simplified experimental schematic. The experiment is performed inside a 14-port stainless-steel ultrahigh vacuum chamber. The fluorescence from the cloud is detected using a photon counter.

At the end of the MOT loading cycle, we typically trap $\sim$ 1.3 million atoms, within a radius of R=0.35 mm ($1/e^2$ radius calculated by image of the MOT using an EMCCD camera), giving an on-resonance OD of, OD $= 3N/(k_a R)^2 \sim 1$ ($k_a = 2\pi/\lambda_a$ is the wave number at the transition wavelength). The optical depth gives a measure of the absorption of a weak resonant beam (linear regime) by the cloud. The atomic temperature is about 44 μK which is measured by monitoring the free-expansion of the cloud using an electron-multiplying CCD (EMCCD) camera. During the final 10 ms of the MOT loading cycle, we turn-off the hyperfine repumper beam. As a result, the atoms are optically pumped into the $F = 2$ ground level at the end of the

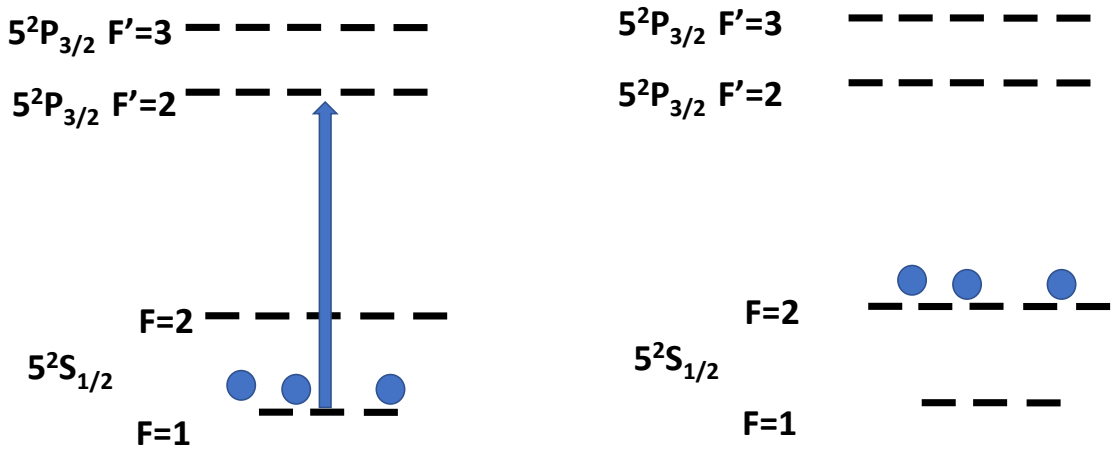

FIGURE 4.2: After the MOT is loaded and with the atoms optically pumped into the $F = 2$ ground level, the atoms are excited into $F' = 3$ level using a short and intense excitation laser. The fluorescence from the cloud is detected using a photon counter.

The relevant energy level diagrams are shown in 4.2 and 4.3. With the atoms optically pumped into the $F = 2$ hyperfine ground level, we turn-off the MOT beams. Then we turn on the excitation pulse. This is a single laser that couples the atoms in the $F = 2$ hyperfine ground level to the $F' = 3$ excited hyperfine level. This laser is the excitation laser. The pulse duration is about 120 ns. With the atoms excited into the $F' = 3$ level, we turn-off the excitation beam. Switching of the excitation beam is achieved using an acousto-optic modulator (AOM). The 90%-10% turn-off time of the excitation laser is 9 ns. This, as mentioned is much smaller than the single atom decay rate. We accomplish such fast switching by careful adjustment of the beam size inside the AOM. The spot size focused in the AOM is about 50 μm. The first order beam from the AOM is coupled into a single mode, polarization maintaining fiber.

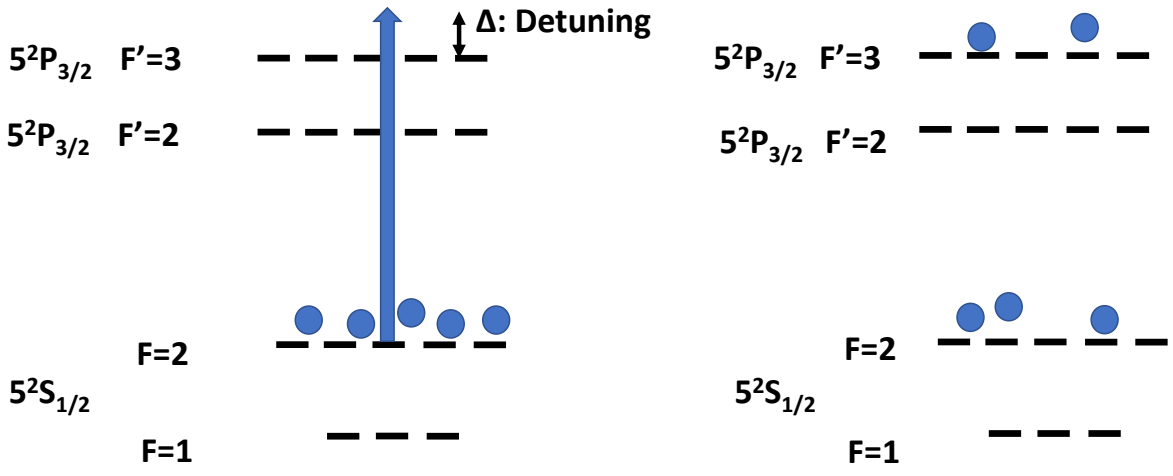

FIGURE 4.3: After the MOT is loaded and with the atoms optically pumped into the $F = 2$ ground level, the atoms are excited into $F' = 3$ level using a short and intense excitation laser.

The output of this fiber is linearly polarized by a beam cube and the direction selected by a waveplate. The beam out of the fiber is a Gaussian beam with $1/e^2$ width out of fiber of around $1mm$. The beam propagates into the chamber, expanding to a diameter of 1.4 mm at the center of the chamber where it hits the MOT. We assume the MOT "encounters" a plane wave Gaussian beam and this approximation is valid, with the MOT being of $1/e^2$ diamater of 35 mm. This is to ensure a proper phase relation between atoms. In principle coherent excitation with well defined phases between atoms can take place for "curved" wave-fronts as well and in futures such studies maybe explored theoretically and experimentally. We however need to make sure the beam size is larger than the atomic cloud to ensure radiation trapping effects are not significant. We record the fluorescence from the atoms using a single-photon counting module (SPCM) and tag the arrival times using a timed measurement in

a high speed oscilloscope. The photons are captured by a focusing lens system, AR coated for 780 nm. The light is focused into a multimode fiber that is coupled to the SPCM. The excitation pulse exits the chamber and is focused on to a high-speed, high bandwidth photodiode. The photodiode signal is also detected in real time using the same oscilloscope. The photon counter has default dark counts even at low signal levels. This is the fundamental noise limit for a photon counting module. We use an iris in front of the fiber coupled to a photon counter, cover the entire imaging system with dark material and work in a dark room to limit stray photons. Our background count is close to the dark count level. There are other subtleties in measurement process involving SPCM discussed in Appendix A (B).

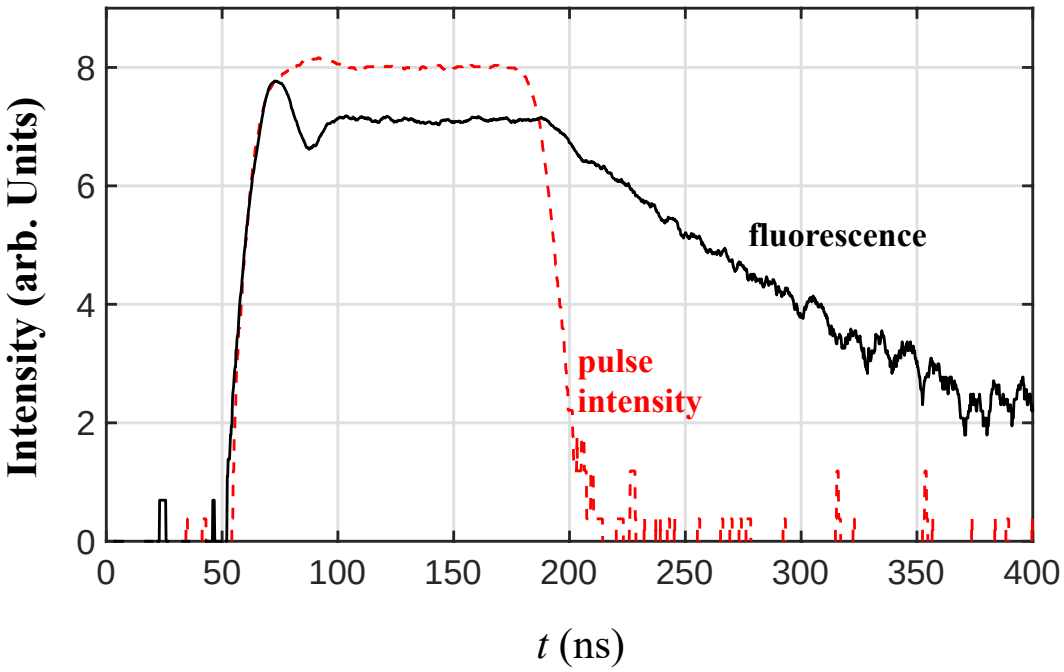

FIGURE 4.4: A sample fluorescence trace (solid black line) overlapped with an excitation pulse intensity trace (dashed red line), both plotted on logarithmic scale. The pulse intensity is measured on a photodiode. The fluorescence trace is the integrated signal from the photon counter.

For each photon detected, the photon-counter produces $\sim$ 10-ns-long electronic TTL pulse, which is then detected by the fast-sampling digital oscilloscope. The

oscilloscope samples at about 1 Gs/sec. To avoid saturation of the photon-counter, we limit the number of detected photons for each experimental cycle to about a few photons per cycle. This is vital as the photon counter has a finite dead time, i.e, a duration for which the counter is inactive. After detecting a photon, the counter goes into an inert mode (inactive or "dead") for about 22-27 ns. During this time any incident photon will not be detected. Thus we will not be able to reproduce an accurate decay curve if we operate in a regime of high photon flux. The strategy, standard in biological imaging and astrophysics, is to reduce the flux to few photons per cycle and carrying out the measurement over several cycles. As a result, the experimental cycle (MOT loading-excitation-fluorescence detection) needs to be repeated many times to obtain a trace with a good signal-to-noise. We typically repeat the experimental cycle $\sim 20,000$ to $60,000$ times to obtain a fluorescence trace. With each experimental cycle lasting for about 1 s, a fluorescence trace takes about 6-20 hours to record in the lab. After every excitation pulse the cloud may be disturbed as we are beyond the weak excitation limit. Therefore we need to reload the cloud for every excitation. Typically we receive, on an average a photon per cycle. To obtain the signal trace we integrate the photon signal on all the counts. We have to ensure that, in the duration of data collection, the lab conditions remain the same. Fluctuations in temperature and humidity cause lasers to drift spectrally causing the lock to drift. We had to discard several hours of data because of this. Also keeping the lasers locked was a challenge. Fortuitiously covering up the lasers using plexiglass helped immensely in stabilizing the lasers and they stayed locked over several days. We kept the MOT gradient coils powered on at all times to prevent hysteresis effects. The field correction shim coils were kept on as well. This ensured the MOT chamber remained magnetized at all times. The experiment can be improved by noise eaters in each beam, with polarization noise being a dominant source of intensity noise. This noise affected coupling to the polarization maintaining single mode fibers used for

all the beams (MOT, repumper, excitation beam). Over several cycles however the fluctuations were minimal, the MOT fairly stable and fluctuations in excitation beam intensity, tracked by the photodiode was about 5% . This was not large enough to effect any of our key results.

Achieving a fast fall time for the AOM excitation beam swith is vital. We use Neos AOM 23210 consisting of a Tellurium Dioxide crystal with a Lithium Niobate transducer. We drive the AOM by a RF signal source at 212 MhZ with the seed beam being one of the ECDLs that go into the MOT beams. The rise/fall time can be calculated by using $t = 1.3d_0/(2V)$ with d_0 being the beam waist/spot size in the crystal and $V = 4260$ m/s, the beam velocity inside the material. We use a Gaussian beam from the output of a single mode fiber and a AR coated lens of short focal length 50 mm to focus the beam to a spot size of around 50 μm. This should, in principle give us a very sharp fall time but we obtain a 90%-10% time of around 9 ns, good enough to analyze superradiant timescales, we obtain superradiant timescales of the order of $15 - 18$ ns. Using the AOM in double passed configuration, in a series of a pair of AOMs or in sequence with a high speed beam block could, in principle, be used to obtain sharper rise and fall times.

A sample fluorescence trace overlapped with an excitation pulse intensity (both on logarithmic scale) is shown in Fig. 4.1(c).

4.3 Experimental data analysis

The short excitation pulse is detected on a fast photodiode after the chamber. The relevant data in our experiment is the signal obtained after turn-off. This $t = 0$ is defined to be the point where the pulse intensity has dropped to less than 10% of its peak intensity. The pulse intensity detected on the photodiode typically becomes indistinguishable from background within a few ns after this point. This is

a consequence of fast switch off that we achieved after careful adjustment of beam size in the AOM. The analysis described is a result of theoredical work presented in work by Deniz and Ben in their paper. The results have been adapted to account for experimental parameters to fit experimental data with a single fitting parameter.

The fluorescence signal recorded using the photon counter is proportional to the optical power emitted from the cloud, and we denote this signal by $P(t)$. Most correlated-decay analysis, including Dicke's original paper, focuses on the total amount of excitation (i.e., the population of the excited level). This is proportional to the total energy stored in the cloud. We denote this quantity by $E(t)$, which is related to the emitted power through the relation $E(t) = E_0 - \int_0^t P(t')dt'$. Here, E_0 is the initial (at $t = 0$) energy stored in the atomic cloud. In the subsequent sections, we will be plotting normalized versions of these quantities, redefined as $P(t) \equiv P(t)/(P(t = 0)$, and $E(t) \equiv E(t)/E(t = 0)$. For independent decay, there is no difference between the time evolution of these two quantities, as they have the identical time dynamics: $E(t) \sim P(t) \sim \exp(-t/\tau_a)$ (τ_a is the lifetime of the excited level $\tau_a = 1/\Gamma_a$).

The photon counter emits a $\sim$ 10-ns-long electronic TTL pulse detected by the oscilloscope that samples at 1 Gs/sec. The scope signal is read by a MATLAB code that reads 2500 data points in the time axis. In the scale that we choose this is about 500 ns at a resolution of 0.2 ns. This is obviously more resolved than the 1 ns sample rate of the scope. We, therefore, bin the data. We first replace each pulse by a single count at a time the pulse has risen 5% of baseline. Then we bin the counts in chunks of 5 data points. This helps with the signal to noise ratio(SNR). Binning too many dats points will help with the SNR but it will affect the accuracy of measured decay rates which we expect to be time-varying. We observe, however, that we can bin 10 data points and still obtain good results. Also, at later times when we have only the slowest modes surviving binning can be very useful as the signal is very weak. A larger binning can be used for signal long after turn-off. We, however, find that a

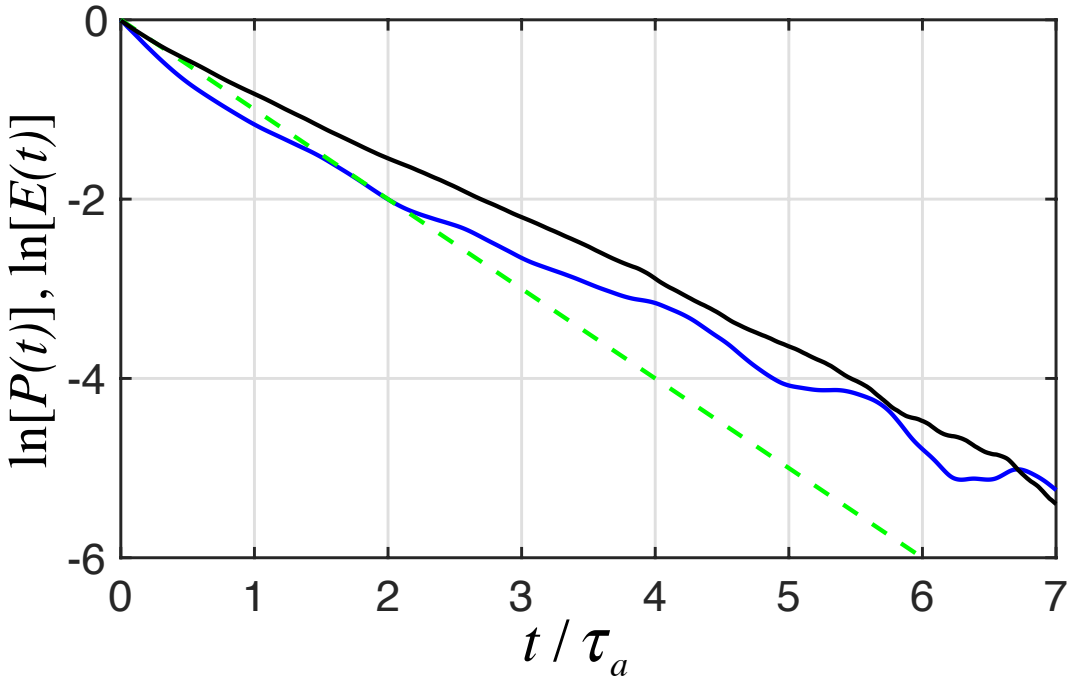

FIGURE 4.5: The observed fluorescence $P(t)$ (solid blue line), and the inferred stored energy in the cloud, $E(t) = E_0 - \int_0^t P(t')dt'$ (solid black line) as a function of time for a sample dataset. Both quantities are appropriately normalized and their natural logarithms are plotted (see text for details). For comparison, the case of independent decay, $\exp(-t/\tau_a)$, is also plotted (dashed green line).

constant bin works fine.

Although the photon counter detects $P(t)$, working with $E(t)$ turns out to be more convenient for most of the data discussed later. This is because $E(t)$ involves integration over the photon counter signal. This has an effect of averaging and thus reduces the noise. An example of this is shown in Fig. 4.5, where we plot the natural logarithm of these quantities as a function of time, $\ln[P(t)]$ (solid blue line) and $\ln[(E(t)]$ (solid black line) for a sample dataset. For comparison, the case of independent decay $\exp(-t/\tau_a)$ is also plotted (dashed green line). The reduced noise in $\ln[(E(t)]$ can be clearly seen in the plots. Furthermore, the two curves do not lie on top of each other, which clearly shows that the decay is not a simple exponential

decay, and cannot be described by a single decay time constant. As we discuss below, consistent with the theoretical model and the numerical results, the variation of the decay time constant during time evolution is better pronounced for $\ln[P(t)]$.

The observed subradiance is quite remarkable considering that there are less than 10^{-4} atoms in a cubic wavelength of volume and the optical depth of the cloud is only of order unity. This, as mentioned is atoms, on average, spaced at 5λ and is by far the most dilute sample for which subradiance has been observed. This is obviously well beyond the Dicke limit. As mentioned before this is significant on a fundamental level as the atoms are, in principle, distinguishable. Collective effects can still persist. This is because, though the atoms are distinguishable, they can still interact with the same vacuum modes causing interference in spontaneously emitted modes. The other critical result is the observed superradiance in a uniformly excited spherical sample. Collective effects and decay rates scale with size and the number of atoms. The results obtained in dilute samples is critical as these effects can give rise to a scale dependent dephasing rate in neutral atom qubit arrays in free space. With increasing scale dephasing can become stronger and possibly impossible to correct by standard error correcting protocols. The size at which this happens is however much larger than present qubit architectures. This is a problem for the future but one of fundamental interest. Another interesting direction, perhaps more optimistic one is the use of weakly coupled subradiant states for quantum information processing and quantum storage while using superradiant states for fast readout.

4.4 Theoretical model and numerical simulations

A detailed analysis is presented in Chapter 5. We discuss, in this section, some concepts directly relevant to the analysis here. Theoretically large sample superradiance and subradiance is known to be quite difficult to analyze in the multiphoton excitation

limit. Beyond the single excitation limit the problem becomes fairly intractible. In the Dicke limit, with all the atoms starting in the excited level, the system can be assumed to remain only in symmetric superpositions. This only leads to superradiant emission since symmetric superpositions are the states where the radiation from the emitters interfere constructively. However, for a large sample there are no obvious symmetries that can be employed and it is not clear how the exponentially large dimension of the Hilbert space can be simplified. Another complication is that for a sample which is spatially large compared to the wavelength, the phase of the emitted radiation varies between different emitters.

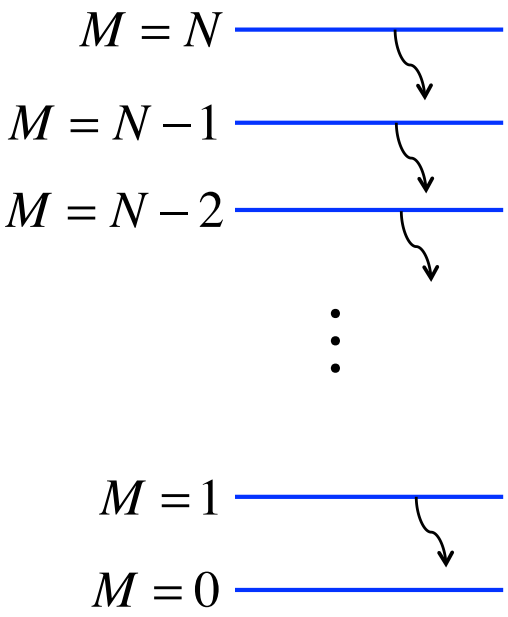

FIGURE 4.6: The excitation decay ladder for the formalism. Each subspace with M atoms excited, decays to a subspace below (i.e., $M-1$ atoms excited).

To model correlated-decay in the large sample and strong excitation regime, we extend the excitation ladder approach as discussed in Ref. [4]. The details of formalism will be presented in Appendix A below, but we summarize the essential ideas here. It is well-known that the excitation ladder approach quantitatively captures many

aspects of Dicke superradiance [4]. The key difficulty is how to extend this model for the large sample regime. For this purpose, we use the recently discovered eigenvalue spectrum of the exchange Hamiltonian, which is the basic physical interaction that causes correlated-decay.

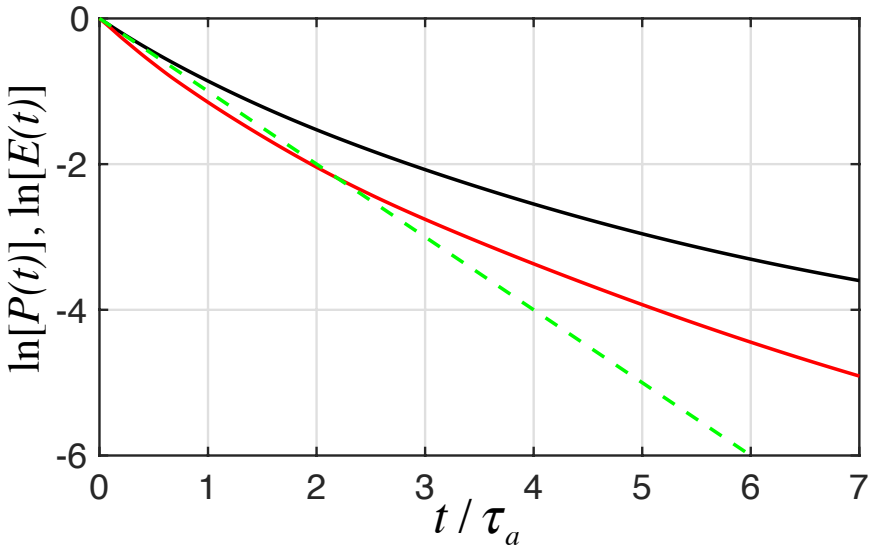

FIGURE 4.7: (Color online) The stored energy $E(t) = \hbar\omega_a \sum_M M\rho_M(t)$ (solid black line) and the radiated power $P(t) = -dE(t)/dt$ (solid red line) for a numerical simulation for the nominal conditions of our experiment: $N = 1.3$ million atoms, excitation fraction of 0.5 and a cloud radius of $R = 0.26$ mm. For comparison, the case of independent decay, $\exp(-t/\tau_a)$, is also plotted (dashed green line).

We consider N atoms uniformly distributed in a spherical cloud with a radius of R. We split the Hilbert space into subspaces that are indexed by $M = 0, 1, ..., N$, which is the number of atoms in the excited state (while the remaining $N - M$ atoms are in the ground state). We denote the probability (i.e., the population) that the system is in M atom excited subspace as $\rho_M(t)$. As shown in Fig. 4.6, each subspace M decays to subspace $M - 1$. At $t = 0$, the system starts in $M = N$ subspace (i.e., at the top of the ladder), and then as time evolves decays down the ladder. We then have a coupled system of $N + 1$ differential equations that describes the evolution of

the system:

$$\frac{d\rho_M}{dt} = -\Gamma_M \rho_M + \Gamma_{M+1}\rho_{M+1} \quad , \tag{4.1}$$

where the quantity Γ_M is the decay rate of subspace M to subspace $M-1$. For independent (i.e., uncorrelated decay), $\Gamma_M = M\Gamma_a$ since the states in subspace M contains M atoms in the excited state and for independent decay the system wavefunction is a product of single-atom wavefunctions. The key idea of our formalism is that we modify this decay rate by the eigenvalue distribution of the exchange Hamiltonian for each subspace. Specifically, we take

$$\Gamma_M = M\Gamma_a + \xi \frac{\sqrt{\pi + 25/12}}{k_a R}\sqrt{N-M}M\tilde{u}\Gamma_a \quad , \tag{4.2}$$

where $\tilde{u}$ is a random variable whose value is uniformly distributed between $[-1, 1]$. We use the dimensionless quantity ξ as a free fitting parameter in the model, which can be viewed as the *shape* factor. This fitting parameter can be thought to account for (i) the deviation of the shape of the cloud from spherical, (ii) the uncertainty in the optical depth and, therefore, the atom number measurement of the cloud, and (iii) the uncertainty in the excitation fraction. As we discuss below, with this fitting parameter, this model successfully produces many aspects of our experimental results. In all the below fits, ξ is of order unity and varies between $0.5 - 2$.

Because the sign of the random variable $\tilde{u}$ can be positive or negative, each rate Γ_M can be faster or slower than the independent decay case. For each simulation, we pick values for Γ_M as given by Eq. (2). Given these values, we then numerically solve $N+1$ coupled differential equations as given by Eq. (1) using fourth order Runge-Kutta method, with the system starting at the top of the ladder: i.e., with the initial condition $\rho_N(t=0) = 1$, and $\rho_M(t=0) = 0$ for all $M \neq N$. For each simulation,

we calculate the total energy stored in the cloud using $E(t) = \hbar\omega_a \sum_M M\rho_M(t)$. The radiated power is calculated using $P(t) = -dE(t)/dt$. To get an accurate description of the dynamics, we repeat the numerical simulation ~ 1000 times, picking different values for Γ_M using Eq. (2). We obtain the final result by averaging over these ~ 1000 simulations.

Figure 4.7 shows numerical results for our nominal experimental conditions: $N =$ 1.3 million atoms, excitation fraction of 0.5 and a cloud radius of $R = 0.26$ mm. Here we plot the stored energy $E(t)$ (solid black) and radiated power $P(t)$ (solid red), both in logarithmic scale, as a function of time. Comparing Fig. 4.7 to the experimental traces of Fig 4.5, the model reasonably captures the overall subradiance, as well as the variation in the decay time scales. However, the model overestimates the variations in the time-scales. One reason for this could be various dephasing mechanisms in the experiment, which is not accounted for in the model.

4.5 Experimental results

We discuss several experiments and present some relevant interesting results in this section. We use data from photon counting module. There were several other results obtained that could not be understood or reproduced for various reasons. These results have been pushed to Appendix A. We discuss results and possible sources of disagreements between experiment and theory wherever applicable.

4.5.1 Excitation fraction scan

We study collective effects beyong the weak excitation regime. Here, the excitation pulse, after extinction leaves the system with multiple excitation. The excitation beam is still in the linear regime, i.e no inversion takes place. Some results at high excitation fraction is discussed in Appendix A. These detasets required a lot of power in the

excitation beam. A separate laser system for the excitation beam was constructed that unfortunately performed poorly and the results were not replicated. In [10], subradiance was studied in the weak excitation regime where the single-atom excited subspace is a good approximation to the full dynamics. In this regime, the observed subradiant time-scales are independent of the intensity of the excitation laser. In this section, we discuss that in the regime of multiphoton excitation in the sample, this is no longer the case and we observe that the decay rates depend on the excitation fraction. Figure 4.8 shows ln[$(E(t)$] for high excitation fraction of 0.3 (solid black curve) and 0.08 (blue curve). The amount of observed subradiance is significantly reduced as the excitation fraction is reduced.

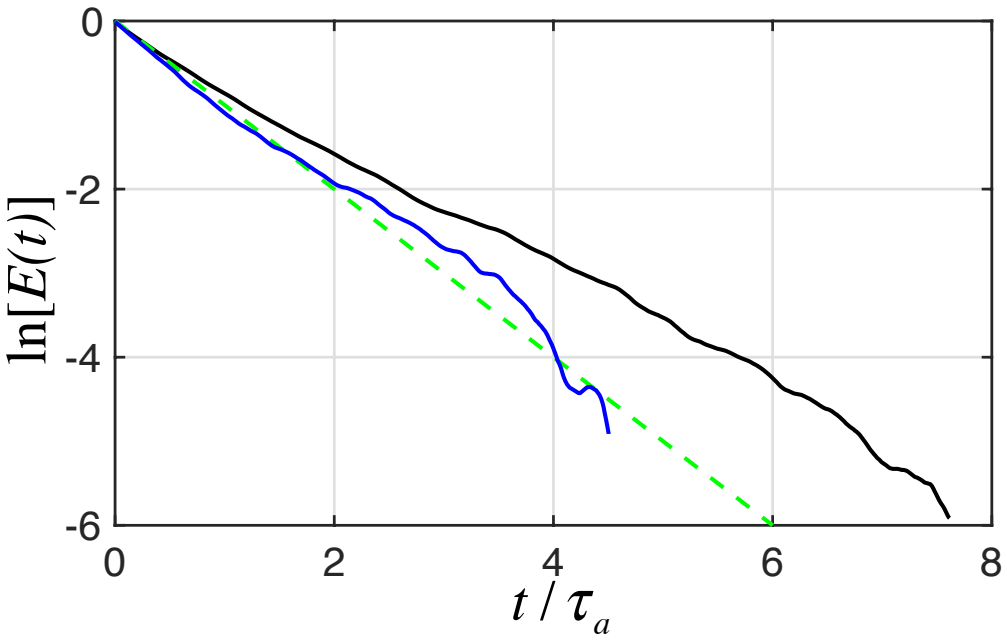

FIGURE 4.8: ln[$(E(t)$] for high excitation fraction of 0.3 (solid black curve) and 0.08 (blue curve). For comparison, the case of independent decay, $\exp(-t/\tau_a)$, is also plotted (dashed green line). The amount of observed subradiance is significantly reduced as the excitation fraction is reduced.

Figure 4.9 shows the mean decay time during $0 < t <$60 ns for 12 experimental curves similar to the ones shown in Fig. 4.8. The curves are chosen from multiple

experiments that are carried out in similar lab conditions. While there is large spread in the data, there is a clear trend that as the excitation fraction is increased, the decay time scales increase (i.e., the system becomes more subradiant). The black curve is the result of analytical result where again the free parameter is adjusted to get a good agreement for the high excitation fraction of 0.3. Again with this single fitting parameter, there is good agreement between the model and the experimental results.

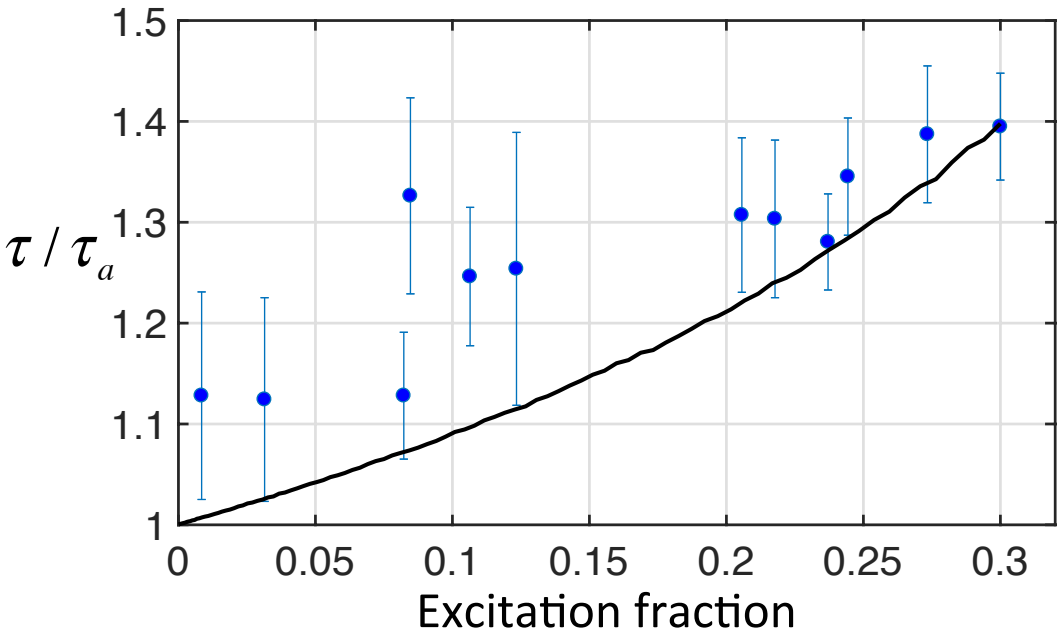

FIGURE 4.9: The mean decay time during $0 < t <$60 ns. The error bar in each data point is the standard variation of the decay time, and is therefore a measure of how much the decay time changes during the same time window.

4.5.2 Optical depth scan

We study collective effects in a very dilute sample. The on resonance OD is given by OD $= 3N/(k_a R)^2$. Thus we can control the OD by parameters N and R. The cloud radius is easy to control. We use the uniform free expansion of the cold atomic

cloud for this. This keeps N, the number of atoms approximately constant. After the CMOT stage we vary the time between excitation pulses to allow free expansion. The largest cloud that we study is still smaller than the excitation beam thereby ensuring plane wave excitation. Figure 6 shows $\ln[(E(t)]$ for cloud optical depth of OD= $1, 0.83, .68, 0.52$, and 0.35. In each plot, the dashed red line is the result of the theoretical model with the free parameter adjusted to be $\xi = .77$. This parameter is adjusted once to get a good overall fit for $0 < t < 9\tau_a$ for the top plot (i.e. for OD=1). There is no further adjustment for the consequent plots. With this single fitting parameter, there is good agreement with the experimental data and the numerical results. For comparison, the case of independent decay, $\exp(-t/\tau_a)$, is also plotted in dashed green line. The result clearly shows that as the optical depth is reduced, the observed subradiance is reduced and the decay approaches to independent (i.e., uncorrelated) decay. This is expected. Collective effects become weaker as average spacing between atoms is increased. Further discussion on this effect can be found in Chapter 4 (5).

Figure 4.11 shows the mean decay time for each experimental curve shown in Fig. 4.10 during $0 < t <$60 ns. The black curve is the result of analytical result where again the free parameter is adjusted to get a good agreement for OD=1.

4.5.3 Signatures of superradiance-to-subradiance transition

A beautiful illustration of collective effects in atomic ensembles is the coexistence of superradiant and subradiant effects. After the fast decay of superradiant states we have a slow subradiant decay. Theoretically, in the Dicke problem this is expected. Dicke superradiance is caused by symmetric states strongly coupled to vacuum modes while vanishing decay is caused by antisymmetric coupling (weaker coupling). We do not, of course, operate in the Dicke limit. However, our theoretical model does predict

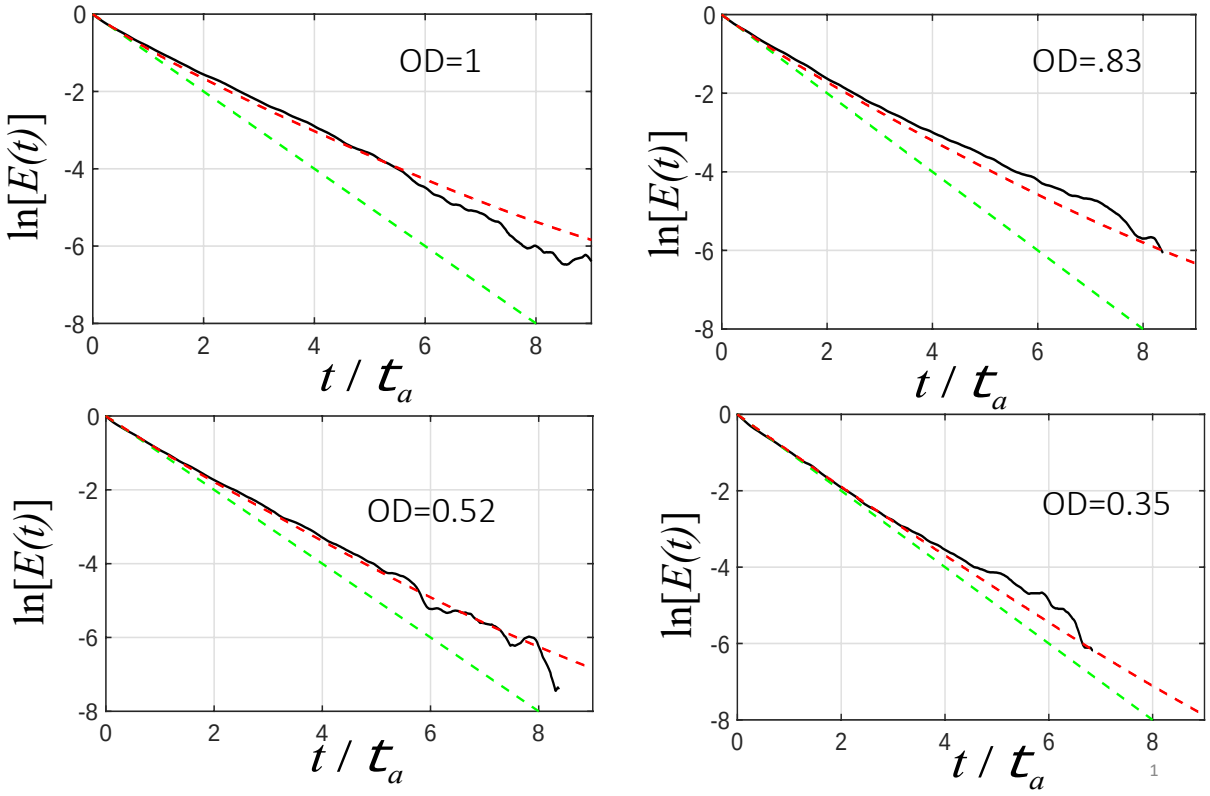

FIGURE 4.10: $\ln[(E(t)]$ as the optical depth is varied from OD=1 (top left) to OD=0.35 (bottom right). In each plot, the dashed red line is the result of the theoretical model discussed in the text. For comparison, the case of independent decay, $\exp(-t/\tau_a)$, is also plotted (dashed green line). As expected, as the optical depth is reduced, the observed subradiance is reduced and the decay approaches to independent (i.e., uncorrelated) decay.

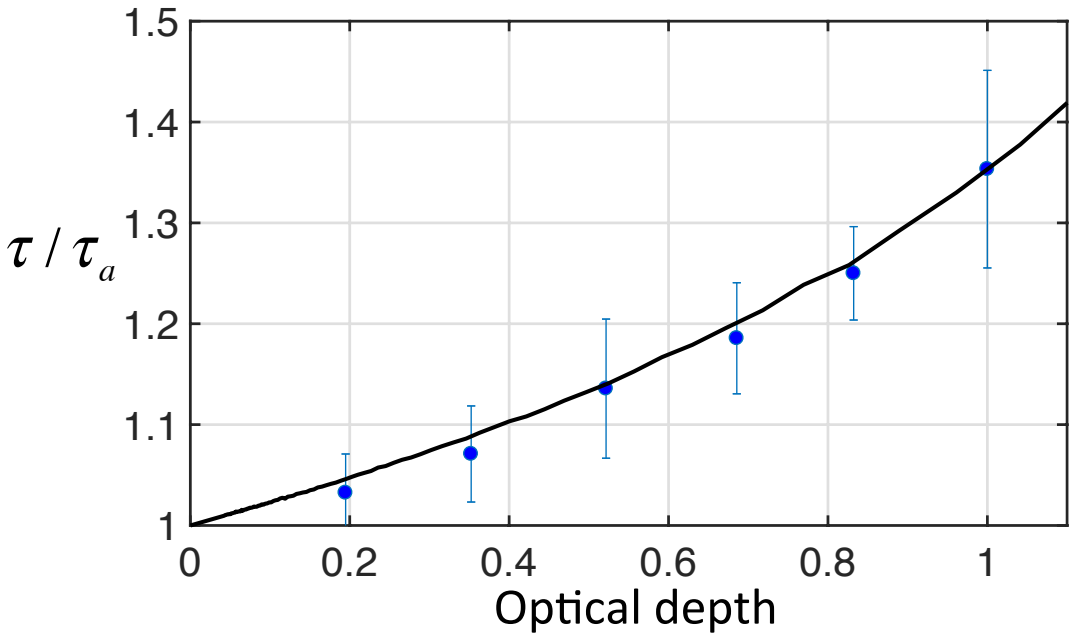

FIGURE 4.11: The mean decay time for each experimental curve shown in Fig. 4.10 during $0 < t <$60 ns. The error bar in each data point is the standard variation of the decay time, and is therefore a measure of how much the decay time changes during the same time window.

faster and slower than independent decay channels and we expect to capture both superradiant and subradiant photons as the system decays down the excitation ladder. To observe the effect in experimental data, we focus on the variation of the decay time as the system evolves and look for signatures of superradiant-to-subradiant transition. In Figure 4.12 we see a decay curve for $0 < t < 7\tau_a$ at high excitation fraction and OD=1. Faster than independent decay (superradiant) dynamics is evident for $t < \tau_a$.At longer time scales the system evolves to a slower subradiant decay.

We look at the system dynamics at early times, $0 < t < 3\tau_a$. It is critical to note at this stage that in order to observe faster than independent decay we need extinction faster than decay rate to ensure that there are no unwanted excitations during the decay and that the decay is not "stimulated" by resonant radiation. Having a fast switch off helps in this regard. With a 9 ns switch off we have extinction faster than most superradiant modes. On top of that, assuming a collection of two level atoms,

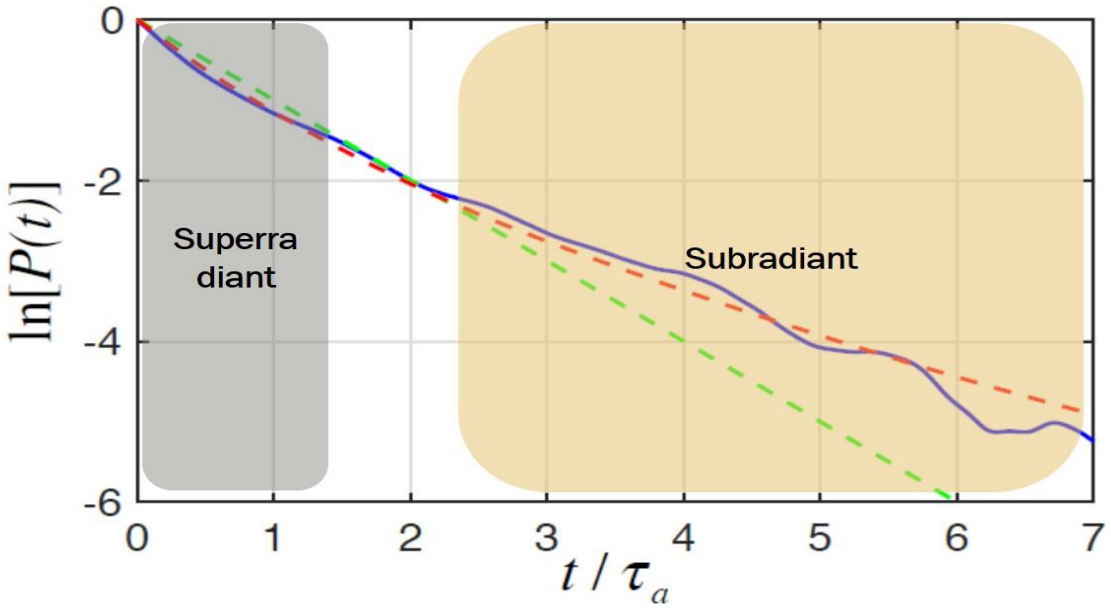

FIGURE 4.12: The system starts off decaying at a rate faster than independent decay rate (superradiant) and then evolves to a subradiant decay. The zones are demarcated by different shades of colour.

it can be shown that a faster than independent decay cannot be stimulated by a resonant beam. Therefore, faster than independent decay is a signature of collective effects. Figure 4.13 shows the observed fluorescence in logarithmic scale, $\ln[P(t)]$, for a cloud optical depth of OD= 1 (solid black), 0.83 (solid red), 0.68 (solid blue), and 0.52 (solid green). For comparison, the case of independent decay, $\exp(-t/\tau_a)$, is also plotted (dashed green line). For all the sets, faster than independent decay (superradiant) dynamics is evident for $t < \tau_a$. As the system evolves, this superradiant decay either evolves to subradiance (high optical depth (mainly for high OD black and red curves), or to independent decay (low optical depth: blue and green curves). For all the sets, faster than independent decay (superradiant) dynamics is evident for $t < \tau_a$. For each set, the $\pm\sigma$ statistical error bars on the data points are also plotted (dotted blue lines) to demonstrate that the observed superradiance is well-beyond the error-bars of the data. The error bars increase as the system evolves due

to the reduced number of detected photons at later times of the decay. As the system evolves, superradiance either evolves to subradiance [high optical depth; (a) and (b)], or approaches to independent decay [low optical depth: (c) and (d)].

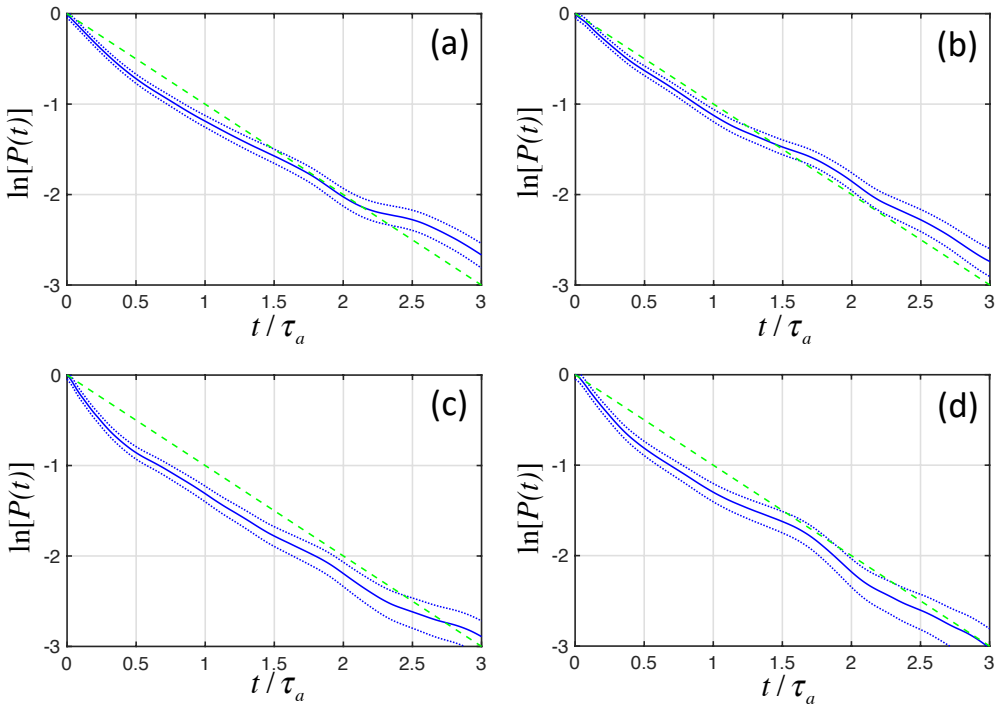

FIGURE 4.13: The observed fluorescence (solid blue lines) in logarithmic scale for a cloud optical depth of (a) OD= 1, (b) 0.83, (c) 0.68, and (d) 0.52. For comparison, the case of independent decay, $\exp(-t/\tau_a)$, is also plotted (dashed green line). For each set, the $\pm\sigma$ statistical error bars on the data points are also plotted (dotted blue lines) to demonstrate that the observed superradiance is well-beyond the error-bars of the data. The error bars increase as the system evolves due to the reduced number of detected photons at later times of the decay.

As the system evolves, this superradiance either evolves to subradiance (high optical depth; black and red curves), or to independent decay (low optical depth: blue and green curves). This may be because dephasing is more prominent at low ODs.

Figure 4.14 shows the observed fluorescence for two optical depths OD= 1 (high) and OD= 0.52 (low) over a longer time window $0 < t < 7\tau_a$, and also overlapped with the numerical results (dashed red curves). Here, the free parameter is adjusted only once to be $\zeta = 0.9$, in order to get good agreement with the experimental results for the high optical depth (left plot). For this case, the numerical results capture the variation of the decay time constant during time evolution, as well as superradiance-to-subradiance transition very well. For the lower optical depth (right plot), the agreement between the experimental data and the numerical results is worse. Specifically, the experimental curve continues to show signatures of superradiance at early times, while the numerical results do not. The reason for this discrepancy is currently an open question. We speculate that one reason for the discrepancy could be the assumption of a uniform cloud in the numerical simulations. In the experiment, the density of the MOT is unlikely to be uniform, due to the complicated three dimensional interference pattern produced by the six MOT laser beams. Because of this interference, there are likely localized regions with a higher density, which may be responsible for the persistent superradiant feature at early times, even at low optical depths

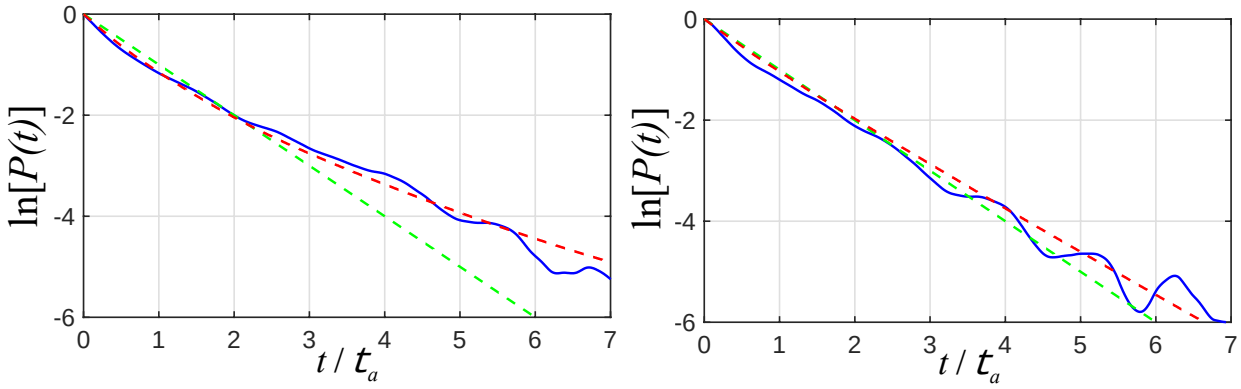

FIGURE 4.14: The observed fluorescence in logarithmic scale for a cloud optical depth of OD= 1 (left) and 0.52 (right). For comparison, the numerical results are also plotted (dashed red curves).

For the lower optical depth (right plot), the agreement between the experimental data and the numerical results is worse. Specifically, the experimental curve continues to show signatures of superradiance at early times, while the numerical results do not. The reason for this discrepancy is currently an open question. We speculate that one reason for the discrepancy could be the assumption of a uniform cloud in the numerical simulations. In the experiment, the density of the MOT is unlikely to be uniform, due to the complicated three dimensional interference pattern produced by the six MOT laser beams.

4.6 Radiation trapping vs subradiance

Multiple scattering of radiation in matter is known as radiation trapping. A schematic picture is shown in the figure. A simple interpretation is a photon knocked around like a billiard ball undergoing multiple collisions with atoms. Of course this interpretation is naive and too simplistic. Scattering takes place at all frequencies but is prominent near resonance. On resonant scattering can have elastic or inelastic components. The photon can be scattered coherently in which case the scattered radiation maintain coherence. It may also undergo multiple instances of absorption and emission making the process highly incoherent. Going into the details is not in the scope of the thesis. Interested readers may refer to an excellent article by Lagendijk and van Tiggelen [56]. However it is important to discuss multiple resonant scattering, coherent or otherwise in the context of subradiant emission.

4.6.1 On-resonance versus detuned excitation

The model we use for our analysis assumes a certain number of excitations in the cloud. If the saturation intensity of the exciting beam is kept constant, the detuning of the beam, whether it is on resonant or detuned may seem to be irrelevant. However,

at resonance multiple resonant scattering, both elastic and inelastic is enhanced. This may "trap" photons in the cloud. The trapping becomes strong at resonance. Thus a photon may remain trapped in the cloud for a while and released at a longer timescale. This may look like subradiance. Because of the low OD of our ultracold cloud, we do not expect incoherent photon absorption followed by reemission (i.e., radiation trapping) to play a role in our experiment. We devote a section at the end of the chapter to a discussion of radiation trapping as it may cause some controversy in the interpretation of our results especially in the subradiant regime. To experimentally confirm that radiation trapping is not prominent, we compare fluorescence when the excitation laser is on-resonant versus off-resonant. Figure 4.15 shows the enerly in the cloud $\ln[(E(t)]$ as a function of time for two different optical depths, OD=1 (black line) and OD=0.35 (blue line), contrasting on-resonance ($\Delta = 0$) and detuned ($\Delta = 4.2\Gamma_a$) excitation laser. For both cases, the results are qualitatively similar with a stronger overall subradiance for OD=1 . The variation of subradiance with optical depths is discussed in a later sub-section. If radiation trapping was responsible for the observed slower decay rate, there would be a large difference between on-resonance versus off-resonance excitation. This is because, for a detuning of $\Delta = 4.2\Gamma_a$, the photon absorption probability (i.e., off-resonant optical depth) is expected to decrease by a factor of $(2\Delta/\Gamma_a)^2 \approx 70$ compared to its on-resonant value. The data shown in the rest of the paper is taken at this detuning of $\Delta = 4.2\Gamma_a$.

This is because, this has an effect of "trapping" photons in the cloud, thereby mimicking subradiance. So how do we know the slow emission we observe at later time scales is due to collective effects, i.e subradiance and not multiple scattering as in radiation trapping. The effects are subtle and the slowing of emission is not very large, we see an increase of a factor of 1.4, which is not very large. A lot of However, we can make a case for subradiance.

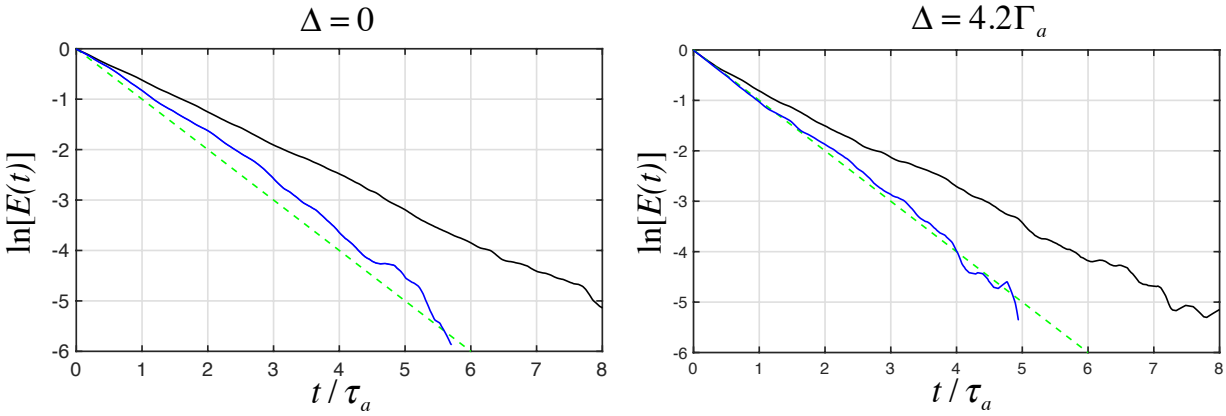

FIGURE 4.15: Stored energy in the cloud (i.e., excited state population), $\ln[(E(t)]$ for two different optical depths, OD=1 (black line) and OD=0.35 (blue line). The left-plot is obtained for an excitation laser which is on-resonant, while the right plot is for a detuning of $\Delta = 4.2\Gamma_a$. For comparison, the case of independent decay, $\exp(-t/\tau_a)$, is also plotted (dashed green line). Because the results are qualitatively similar, this shows that radiation trapping does not play a significant role.

4.6.2 On resonance Optical Depth

It is well-known that on-resonant radiation trapping, which is critically important for atomic clouds with a large optical depth, can mimic subradiance. The strongest case we can make in favour of subradiance is that the on-resonant OD of the atomic cloud in our experiments is of order unity. We measure the optical depth using two different methods. In the first one, we measure the absorption of a very weak resonant beam through the cloud. In the second approach, we monitor continuous fluorescence of the MOT atoms with the EMCCD under full saturation. Using the detected photon counts at the EMCCD and known solid angle of the collection optics, optical losses, and quantum efficiency of detection, we can then infer the number of atoms in the MOT. Together with the measurement of the size of the MOT cloud, this then allows us to infer the optical depth. We have found these two different measurements of the OD to be reasonably consistent, agree to within a factor of 2. In above we report the OD measurements using the absorption of a weak resonant beam, since we believe

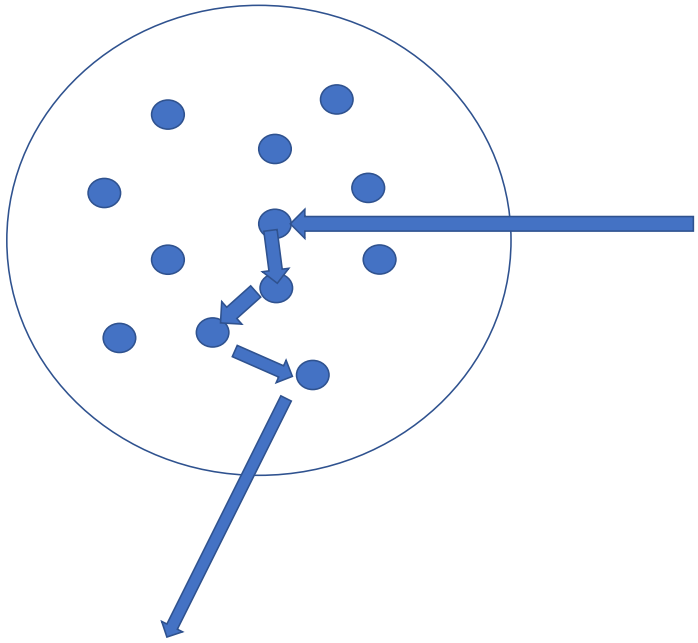

FIGURE 4.16: Incoming photon gets "bounced around" before escaping mimicking the effect of subradiance.

this approach to be more reliable.

For atomic clouds with near-uniform illumination (i.e. the size of the beam larger than the size of the cloud, which is the case in our experiment), radiation trapping is predicted to be negligible at such low optical depths. For example, as discussed in Ref. [11], exact Monte-Carlo simulations suggest that optical depths far larger than unity is needed for multiple scattering events (which result in radiation trapping) to become appreciable.

4.6.3 Variation of subradiant time-scales with Optical Depth

Our experimental data of Fig. 4.9 rules out radiation trapping being a dominant factor role. In this plot, we show that the subradiant time scales increase as the excitation fraction of the cloud (i.e., the initial number of atoms in the excited state) increases.

If radiation trapping was a dominant factor, we would expect exactly the opposite behavior: i.e., the subradiant time scales should have decreased as the excitation fraction is increased. For larger excitation we have a larger fraction of atoms in the excited state making it less likely for a photon to be reabsorbed by the cloud.

For larger excitation fractions, there are fewer atoms in the cloud initially in the ground state, and the probability of a photon being absorbed by the cloud decreases (i.e., the "effective" optical depth of the cloud is reduced as the excitation fraction is increased).

4.6.4 Presence of superradiance

Collective effects manifest itself in superradiant and subradiant decay rates. The presence of superradiance with rates fitting well with subradiant scales according to a theoretical model discussed later is a strong evidence for subradiance.

The Dicke model predicts superradiance and subradiance as well. So the presence of superradiance explains collective effects in the cloud.

Chapter 5

Theory

5.1 Coupled Dipole model

The Coupled Dipole model has been the standard tool for analyzing collective effects in the weak excitation limit. As mentioned before we can study these effects beyond the Dicke limit but with a single photon in the cloud. In this simplified situation we show the problem to be equivalent to the emission of a collection of phased dipoles. Several other effects like directional emission can also be analyzed using the model. An understanding of the coupled dipole model can be a good headway to the much more complicated problem of multiphoton excitation, so it is worth discussing.

The derivation of the exchange interaction Hamiltonian is given in detail in the paper Ref. [12] and in [10].

5.1.1 A. Hamiltonian

Consider N two-level atoms, each with levels $|0\rangle$ and $|1\rangle$, in a three-dimensional geometry. We denote each individual atom with the index j and consider a continuum of electromagnetic modes with annihilation and creation operators $\hat{a}_{\kappa\epsilon}$ and $\hat{a}^{\dagger}_{\kappa\epsilon}$ respectively. These operators act on the mode of the field with wave-vector κ and polarization ϵ. The total Hamiltonian for the system when only the energy conserving terms are

retained (under the rotating wave approximation) is [12]:

$$\begin{aligned}\hat{H}_{total} &= \sum_j \frac{1}{2}\hbar\omega_a\hat{\sigma}_z^j + \sum_{\kappa\epsilon}\hbar\nu_{\kappa\epsilon}\left(\hat{a}_{\kappa\epsilon}^\dagger\hat{a}_{\kappa\epsilon} + \frac{1}{2}\right) \\ &- \sum_j\sum_{\kappa\epsilon}\hbar g_{\kappa\epsilon}\left[\hat{a}_{k\epsilon}\exp\left(i\vec{\kappa}\cdot\vec{r}_j\right)\hat{\sigma}_+^j + \hat{a}_{\kappa\epsilon}^\dagger\exp\left(-i\vec{\kappa}\cdot\vec{r}_j\right)\hat{\sigma}_-^j\right] \quad , \end{aligned} \tag{5.1}$$

where

$$\begin{aligned}\hat{\sigma}_z^j &= |1\rangle^{j\ j}\langle 1| - |0\rangle^{j\ j}\langle 0| \quad , \\ \hat{\sigma}_+^j &= |1\rangle^{j\ j}\langle 0| \quad , \\ \hat{\sigma}_-^j &= |0\rangle^{j\ j}\langle 1| \quad . \end{aligned} \tag{5.2}$$

In Eq. (5.1), the first two terms describe the atoms and the electromagnetic modes in the absence of any interaction whereas the third term describes the coupling between the two systems. $\vec{r}_j$ is the position of the j'th atom and the energies of the atom states $|0\rangle$ and $|1\rangle$ are taken to be $-\frac{1}{2}\hbar\omega_a$ and $\frac{1}{2}\hbar\omega_a$, respectively. The Dicke limit of the above equations is obtained when the total size of the sample is assumed to be small compared to the κ-vector of the relevant modes, i.e., $\vec{\kappa}\cdot\vec{r}_j \to 0$.

5.1.2 Timed Dicke state

We choose an eigenstate describing the single excitation in the cloud.

$$|\psi\rangle_{TD} = \sum_j \frac{1}{\sqrt{N}}[\exp\left(-i\vec{\kappa}\cdot\vec{r}_j\right)|000...1_j...0\rangle] \tag{5.3}$$

Here the atomic state $|\psi\rangle_{TD}$ is the phased state with a single excitation in the cloud. This can be contrasted with the symmetric Dicke state

$$|\psi\rangle_{Dicke} = \sum_j \frac{1}{\sqrt{N}}[|000...1_j...0\rangle] \tag{5.4}$$

where the term $\exp(-i\vec{\kappa}\cdot\vec{r}_j) = 1$ in the Dicke limit. Here $|000...1_j...0\rangle$ is the N-atom state with atom j is in the excited state with all the other atoms in the ground state.

The field state is chosen to be the vacuum state $|\psi_{field}\rangle = |0\rangle$

The combined atomic ensemble and field initial state is assumed to be in a separable product state to begin with

$$|\psi(t=0)\rangle = |\psi\rangle_{TD} \otimes |\psi_{field}\rangle \tag{5.5}$$

We let the system evolve under the Hamiltonian Eq. (5.1). The atomic state can be coupled to the ground state by the third term in the Hamiltonian in Eq. (5.1). At any time t the state of the atom field system can be written as

$$|\psi(t)\rangle = \sum_j \alpha_j(t)(|000...1_j...00\rangle \otimes |0\rangle) + \beta(t)(\sum_{\kappa\epsilon} |000...\rangle \otimes |1_{\kappa\epsilon}\rangle) \tag{5.6}$$

Here $|1_{\kappa\epsilon}\rangle$ is the singly occupied photon mode occupying the state with wave vector κ with polarization state ϵ.

We can interpret $|\dot{\beta(t)}|^2$ as the rate at which the ground state is populated, which, because of the ansatz eigenstate we have chosen, can be interpreted as the rate of photon emission from the cloud. For an understanding of the collective effects we can look at the rates of fluctuations of excited state populations. It can be shown after

some straightforward calculation that

$$\frac{d}{dt}\alpha_i(t) \sim -\frac{\Gamma}{2}\alpha_i(t) + i\frac{\Gamma}{2}\sum_j V_{ij}\alpha_j(t) \tag{5.7}$$

The first term is just the rate of independent decay while the second term captures the collective effects. The term $V_{ij} \sim \frac{\exp(i\kappa|r_i - r_j|)}{\kappa|r_i - r_j|}$. This captures an effective dipole-dipole interaction between atoms giving rise to collective effects. If we want to find the rate of photon emission $\frac{d}{dt}\sum_i |\alpha_i^2|$ we can see that it is equivalent to computing the far field intensity of a collection of N oscillating dipoles with a phase proportional to $\exp(i\kappa|r_i - r_j|)$. This is called the coupled dipole model. Intuitively, any phased sum of fields can give rise to "constructive" or "destructive" interference terms. The constructive interference terms lead to a faster than single atom decay, i.e superradiance, where as the destructive interference terms give rise to subradiance. The coupled dipole model works very well in the weak excitation limit as demonstrated by several experiments. It gives us an intuition as to how photon emission rates can give us information about collective effects in an ensemble. We can also get an idea of how we expect these rates to scale with cloud size, atom separation, optical depths etc. The dependence of collective effects on the coupling term V_{ij} which becomes weaker as the cloud becomes more dilute shows why collective effects become weaker as the optical depth decreases. The coupled dipole model, however, has several limitations and it cannot be applied to our system effectively, the obvious factor being the assumption of a single excitation in the cloud. Multiphoton excitation needs to be taken into account when we are dealing with the kind of experiments we are trying in our lab. The variation of decay rates with excitation fraction cannot be captured by the model. The problem becomes analytically intractable for higher excitation fraction and hence we need a different approach, discussed in the subsequent sections.

5.2 Beyond the coupled dipole model

5.2.1 The effective Hamiltonian: multiphoton excitation

In the previous section we observed the effect of coupling term V_{ij}. The key physical effect that describes many different aspects of collective decay, including superradiance and subradiance is the exchange interaction. Starting with the Hamiltonian of Eq. (5.1), this interaction has been derived using a variety of approaches by a number of authors [60, 61, 7, 62]. The derivation uses assumptions that are similar to the traditional Wigner-Weisskopf theory of spontaneous decay [63]. As an ansatz, we take the initial atomic system to be an arbitrary superposition (in general entangled state) and assume that the field is in a zero excitation in each electromagnetic mode $\kappa\epsilon$. We then study the problem in the interaction picture and integrate out the probability amplitudes of the continuum states using the usual Born-Markov approximation. The initial state of the combined atom-field system can be written as

$$|\psi(t=0)\rangle = \sum_{q}^{2^N-1} c_{q,0}|q\rangle \otimes |0\rangle. \tag{5.8}$$

Here, the index q runs through all possible 2^N combinations for the qubits and $c_{q,0}$ are the expansion coefficients. For each $|q\rangle$ we define $2M_q = \#atomsinstate|1\rangle - \#atomsinstate|0\rangle$

Thus the total energy of atomic state $|q\rangle$ is $M_q\hbar\omega_a$. The general state at any time t can be written as

$$|\psi(t)\rangle = \sum_{q=0}^{2^N-1} c_{q,0}(t)\exp(-iM_q\omega_a t)|q\rangle \otimes |0\rangle \quad + \quad \sum_{\kappa\epsilon}\sum_{q'=0}^{2^N-1} c_{q',0}(t)\exp(-i(M_{q'}\omega_a + \nu_{\kappa\epsilon})t)|q'\rangle \otimes |1_{\kappa\epsilon}\rangle. \tag{5.9}$$

Here $|1_{\kappa\epsilon}\rangle$ is the state of the radiation field in which the field mode $\kappa\epsilon$ has one photon and all other modes are in the vacuum state.

The Schroedinger equation

$$i\hbar\frac{d}{dt}|\psi(t)\rangle = \hat{H}_{total}|\psi(t)\rangle \tag{5.10}$$

Using the wave function ansatz from eq. (5.9) and plugging it in eq. (5.10), we can arrive at the following effective interaction Hamiltonian:

$$\hat{H}_{eff} = \sum_j \sum_k \hat{H}^{jk} \quad . \tag{5.11}$$

Here, the sum is over all pairs of qubits and operators $\hat{H}^{jk}$ act nontrivially only on the qubits with indices j and k

$$\hat{H}^{jk} = F_{jk}\hat{\sigma}_+^j\hat{\sigma}_-^k + F_{kj}\hat{\sigma}_-^i\hat{\sigma}_+^j \quad , \tag{5.12}$$

with coupling constants of F_{jk}:

$$F_{kj} = -(i\frac{\Gamma_a}{2} + \delta\omega_a)(\frac{3}{8\pi})\left[(1-\cos^2\theta_{jk})\frac{\sin\kappa_a r_{jk}}{\kappa_a r_{jk}} + (1-3\cos^2\theta_{jk})(\frac{\cos\kappa_a r_{jk}}{(\kappa_a r_{jk})^2} - \frac{\sin\kappa_a r_{jk}}{(\kappa_a r_{jk})^3})\right] \tag{5.13}$$

Note that in the above equation we have $F_{jk} = F_{jk}$. This is analogous to a"spin" exchange interaction, with the interaction mediated by photons.

Here, Γ_a is the single-atom decay rate and $\delta\omega_a$ is the single-atom Lamb shift of the qubit transition. r_{jk} is the distance between the two atoms, and θ_{jk} is the angle between the atomic dipole moment vector and the separation vector $\vec{r}_{jk}$. The quantity

κ_a is the wave vector for the electromagnetic modes energy-resonant with the qubit transition: $\kappa_a = \omega_a/c$.

The exchange term F_{jk} is going to take over from the term V_{ij} introduced earlier in the analysis of the problem by the coupled dipole method.

5.2.2 The width of the eigenvalue distribution for M-subspace

In this section, we discuss the width of the eigenvalue spectrum of the exchange Hamiltonian $\hat{H}_{eff} = \sum_{jk} \hat{H}^{jk} = \sum_k F_{jk}\hat{\sigma}_+^j\hat{\sigma}_-^k + F_{kj}\hat{\sigma}_-^j\hat{\sigma}_+^k$ in the $N \to \infty$ limit, for the M-atom excited subspace. Details of the derivation is given in [12]. In this limit, the eigenvalues λ of $\hat{H}_{eff}$ can be viewed as having a continuous distribution with probability density function $f_\Lambda(\lambda) \equiv P\{\Lambda = \lambda\}$. The width of the probability density function can be evaluated by explicitly calculating the second-moment (variance) of the distribution $\sigma^{(2)} \equiv E[\Lambda^2] = \int f_\Lambda(\lambda)\lambda^2 d\lambda$, where $E[...]$ stands for the expected value. By definition, this second moment is:

$$\begin{aligned}
\sigma^{(2)} &= E[\Lambda^2] = \begin{pmatrix} N \\ M \end{pmatrix}^{-1} \mathrm{Trace}\left[(\hat{H}_{eff})^2\right] \quad , \\
&= \begin{pmatrix} N \\ M \end{pmatrix}^{-1} \sum_q \langle q| \left(\sum_{jk} F_{jk}\hat{\sigma}_+^j\hat{\sigma}_-^k + F_{kj}\hat{\sigma}_-^j\hat{\sigma}_+^k \right)^2 |q\rangle \quad . \qquad (5.14)
\end{aligned}$$

Here, the summation q is over all the states in the M atom excited subspace. By inspection, each term $\langle q| \left(\sum_{jk} F_{jk}\hat{\sigma}_+^j\hat{\sigma}_-^k + F_{kj}\hat{\sigma}_-^j\hat{\sigma}_+^k\right)^2 |q\rangle$ produces $(N-M)M$ contributions, each appropppriately scaled with the the square of the relevant coupling constant, F_{jk}^2. In the $N \to \infty$ limit, the result is therefore:

$$\begin{aligned}
\sigma^{(2)} &= (N-M)ME[F_{jk}^2] \quad , \\
&= \frac{\pi + 29/12}{k_a^2 R^2}(N-M)M\Gamma_a^2 \quad . \qquad (5.15)
\end{aligned}$$

Here, in the last step, we have used the expected value of the squares of the coupling constants in a three-dimensional geometry, $E[F_{jk}^2]$, as discussed in Ref. [12]. The standard deviation (width) of the distribution is the square-root of the variance given in Eq. (5.15):

$$\sigma = \sqrt{\sigma^{(2)}} = \frac{\sqrt{\pi + 29/12}}{k_a R}\sqrt{N-M}\sqrt{M}\Gamma_a \quad . \tag{5.16}$$

The distribution is symmetric around $\lambda = 0$, which means that there are an equal number of superradiant and subradiant states. Numerical analysis in [12] has shown that the results are insensitive to the precise shape of the distribution; rather, the width of the distribution is critical. We can therefore work with a simple uniform distribution centered around $\lambda = 0$, with a width given by Eq. (5.16).

5.2.3 Heuristic incorporation of stimulated emission

The formalism described above assumes each photon mode to be unoccupied initially, and as a result, it does not incorporate stimulated emission in the decay process. In the small sample regime, an M-atom subspace has "M" photons stored, and the spontaneous rates would at most be enhanced by "M", as the system decays through the ladder. This is because, the stimulated emission rate for an M-photon state is a factor of M larger than the spontaneous rate [63]. For a large sample, all emitted photons would not interfere constructively, but instead interfere with random phases. As a result, we hypothesize that one would expect $\sqrt{M}$ enhancement compared to the spontaneous rate for the large sample. We, therefore, multiply the width given by Eq. (5.16) by a factor of $\sqrt{M}$ to heuristically incorporate for stimulated emission.

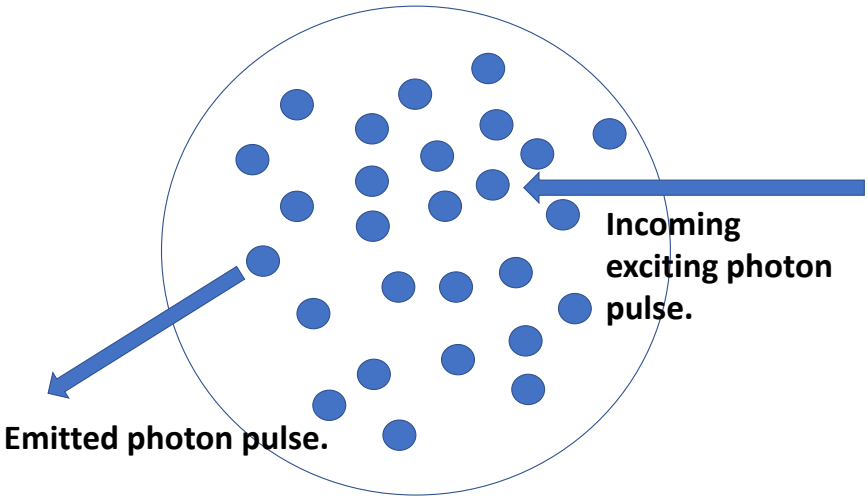

FIGURE 5.1: The direction of emitted photon is correlated with the direction of exciting photon pulse.

5.2.4 Directional emission

This section is not relevant in the context of the experiments we are trying to do. However it is a good addition to the chapter as it presents a beautiful aspect of collective effects in the photon emission characteristics. We go back to the Timed Dicke state.

$$|\psi\rangle_{TD} = \sum_j \frac{1}{\sqrt{N}} [\exp(-i\vec{\kappa}\cdot\vec{r}_j)|000...1_j...0\rangle] \tag{5.17}$$

Instead of looking at the effective coupling Hamiltonian we can look at the emitted photon modes. The Timed Dicke state has a photon symmetrically distributed in the cloud. The expectation value of the collective dipole moment operator in the cloud is zero, i.e there is no "direction" associated with the collective atom photon state of the cloud and field. The cloud is now allowed to evolve under the Hamiltonian with a treatment similar to calculation of spontaneous emission modes. After a time $t \to \infty$,

is large compared to atomic evolution time-scales we find, after some straightforward calculations.

$$|\psi_{field}\rangle \sim \delta(\vec{k} - \vec{k}_0)|1\rangle \tag{5.18}$$

The emitted photon is strongly correlated to the direction of the incoming photon [24]. The directional emission is characteristic of collective effects in a sample in weak excitation but is different from the "superradiant burst" in the Dicke limit [4].

In the single photon limit we expect to find some directional nature to the superradiant photons. The direction of the emitted photons are correlated with the direction if exciting photon. This correlation is lost in case of multiple excitations with the system cascading down the excitation ladder (Fig. 4.6). We do not analyze directional dependence in our experiments, though this is an interesting avenue for exploration in future.

Chapter 6

Part II: Coherent quantum control using dark states

In this section of the thesis we study quantum control using dark state in an atomic ensemble under conditions of EIT (Electromagnetically induced transparency). Quantum computing using dark states can provide several advantages primarily due to the "darkness" of the system. The term originates from the fact that under conditions of EIT, the system is decoupled from the excited state and we see no fluorescence driven by spontaneous emission. This is achieved by choosing a Λ system in the atom (3 energy levels, two metastable ground states and one excited state). We couple the two ground states using two separate excitation beams with the excited state. The dark state is formed by destructive interference of the two paths to the excited state which results in an eigenstate with no component in the excited state. The relative amplitudes in the two ground states depends on the relative strengths of the coupling to the excited states, which in turn depends on the Rabi frequencies of the two addressing beams (i.e the beam intensities). Thus the relative populations of the two ground states can be coherently controlled by adjusting the beam intensities. This is a feature we exploit for coherent quantum state manipulation. Another feature is that the dependence of state transfer on beam intensities are non linear. For our

experiments we use the cold atom setup described in chapter 3. Experiments described here have been carried out in our lab from 2011-2017 and several grad students were involved. Previously EIT experiments were carried out in hot atomic vapours as well.

Chapter 7

Quantum computing and coherent control using EIT

7.1 Introduction

The goal of this current project is to implement a C-Phase quantum gate with subwavelength resolution using spatial properties of dark state under conditions of Electromagnetically induced transparency (EIT). This is an extension our work on subwavelength localization of atomic excitation described in [68] and [70]. For single atom trapping and imaging we have implemented a non-conventional MOT to clear an access window that was previously used for a MOT beam pair in our MOT chamber. This window has a larger diameter and is also closer to the atoms, it could be used to collect a large fluorescence fraction. We have set up large N.A collection optics for single atom imaging (in-fact as large as possible for the set-up we had, N. A$\sim$ .3). Recently we have acquired a fiber amplifier that will allow us to implement deep optical dipole traps for single atom trapping and imaging. With improved imaging capacity and a strong robust optical dipole trap we hope to implement single atom quantum gate and quantum state readout and in future two qubit gates. The long-term goal is to extend the scheme to an atomic array of qubits for a scalable neutral

atom quantum computer.

My first project after joining our lab was to build on a project that experimentally demonstrated subwavelength localization of atomic excitation by using Electromagnetically induced transparency in Rubidium atoms in a dipole trap (Phys. Rev. X 3, 031014 (2013)). The team was led by my supervisor Deniz and my senior Jared Miles. Over the next couple of years, we improved the system to demonstrate stronger and improved localization (Physical Review A92, 033838 (2015)).

In this section of the thesis we discuss progress towards implementing EIT/dark state based qubit addressing, gate implementation and localized readout scheme. Experimental results and strategies are discussed. Simulations and theoretical schemes are analyzed.

7.2 Electromagnetically induced transparency

7.2.1 Derivation of the EIT Hamiltonian

In this section we discuss the theory of EIT. We start with a generic 3-level system, two metastable ground states $|1\rangle$ and $|2\rangle$ and one excited state $|e\rangle$. We have a pair of plane polarized beams. We will discuss subtleties arising due to multilevel structure of ^{87}Rb.

Consider a 3-level system shown in the figure below. For the lambda scheme we work in, EIT can occur if each of the lower two levels are coupled to the excited by separate laser beams. The figure shows the energy diagram and laser used for the lambda EIT configuration. The “probe” beam is a laser that couples the lowest state $|1\rangle$ to the state $|e\rangle$. is and has frequency ω_p. The "coupling" laser beam couples $|2\rangle$ to the state $|e\rangle$ is and has frequency ω_c. We assume that the dipole matrix element

for levels $|1\rangle$ and $|2\rangle$ is zero, the transition is dipole forbidden, that between $|e\rangle$ and $|1\rangle$ is given by μ_{1e} and $|e\rangle$ and that between $|e\rangle$ and $|2\rangle$ is μ_{2e}.

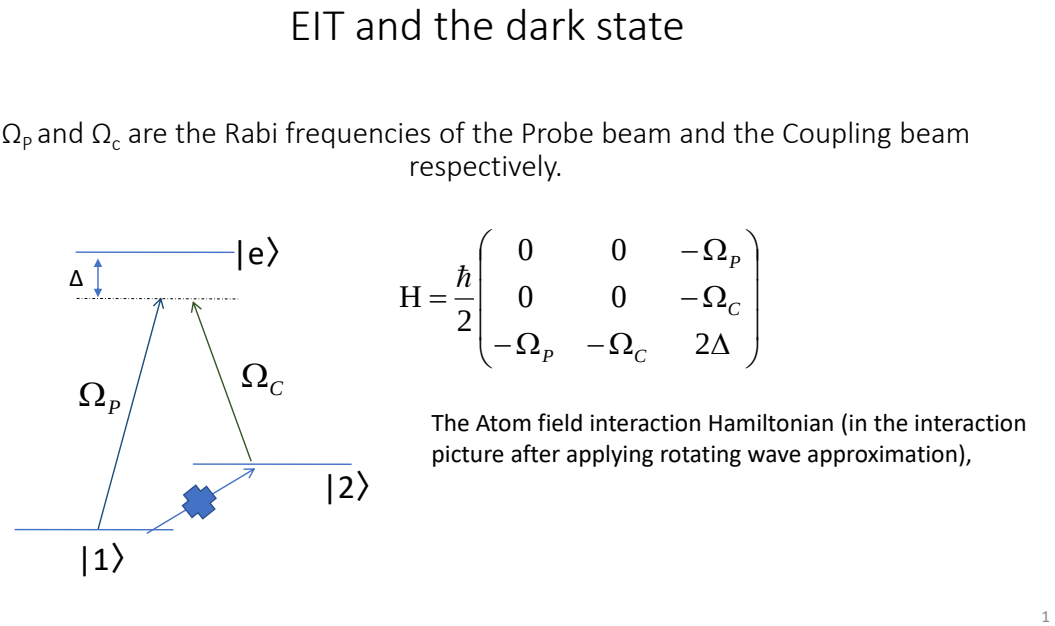

FIGURE 7.1: The Λ schematic and effective Hamiltonian. Transition between $|1\rangle$ and $|2\rangle$ is dipole forbidden.

Incident radiation fields can be described classically as oscillating electric fields with slowly varying amplitudes

Coupling beam

$$E_c(r,t) = \frac{E_c(r,t)}{2}[\exp(i(\omega_c t)) + \exp(-i(\omega_c t))] \tag{7.1}$$

Probe beam

$$E_p(r,t) = \frac{E_p(r,t)}{2}[\exp(i(\omega_p t)) + \exp(-i(\omega_p t))] \tag{7.2}$$

We assume a fixed atomic position and set $r = 0$. The total Hamiltonian describing the system can be written as a sum of atomic Hamiltonian, H_{atom} and the Hamiltonian describing atom and field coupling, H_{int}.

$H_{int} = \mu_{1e}.E_p(r,t)(|e\rangle\langle 1| + |1\rangle\langle e|) + \mu_{2e}.E_c(r,t)(|e\rangle\langle 2| + |2\rangle\langle e|)$

$H_{atom} = \hbar\omega_1|1\rangle\langle 1| + \hbar\omega_2|1\rangle\langle 2| + \hbar\omega_e|e\rangle\langle e|$

$$H_{total} = H_{atom} + H_{int} \tag{7.3}$$

We denote the interaction Hamiltonian in terms of Rabi frequencies defined by

$\Omega_p = \mu_{1e}E_p/\hbar$

$\Omega_c = \mu_{2e}E_c/\hbar.$

We use a unitary matrix to transform the original Hamiltonian in to one with no time dependent terms. We describe the procedure here.

$$\mathrm{H}_{total} = \begin{bmatrix} \hbar\omega_1 & 0 & \frac{1}{2}\Omega_p(e^{i\omega_p t} + e^{-i\omega_p t}) \\ 0 & \hbar\omega_2 & \frac{1}{2}\Omega_c(e^{i\omega_c t} + e^{-i\omega_c t}) \\ \frac{1}{2}\Omega_p(e^{i\omega_c t} + e^{-i\omega_c t}) & \frac{1}{2}\Omega_c(e^{i\omega_c t} + e^{-i\omega_c t}) & \hbar\omega_e \end{bmatrix}$$

Next we apply a time dependent unitary transformation, $U(t)$, to the Hamiltonian. The transformation gives

$$H_{tr} = U(t)HU(t)^{\dagger} + i\hbar U(t)\dot{U}(t) \tag{7.4}$$

We choose $U(t)$ to be a matrix of the form

$$\mathrm{H}_{total} = \begin{bmatrix} \hbar\omega_x & 0 & 0 \\ 0 & \hbar\omega_y & 0 \\ 0 & 0 & \hbar\omega_z \end{bmatrix}$$

This gives

$$\mathrm{H}_{tr} = \begin{bmatrix} \hbar(\omega_1 - \omega_x) & 0 & \frac{1}{2}\Omega_p(e^{i\omega_p t} + e^{-i\omega_p t})e^{i(\omega_z - \omega_x)t} \\ 0 & \hbar(\omega_2 - \omega_y) & \frac{1}{2}\Omega_c(e^{i\omega_c t} + e^{-i\omega_c t})e^{i(\omega_z - \omega_y)t} \\ \frac{1}{2}\Omega_p(e^{i\omega_p t} + e^{-i\omega_p t})e^{i(\omega_z - \omega_x)t} & \frac{1}{2}\Omega_c(e^{i\omega_c t} + e^{-i\omega_c t})e^{i(\omega_z - \omega_y)t} & \hbar(\omega_e - \omega_z) \end{bmatrix}$$

We can simplify the Hamiltonian by choosing

$\omega_x = \omega_1$

$\omega_y = \omega_2 - \delta\omega$

$\omega_z = \omega_2 - \Delta$

where $\delta\omega = (\omega_2 - \omega_1) - (\omega_p - \omega_c)$ and $\Delta\omega = (\omega_3 - \omega_1) - \omega_p$

This simplifies the Hamiltonian to

$$\mathrm{H}_{tr} = \hbar \begin{bmatrix} 0 & 0 & \frac{1}{2}\Omega_p(e^{i\omega_p t} + e^{-i\omega_p t})e^{i\omega_p t} \\ 0 & \delta\omega & \frac{1}{2}\Omega_c(e^{i\omega_c t} + e^{-i\omega_c t})e^{i\omega_c t} \\ \frac{1}{2}\Omega_p(e^{i\omega_p t} + e^{-i\omega_p t})e^{i\omega_p t} & \frac{1}{2}\Omega_c(e^{i\omega_c t} + e^{-i\omega_c t})e^{i\omega_c t} & \Delta \end{bmatrix}$$

$$= \hbar \begin{bmatrix} 0 & 0 & \frac{1}{2}\Omega_p(1 + e^{-i2\omega_p t}) \\ 0 & \delta\omega & \frac{1}{2}\Omega_c(1 + e^{-2i\omega_c t}) \\ \frac{1}{2}\Omega_p(1 + e^{-i2\omega_p t}) & \frac{1}{2}\Omega_c(1 + e^{-i2\omega_c t}) & \Delta \end{bmatrix} \tag{7.5}$$

Finally we neglect the terms $e^{-i2\omega_p t}$ and $e^{-i2\omega_c t}$. These fast oscillating terms are expected to average to zero in the timescales over which the dynamics of the system is studied. This is known as the rotating wave approximation (RWA). Applying this simplifies the Hamiltonian to the final form we call H_{EIT}.

$$\mathrm{H}_{EIT} = \hbar \begin{bmatrix} 0 & 0 & \frac{1}{2}\Omega_p \\ 0 & \delta\omega & \frac{1}{2}\Omega_c \\ \frac{1}{2}\Omega_p & \frac{1}{2}\Omega_c & \Delta \end{bmatrix}$$

The Hamiltonian in its final form does not have any time dependent terms and is considerably simpler to work with than the full time dependent Hamiltonian.

For observing EIT we need the term $\delta\omega = 0$. This is when the frequency difference of the probe and coupling laser is equal to the separation of the two levels $|1\rangle$ and $|2\rangle$. This gives us

$$\mathrm{H}_{EIT} = \hbar \begin{bmatrix} 0 & 0 & \frac{1}{2}\Omega_p \\ 0 & 0 & \frac{1}{2}\Omega_c \\ \frac{1}{2}\Omega_p & \frac{1}{2}\Omega_c & \Delta \end{bmatrix}$$

Diagonalizing the Hamiltonian is straightforward. One of the eigenstates is known as the "dark state" as it has an eigenvalue of zero.

$|D\rangle = \frac{1}{\tilde{\Omega}}[\Omega_c|1\rangle - \Omega_p|2\rangle]$

with $\tilde{\Omega} = \sqrt{\Omega_p^2 + \Omega_c^2}$ The dark state $|D\rangle$ has no component in the excited state and the "darkness" of arises from the fact that it is decoupled from both the probe and coupling beams. The term was coined because no fluorescence is observed when the

system is in this state. It is straightforward to see that $H_{EIT}|D\rangle = 0$, i.e. the state does not evolve with time. The other two eigenstates are the bright states $|B_+\rangle$ and $|B_-\rangle$

$$|B_+\rangle = N[\Omega_p|1\rangle + \Omega_c|2\rangle + \alpha|e\rangle]$$

and

$$|B_-\rangle = N[\Omega_p|1\rangle + \Omega_c|2\rangle - \alpha|e\rangle]$$

where α and N are the excited state amplitude and eigenstate normalization respectively. For $\Delta >> \Omega_p$ we have

$|B_+\rangle = \frac{1}{\tilde{\Omega}}[\Omega_p|1\rangle + \Omega_c|2\rangle] + \frac{\Delta\tilde{\Omega}}{\tilde{\Omega}^2+\Delta^2}|e\rangle]$

and

$|B_-\rangle = \frac{1}{\tilde{\Omega}}[\Omega_p|1\rangle + \Omega_c|2\rangle] - \frac{\Delta\tilde{\Omega}}{\tilde{\Omega}^2+\Delta^2}|e\rangle]$

for $\tilde{\Omega} = \sqrt{\Omega_p^2 + \Omega_c^2}$

The bight states are strongly coupled to both the beams and have a population in the excited state.

7.2.2 Spontaneous emission

The EIT Hamiltonian described above is an ideal unitary Hamiltonian. The system is isolated from any environment. We can account for spontaneous emission from the upper level $|e\rangle$ to the ground state by adding an imaginary term to the Hamiltonian accounting for an irreversible decay. We assume that the state can decay into either ground states. The non-unitary Hamiltonian, with Γ_e being the decay rate from the excited state.

$$\mathrm{H}_{EIT} = \hbar \begin{bmatrix} 0 & 0 & \frac{1}{2}\Omega_p \\ 0 & 0 & \frac{1}{2}\Omega_c \\ \frac{1}{2}\Omega_p & \frac{1}{2}\Omega_c & \Delta + i\frac{\Gamma_e}{2} \end{bmatrix} \quad (7.6)$$

The term Γ_e for the ^{87}Rb excited state that we work with in our experiments is known to be 6.06 MhZ. We are going to be using this value for density matrix simulations described later. The branching ratio, defined as the ratio of decay rates into the ground states $|1\rangle$ and $|2\rangle$ is assumed to be equal to 1. Spontaneous emission from the dark states populate the two ground states equally. Spontaneous emission can drive optical pumping processes but is also a major source of dephasing in quantum computing that we need to consider. Note that the spontaneous emission rate is proportional to the popolation in the excited state $|e\rangle$ which is zero in the dark state. The decay rate from the metastable ground state $2\rangle$ to $|1\rangle$ is very small. The states are known as clock states and the transition between these states have a very narrow linewidth. This can be exploited for quantum computing and atomic clocks. The clock states are often used as qubits for quantum computing.

7.2.3 Density matrix formulation

The density matrix formulation is a standard method in quantum physics for simulating time evolution of quantum systems and calculating expectation values of operators. All simulations and results henceforth discussed are carried out using this procedure. An alternative method is known as the quantum jump method that tracks trajectories of wave functions instead of density matrices. The method is computationally less intensive. However, the density matrix formulation works very well for our as we have a fairly small system of 3 or 4 dimensions.

The density matrix is defined as

$\rho = \sum \rho_{ab} |\psi_a\rangle\langle\psi_b|$

Here $\rho_{ab} = \langle\psi_a|\rho|\psi_b\rangle$, if we have $a = b$, ρ_{aa} gives us population of state $|\psi_a\rangle$ and for $a \neq b$, the terms ρ_{ab} gives us the coherence term between states $|\psi_a\rangle$ and $|\psi_b\rangle$. The diagonal terms of the density matrix are the populations and the off diagonal terms are the coherences.

For our system, described by the EIT Hamiltonian, H_{EIT} the time evolution of the density matrix is give by $\dot{\rho} = \frac{-i}{\hbar}[H_{EIT}, \rho] - \frac{1}{2}\{\Gamma_e, \rho\}$.
Here $[H_{EIT}, \rho] = H_{EIT}\rho - \rho H_{EIT}$, the commutator of the Hamiltonian and the density matrix operators. The term $\{\Gamma_e, \rho\} = \Gamma_e\rho + \rho\Gamma_e$.

In the following chapters we discuss subwavelength localization experiments using a spatially varying coupling beam and a probe beam. Then we discuss theoretical studies of a subwavelength phase qubit gate and experimental progress towards the same.

7.3 Initializing the system to the dark state

For our experiments it is vital that we initialize the system in the dark state. State preparation is vital in quantum computing experiments as well. In this section we go through a few important factors that are vital in ensuring a high fidelity preparation of the dark state.

Typically the probe and coupling pulses are not monochromatic beams, they are pulses with finite turn-on and turn-off times. They are represented as slow variations of the electric field amplitudes, the variations being slow compared to the beam frequencies. We can, in our simulations treat Ω_p and Ω_c as time varying quantities $\Omega_p(t)$ and $\Omega_c(t)$ as the amplitudes vary slowly compared to the atomic dynamics. The

time evolution of the density matrix is give by $\dot{\rho} = \frac{-i}{\hbar}[H_{EIT}(t), \rho] - \frac{1}{2}\{\Gamma_e, \rho\}$.

The discrete family of Hamiltonians is described by $H_{EIT}(t)$. For each instance of time t we have the Hamiltonian described by $H_{EIT}(t)$. The Hamiltonian spectrum is discrete. If the terms $\Omega_p(t)$ and $\Omega_c(t)$ vary slowly compared to the energy splitting between the levels, we satisfy the adiabaticity condition (Kato and Messiah). This is ensured by the adiabatic theorem of Quantum Mechanics which states that "*A physical system remains in its instantaneous eigenstate if a given perturbation is acting on it slowly enough and if there is a gap between the eigenvalue and the rest of the Hamiltonian's spectrum*". Therefore, in order to ensure that our system remains in the same eigenstate throughout the evolution we need to ensure that the frequency of variations in pulse intensity is small compared to the $|B\rangle - |D\rangle$ splitting.
We need to satisfy the conditions.
$|\dot{\Omega}_c| << \frac{1}{|\sqrt{\Delta^2+\Omega_p^2+\Omega_c^2}|}$
$|\dot{\Omega}_p| << \frac{1}{|\sqrt{\Delta^2+\Omega_p^2+\Omega_c^2}|}$

These are the adiabaticity conditions in quantum mechanics. This in general means adjusting the rise and fall times of the pulses to be slow compared to the splittings. Typically the splittings are of the order of ~ 40 MhZ. To ensure adiabaticity condition the turn-on and off rates are kept to around 3 MhZ. This is done by adjusting the spot sizes in the AOMs that act as on/off switches for the beams.

The second issue is a bit more subtle. We need to ensure adiabatic continuity into the dark state of the Hamiltonian. The dark state is the state with zero eigenvalue given by
$|D\rangle = \frac{1}{\tilde{\Omega}}[\Omega_c|1\rangle - \Omega_p|2\rangle]$, for $\tilde{\Omega} = \sqrt{\Omega_p^2 + \Omega_c^2}$

To make sure we adiabatically continue into the dark state we need to make sure the system initializes into the dark state and *adiabatically follow* the state during the

entire duration of the pulses. Typically we initialize the system in the state$|1\rangle$. This is the dark state when the coupling beam is on. It is straightforward to verify that if we turn on the probe beam first we initialize the system in the bright state and with adiabatic pulses the system stays in the bright state. We, therefore, need to turn-on the coupling beam first. This "counter-intuitive" pulse sequence initializes the system in the dark state and throughout the evolution the atom, at-least in principle stays in the dark state.

Population can be transfered between the two ground states using this method as well. The slow transfer of population known as STIRAP (Stimulated Raman Adiabatic Passage) can be implemented by adiabatic pulses as well. If we turn on the coupling beam before the probe, we initialize the state in the dark state $|1\rangle$. Turning on the probe and increasing it's power (again, adiabatically) rotates the dark state in the $|1\rangle$, $|2\rangle$ axis, shifting towards $|2\rangle$ as the probe beam power is increased. This method can be used to transfer population between ground states. Finally if the probe beam is turned-off after the coupling beam we have a population transfer from $|1\rangle$ to $|2\rangle$. The transfer is coherent without any dissipative process involved as in optical pumping. The atom stays in the dark state at all times.

Chapter 8

Subwavelength localization of excitation using EIT

This chapter is a summary of the work presented in [70]. Several technical details are omitted and only the key results and methods are highlighted. The details can be found in the thesis of Jared Miles [81], the lead author in the work mentioned above. This is a follow up of the fantastic work done by the team in [68] where a localized excitation in a spatial extent of $\lambda/8$ was demonstrated using the nonlinear spatial dependence of the dark state under the conditions of EIT. We made several improvements to the experiment and report the results in this work. The improvements included moving to a different laser transition for EIT and a new dipole trap setup.

In this work we experimentally demonstrate the localization of excitation between hyperfine ground states of ^{87}Rb atoms to as small as $\lambda/13$ wide spatial regions. We use ultracold atoms trapped in a dipole trap and utilize electromagnetically induced transparency (EIT) for the atomic excitation. The localization is achieved by combining a spatially varying coupling laser (standing-wave) with the intensity dependence of EIT. Because the width of the localized regions is much smaller than the wavelength of the driving light, traditional optical imaging techniques cannot resolve the localized features. Therefore, to measure the excitation profile, we use

an auto-correlation-like method where we perform two EIT sequences separated by a time delay, during which we move the standing wave.

8.1 Motivation

Neutral atom quantum computing requires addressing qubits with electromagnetic radiation. Addressability resolution is limited by the Abbe diffraction limit, i.e atoms need to be spaced at a separation of atleast $\lambda/2$ (the diffraction limit) to be addressed individually without affecting neighbouring atoms. If we use ^{87}Rb as qubit atoms this typically limits the atomic spacing to the order of 1 μm, the addressing wavelength being $780-795$ nm depending on the working transitions. Beating the diffraction limit can help in building large scalable devices as well as implementing two qubit quantum gate operations in which the driving interaction strength (and hence gate speeds) can be increased by reducing spatial separation. The dark state can be prepared with little population transfer to a radiative excited state, which reduces heating and decoherence from spontaneous emission. As the excitation is coherent, dark-state based localization can be achieved using short laser pulses, enabling fast gate speeds. The ideas discussed can, in principle, be extended to high resolution optical imaging which suffers from the diffraction limit and optical lithography techniques. The ideas can be implemented in solid state qubits in quantum dots and NV centers.

8.2 Dark state and localization

Ideas behind dark state based localization stem from the non-linear dependence of the dark state in a Lambda scheme on the intensity of the coupling beam. We start

with the standard EIT Hamiltonian (details in 6)

$$H_{EIT} = \hbar \begin{bmatrix} 0 & 0 & \frac{1}{2}\Omega_p \\ 0 & 0 & \frac{1}{2}\Omega_c(x) \\ \frac{1}{2}\Omega_p & \frac{1}{2}\Omega_c(x) & \Delta \end{bmatrix} \tag{8.1}$$

where we have chosen a spatially varying coupling beam intensity giving rise to a spatially varying coupling beam Rabi frequency $\Omega_c(x)$. We have the dark state solution of the Hamiltonian

$|D\rangle = \frac{1}{\tilde{\Omega}}[\Omega_c(x)|1\rangle - \Omega_p|2\rangle]$

with $\tilde{\Omega} = \sqrt{\Omega_p^2 + \Omega_c(x)^2}$.

The population in the excited state $|2\rangle$ is given by

$$|\langle 2|D\rangle|^2 = \frac{\Omega_p^2}{\Omega_p^2 + \Omega_c(x)^2} = \frac{I_p}{I_p + I_c} \tag{8.2}$$

with I_p and I_c being the probe and coupling beam intensities respectively.

We can plot the spatial dependence of the population of the state $|2\rangle$ as a function of distance giving the characteristic non-linear dependence.

This non-linear dependence on beam intensities, can be exploited as shown in figure 8.2 to localize excitations.

8.3 Localization of atomic excitation

In this section we discuss strategy to create spatially varying coupling beam intensity profile. We bulid on proposals by Agarwal and colleagues [71], Lukin [65] and previous work in this group (theory[72] and experiment [68]). The first experiment that

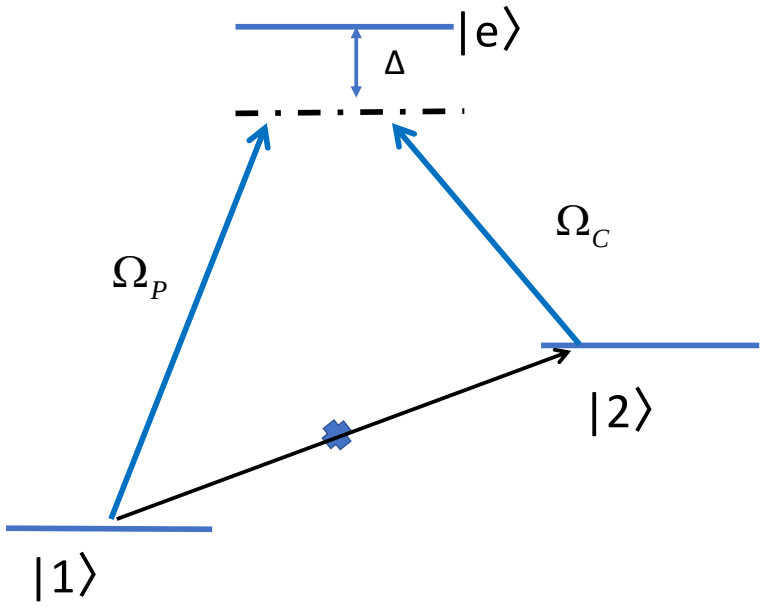

FIGURE 8.1: The Λ scheme of the atom. Transition from $|1\rangle$ to $|2\rangle$ is forbidden. The corresponding Hamiltonian is given by 8.1.

observed dark-state-based localization was performed in a vapor cell by Scully and collegaues [73] and a proof of concept experiment reported in this group using ultra-cold atoms trapped inside a magneto-optical trap (MOT) [74].

A simplified energy level diagram is shown in Fig 8.1. Two laser pulses are the coupling beam (with Rabi frequency Ω_c) and the probe beam (Ω_c) They interact with a three level atomic system. The two lower states, states $|1\rangle$ and $|2\rangle$, are the metastable ground states with long lifetimes, and they are coupled to each other through the radiative excited state $|e\rangle$. The atoms are initialized into state $|1\rangle$ before applying a counter intuitive pulse sequence where the coupling beam is turned on before the probe beam. The conditions for adiabatic following into the dark state of EIT is discussed in Chapter 7. The dark state has no population in the excited state $|e\rangle$. From Eq. 8.2 and Fig. 8.3 we can see that the populations of states $|1\rangle$ and $|2\rangle$ are determined by the Rabi frequencies, and therefore the intensities of the two lasers. The population in state $|2\rangle$ increases as the ratio I_c/I_p decreases. The population of

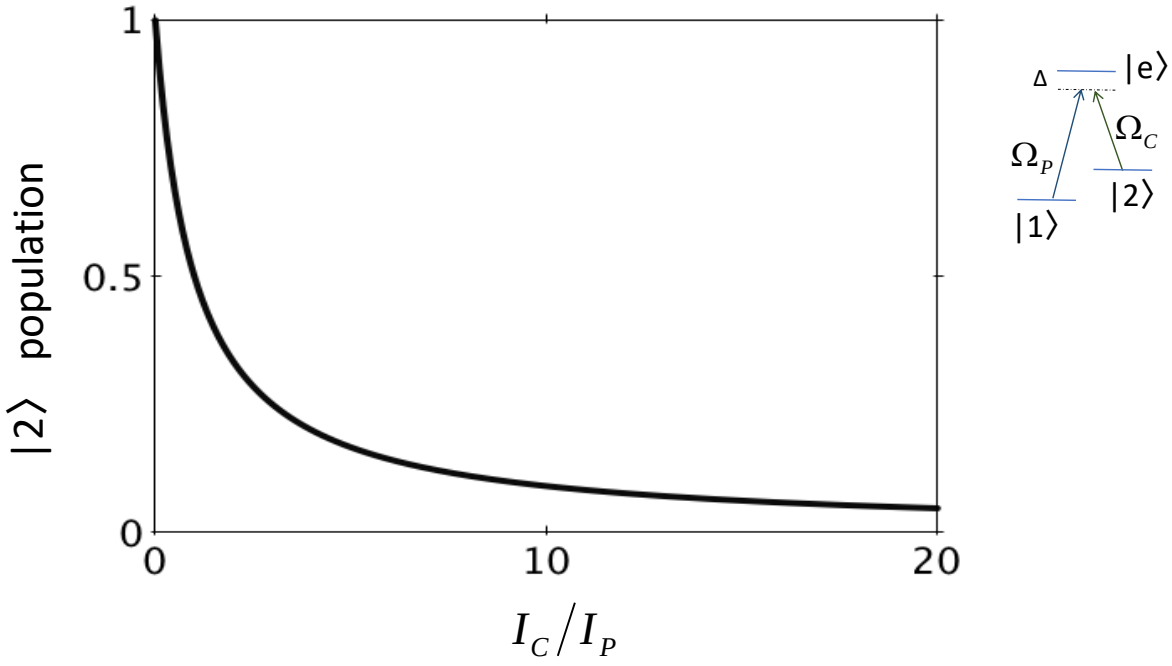

FIGURE 8.2: Variation of population in $|2\rangle$ with the ratio of probe and coupling beam intensities.

state $|2\rangle$ can then be tightly localized if the coupling laser goes through an intensity minimum. A straightforward approach for achieving producing a spatially varying coupling laser is to use a standing-wave [71, 65]. This scheme is demonstrated in Figures 8.3 and 8.4 where a strong transfer to state $|2\rangle$ occurs near the nodes of the coupling standing wave and away from the nodes atoms mostly remain in state $|1\rangle$. The probe beam intensity (I_p or Ω_p) is held constant.

8.4 Experimental procedure

The description of MOT/dipole trapping procedure is given in 3. A schematic of the experimental set up in our lab is given in Fig. 8.5.

The experiment is performed in our 14-port stainless-steel ultra-high vacuum

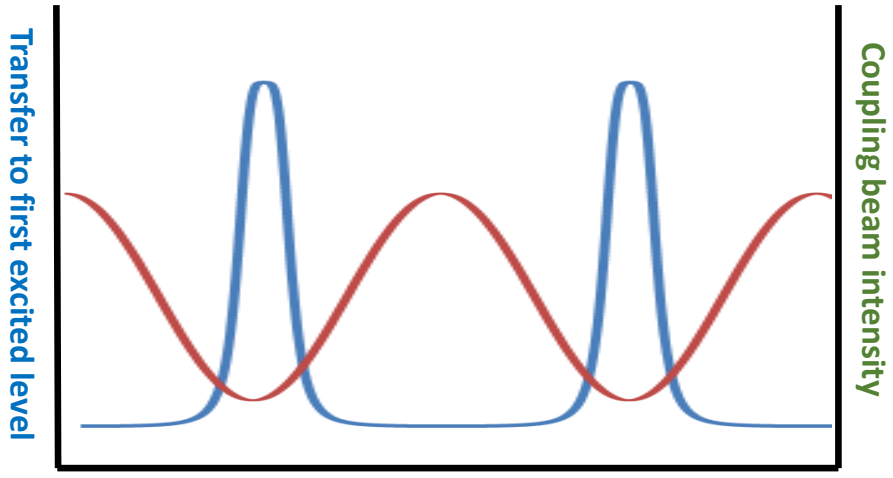

FIGURE 8.3: Variation of population in $|2\rangle$ with the ratio of probe and coupling beam intensities.

chamber. The MOT is generated from three retro-reflected beams each having 50 mW of power in two directions and 26 mW in the beam alone the axis of the anti-Helmholtz colis. The beams have a diameter of 3 cm. The beams originate from a semiconductor tapered amplifier seeded by a home-built external-cavity diode laser (ECDL). The ECDL is locked to the D1 line of ^{87}Rb near a wavelength of 795 nm using saturated absorption locking. The far-off resonance trap (FORT)/optical dipole trap for the atoms is formed using a 1064 nm diode seeding a 1055 nm semiconductor tapered amplifier . The FORT beam is focused to a $1/e^2$ beam radius of 25 μm and is overlapped with the MOT. Once the atoms are trapped in the FORT, they are evaporatively cooled for about 200 ms down to a temperature below 1 μK by reducing the FORT potential depth to $\sim$ 10 μK. At the end of evaporative cooling we have a few thousand atoms in the dipole trap.

The coupling and probe lasers are both generated from the same ECDL [74, 68]. In order to have a perfect EIT the phase and frequency fluctuations in the probe and coupling beams should match. Semi-conductor tapered amplifiers and high-frequency

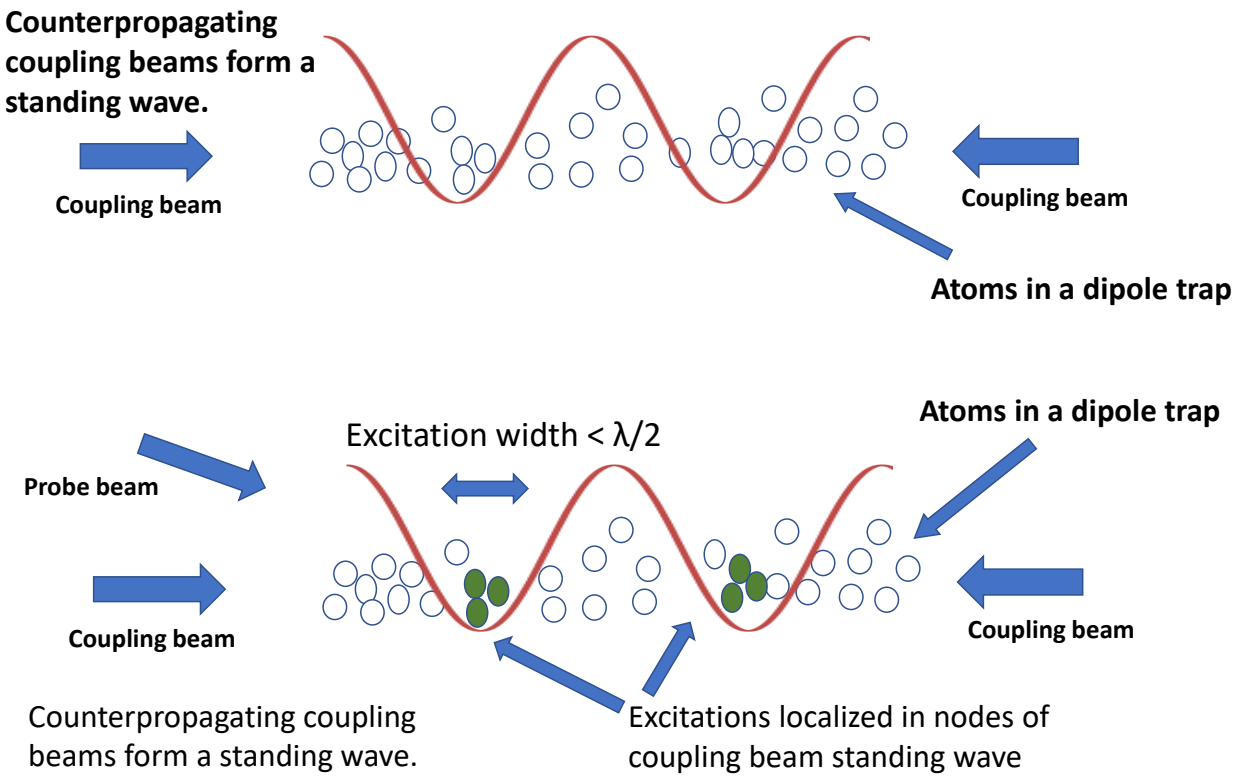

FIGURE 8.4: Spatial Variation of population transfer to $|2\rangle$.The red solid lines indicate the spatial variation of the coupling beam intensity. The excitations are localized near the nodes of the standing wave.

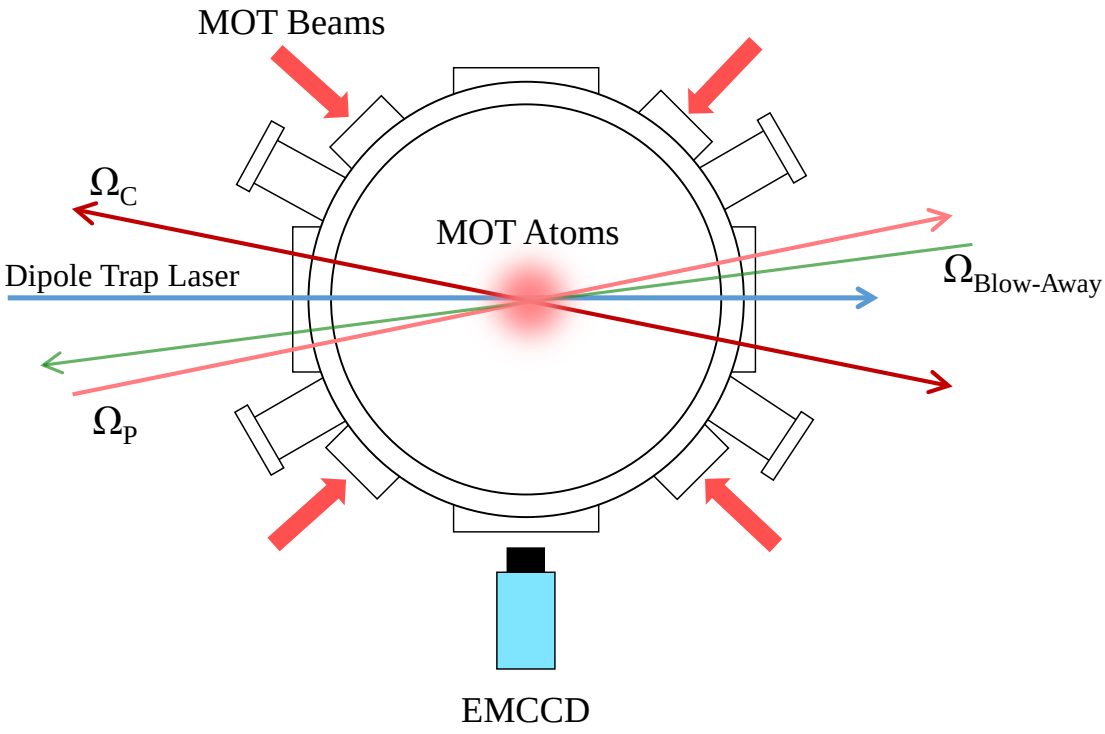

FIGURE 8.5: An electron-multiplying CCD camera (EMCCD) images the remaining atoms left in the FORT after an EIT experiment. The laser $\Omega_{blow-away}$ is used for the measurement protocol, and heats and removes any atoms that are in the $F = 2$ level after the experimental pulse sequence.

acousto-optic modulators are then used to produce the required frequency spacing of 6.834 GHz and sufficient optical power in each beam. As shown in Figure 8.6, the two lasers form an EIT Λ with the levels $5S_{1/2}, F = 1$ to $5P_{1/2}, F' = 2$ being coupled by the probe beam and levels $5S_{1/2}, F = 2$ to $5P_{1/2}, F' = 2$ transition addressed by the coupling beam. These are the transitions in the D1 line of ^{87}Rb.

The decay rate of the excited $5P_{1/2}$ level is $\Gamma = 2\pi \times 5.75$ MHz. The polarization of the two beams are linear and orthogonal to one another. The quantization axis chosen along the propagation direction of the probe laser beam. This allows atoms to transfer between identical ground state m levels via the $m' = m + 1$ excited state. Note that this is true because a linearly polarized light in a direction perpendicular

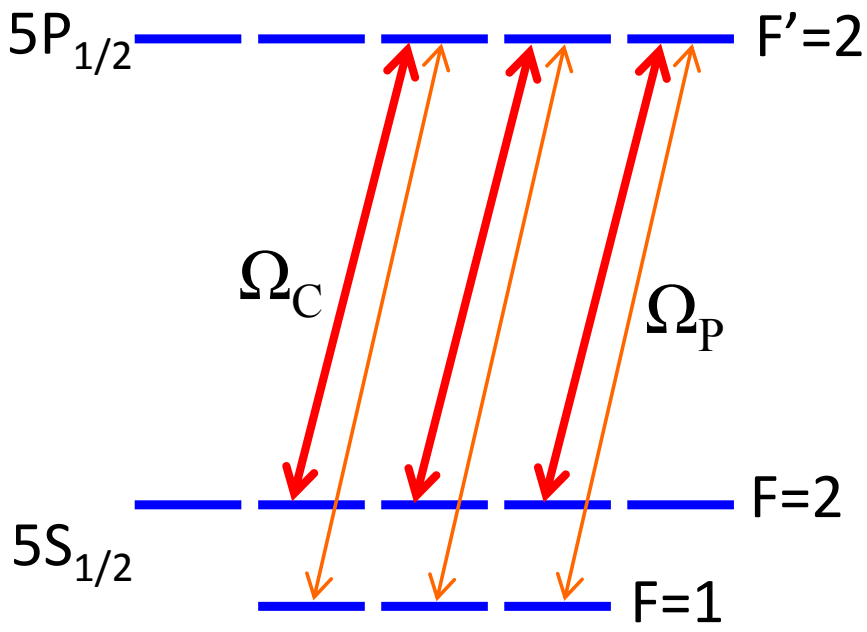

FIGURE 8.6: The Λ scheme in ^{87}Rb

to the quantization axis can be written as a sum of left and right circularly polarized light and the right circularly polarized light couples $m' = m + 1$ while left circularly polarized component couples $m' = m - 1$. The atoms are initialized in the $F = 1$ level and then transferred to $F = 2$ through three parallel m-level channels (forming three Λ systems).

8.5 Experimental results

8.5.1 Dark state preparation

We did experiments to measure population transfer to the $F = 2$ level under conditions of EIT. For this we use only one coupling beam. The off-resonance experiments were

carried out with a single photon detuning of $\Delta\omega = 5.2\Gamma \sim 30$ Mhz.The experiments were performed using coupling and probe beams with pulse widths of 150 ns and 100 ns, respectively, keeping the counterintuitive pulse sequence in mind.

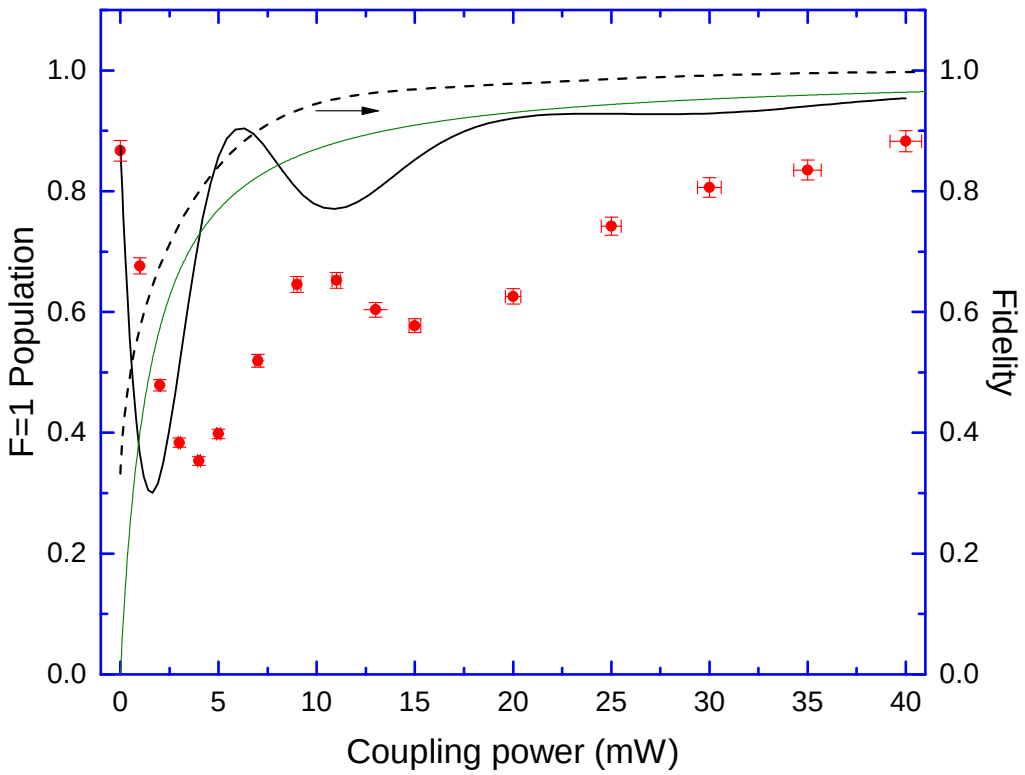

FIGURE 8.7: The population remaining in the $F = 1$ level after a single EIT pulse as a function of coupling laser power is varied. This experiment is performed using a single coupling laser. The solid black line is the result of numerical simulations of the density matrix without any adjustable parameters, i.e., all the beam parameters that are used are experimentally measured. The solid green line shows the $F = 1$ level population using the ideal dark state solution. The dotted line is the fidelity of dark state preparation, calculated in the simulations and the ideal dark-state density matrix.

The lasers are turned off simultaneously. The detuning ensures less spontaneous emission due to probe beam. The calculated probe laser Rabi frequencies for the three channels are $\Omega_p = 1.95\Gamma$ $(m_F = -1 \rightarrow m_{F'} = 0)$, $\Omega_p = 3.33\Gamma$ $(m_F = 0 \rightarrow m_{F'} = 1)$

and $\Omega_p = 4.7\Gamma$ ($m_F = 1 \rightarrow m_{F'} = 2$). We experimentally measure transfer to $F = 2$ level. After a EIT pulse we blow away atoms at $F = 2$ level using a resonant blow away beam ($\Omega_{blow-away}$). Results are shown in Fig. 8.7 ([70]).

For a coupling beam power of 40 mW calculated coupling laser Rabi frequencies for the three channels are $\Omega_c = 18.2\Gamma$ ($m_F = -1 \rightarrow m_{F'} = 0$), $\Omega_c = 18.2\Gamma$ ($m_F = 0 \rightarrow m_{F'} = 1$) and $\Omega_c = 14.1\Gamma$ ($m_F = 1 \rightarrow m_{F'} = 2$). We experimentally measure transfer to $F = 2$ level. In the figure the fidelity is calculated using a trace distance measure $tr\sqrt{\sqrt{\sigma}\rho\sqrt{\sigma}}$ [76].

At low coupling intensities, the EIT pulse is so short that the system does not have sufficient time to reach the dark state, resulting is low atomic transfer to the $F = 2$ level. As the coupling laser intensity is increased, the transfer peaks and then drops again. The oscillations are an indication of non-adiabatic transitions before reaching the dark state. On the whole, we estimate a steady state dark state fidelity of $\sim .95$ after the oscillations die down.

8.6 Auto-Correlation Measurement Protocol

In this section we discuss our measurement protocol for localization experiments. A similar protocol is used to 'image' subwavelength excitation structures in [68].

In the protocol two EIT transfer sequences separated by time τ are used. A pair of counter propagating lasers produce the coupling beam standing wave and the frequencies of these two beams differ by an amount δf.

The first EIT pulse transfers atoms to the $F = 2$ level. The transfer depends on coupling beam intensity which varies with position as $\sim \sin^2(2\pi x/\lambda)$. Thus we end up having a transfer as a function of position according to the dark state equation 8.2. After the first EIT pulse, the blow-away laser is turned on. The beam 'blows-away' atoms in the $F = 2$ level, being resonant with the $F = 2 \rightarrow F' = 3$ transition. The

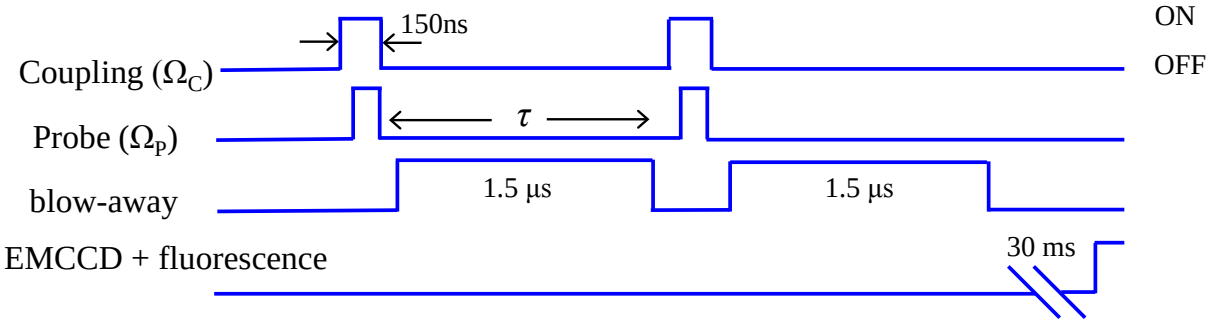

FIGURE 8.8: Timing of the auto correlation experiment protocol. The first EIT pulse sequence transfers some atoms to the $F = 2$ level. The blow-away beam heats the atoms that have been transferred, ejecting them from the trap. The procedure is repeated with the second EIT pulse, after which the remaining ($F = 1$) atoms in the trap are imaged with a fluorescence measurement.

atoms in $F = 2$ after the first EIT pulse are ejected out of the trap. Before the second EIT pulse the standing wave moves by an amount $\delta x = (\lambda/2)\delta f \tau$. The number of atoms transferred by the second EIT pulse at a position depends on the new intensity of the shifted standing wave pattern as well as the number of atoms remaining after the application of the blow away beam. After the second EIT pulse, the blow-away beam is turned on again, blowing away atoms transferred by the second EIT pulse to $F = 2$ level. The total number of atoms that remain in the $F = 1$ level are then measured with the EMCCD camera by a fluorescence measurement using the $F = 2$ to $F' = 3$ cycling transition. The procedure is repeated by varying δf, giving a correlation between the excitation profiles generated by the two EIT pulses. This correlation measurement enables us to infer the spatial profile of the excitation that results from a single EIT pulse. We neglect atomic motion during the duration τ between the two EIT pulses. This is a valid assumption for atoms cooled to around $1\mu K$. Figure 8.8 shows the pulse sequence.

Figure 8.9 shows the results of the autocorrelation experiment. The coupling beam power in the standing wave varies from 0 mW to 10 mW in 8.9(a) and 0 mW to

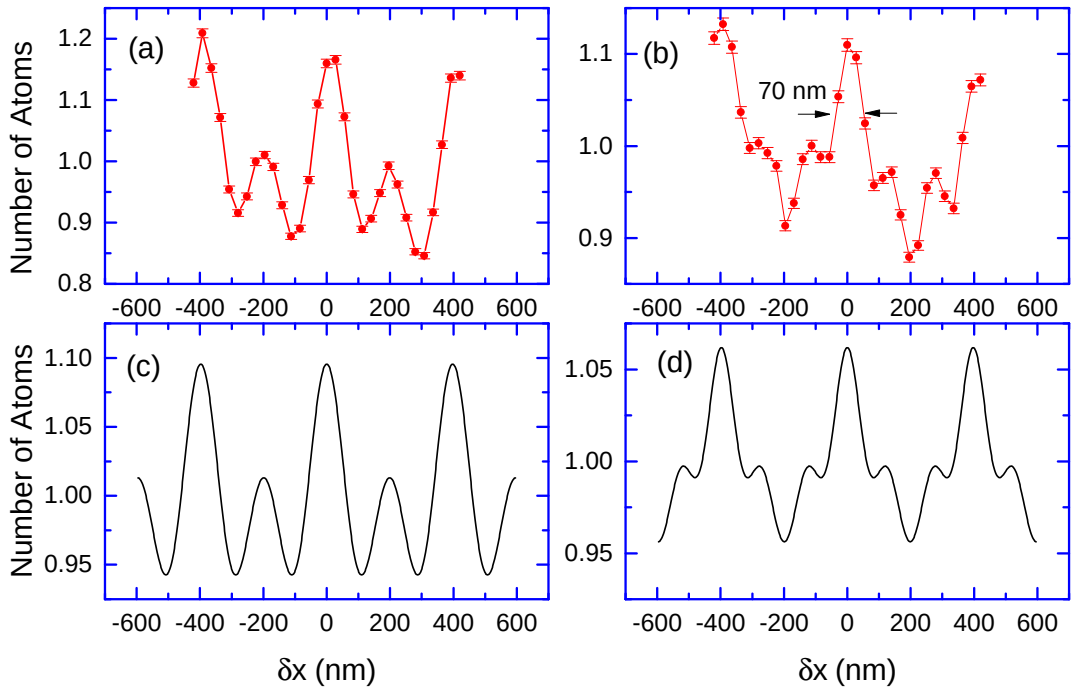

FIGURE 8.9: Results of the autocorrelation experiment. The coupling beam power in the standing wave varies from 0 mW to 10 mW in 8.9(a) and 0 mW to 20 mW in 8.9(b).

20 mW in 8.9(b). This data is recorded over a scanning distance of approximately two periods of the standing-wave. The horizontal axis is $\delta x = (\lambda/2)\delta f \tau$, translations δx being generated by a varying the frequency difference δf. To infer the actual transfer curves from the autocorrelation profile, we simulate the experimental correlation traces by keeping the maximum power of the coupling laser standing wave as an adjustable parameter; there are no other fit parameters in these simulations. These simulation results are displayed in figures 8.9 (c) and (d). The correlation traces show subwavelength transfer with FWHM $\pm \sim 70$ nm. The two experimental traces are best captured with the coupling laser power ranging from 0 mW to 3 mW [Figs.8.9 (c)] and 0 mW to 7.5 mW [Figs. 8.9 (d)], respectively.

Figure 8.10 shows a numerical solution of the density matrix equations for the

EIT pulse sequence at each point along the standing-wave spatial profile, generating the population transferred to the $F = 2$ level as a function of position. This spatial transfer pattern is convoluted with a itself at different spatial shifts of the standing wave. A velocity spread is incorporated by using the Maxwell Boltzmann velocity distribution at 1μK.

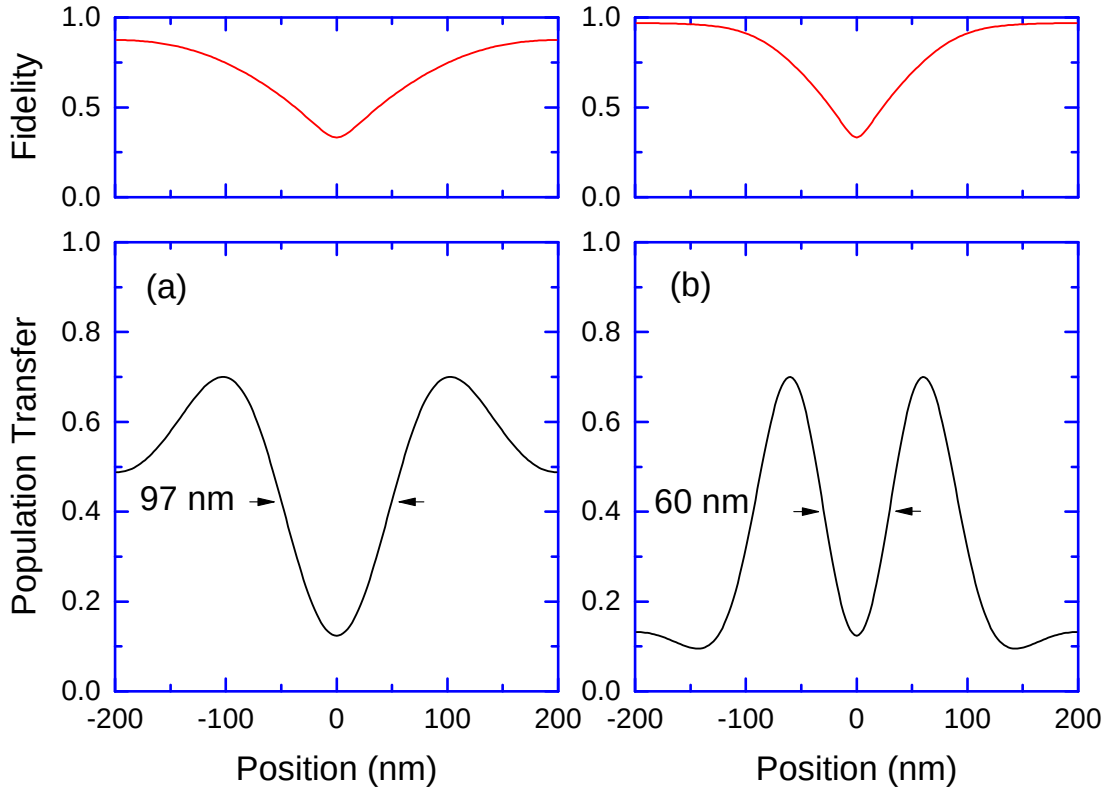

FIGURE 8.10: The density matrix simulation of the inferred population transfer to the $F = 2$ level as a function of the position in the standing-wave for a coupling power range of (a) 0 mW to 3 mW and (b) 0 mW to 7.5 mW. Position = 0" in the horizontal axis coincides with the intensity minimum of the standing-wave and the results are displayed over one period. The simulated correlation traces agree well with the experimental results as shown in Fig. 8.9. In (b), the middle feature has a width of $60nm$ or $\lambda/13.3$, a factor of 6.6 better than the diffraction limit. The top plots show the simulated fidelity of the system to be in the dark state.

There is good agreement between the experimental results and the simulations of Fig. 8.9 and Fig. 8.10. For the 0 mW to 3 mW power range, the middle feature of Fig. 8.10(a) has a width of 97 nm or $\sim \lambda/8$. The 0 mW to 7.5 mW range transfer profile [Fig. 8.10(b)] has a width of 60 nm or $\sim \lambda/13.3$, 6.6 times sharper than the diffraction limit. The top plots in Fig. 8.10 show the estimated dark state fidelity using density matrix simulations. The dark state fidelity is poor at the nodes where the coupling beam intensity is low leading to a significant leakage to the bright states leading to coupling with the excited state and hence unwanted spontaneous emission.

The next set of experiments were carried out with on resonance probe and coupling beams, i.e the single photon detuning $\delta\omega = 0$. Being on resonance reduces the non-adiabatic corrections to the dark state. The pulse widths for both the coupling and probe beams were kept the same, but the rise times of the pulses were increased by a factor of two (from about 20 ns to 40 ns), reducing non- adiabatic corrections to the dark state by a significant amount. A pumping scheme to reduce the three parallel EIT channels (Figure 8.5) to one was also carried out. we pump the atoms into the $F = 1; m = 0$ state using an optical pumping beam. For this purpose, we apply a DC magnetic field of magnitude $3G$ along the propagation direction of the EIT laser beams. The magnetic field direction is the quantization axis and lifts the degeneracy of the m-levels through the Zeeman shift (Fig. 8.11) . A laser, linearly polarized along the direction of the magnetic field is then applied. This laser pumps the atoms from the $F = 1, m = \pm 1$ states into the $F = 1, m = 0$ state via the $F' = 2$ excited level. The propagation direction of the optical pumping laser is roughly perpendicular to the dipole trap laser beam direction.

The results of transfer to excited state and dark state overlap using a single coupling beam is shown in Fig. 8.12. We find a lot of oscillations seen before in Fig. 8.7 have died down indicating less non-adiabatic effects. Due to the pumping scheme mentioned above we measure population in $F = 1, m = 0$ level, i.e a single

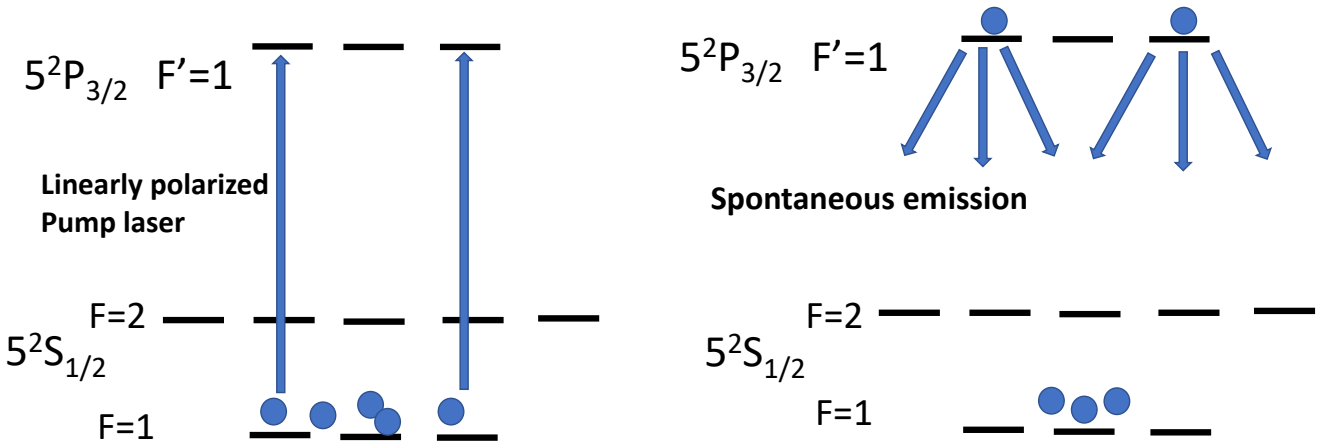

FIGURE 8.11: m-level pumping by linearly polarized light. The $F = 1m_F = 0$ to $F' = 1m_F = 0$ transition is a forbidden. After pumping the excited atoms can decay to either of the $F = 2$ or $F = 1$ ground state levels. Atoms in $F = 2$ level is pumped out using the coupling beam on resonant with the $F = 2$ to $F' = 2$ transition. After this sequence atoms enf up in $F = 1, m = 0 level$

EIT channel is involved in the experiment.

The results of the two pulse EIT experiments are shown in figure 8.13 and the inferred transfer profiles are shown in figure 8.14. For these experiments the coupling beam standing wave minima was kept to $1mW$ to ensure better dark state fidelity at all positions. Figure 8.13 shows the experimentally measured correlation traces for four different ranges of the standing wave: (a) 1 mW to 10 mW, (b) 1 mW to 20 mW, (c) 1 mW to 40 mW, and (d) 1 mW to 80 mW , with coupling beam Rabi frequency (a) 2.89Γ to 9.11Γ (b) 2.89Γto 12.9Γ (c)2.89Γ to 18.2Γ and (d) 2.89Γto 25.8Γ respectively. The solid black lines are the numerical simulations of the density matrix without any adjustable parameters.

Figure 8.14 shows the inferred population transfer along the standing wave after a single EIT pulse for the four experimental conditions of Fig. 8.13. These population

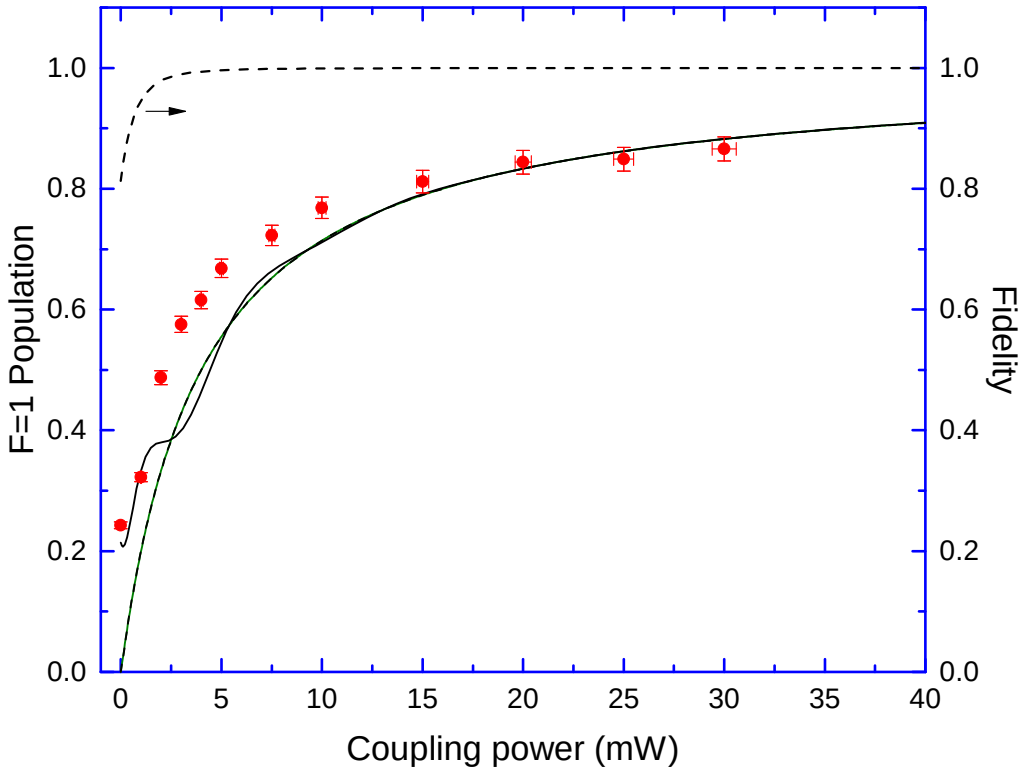

FIGURE 8.12: The population remaining in the $F = 1$ level after a single EIT pulse as the coupling laser power is varied. This experiment the EIT lasers having single photon detuning $\delta\omega = 0$. The solid black line is the result of numerical simulations of the density matrix without any adjustable parameters. The solid green line shows the $F = 1$ level population using the ideal dark state solution. The dotted line is the fidelity of dark state preparation, which approaches unity for coupling laser power values above 2 mW. This experiment is performed with the atoms initially optically pumped into the $F = 1; m = 0$ state, there is a single EIT channel. The probe beam Rabi frequency $\Omega_p = 5.78\Gamma$ and for coupling beam power of 40 mW, the calculated coupling Rabi frequency is $\Omega_p = 18.2\Gamma$

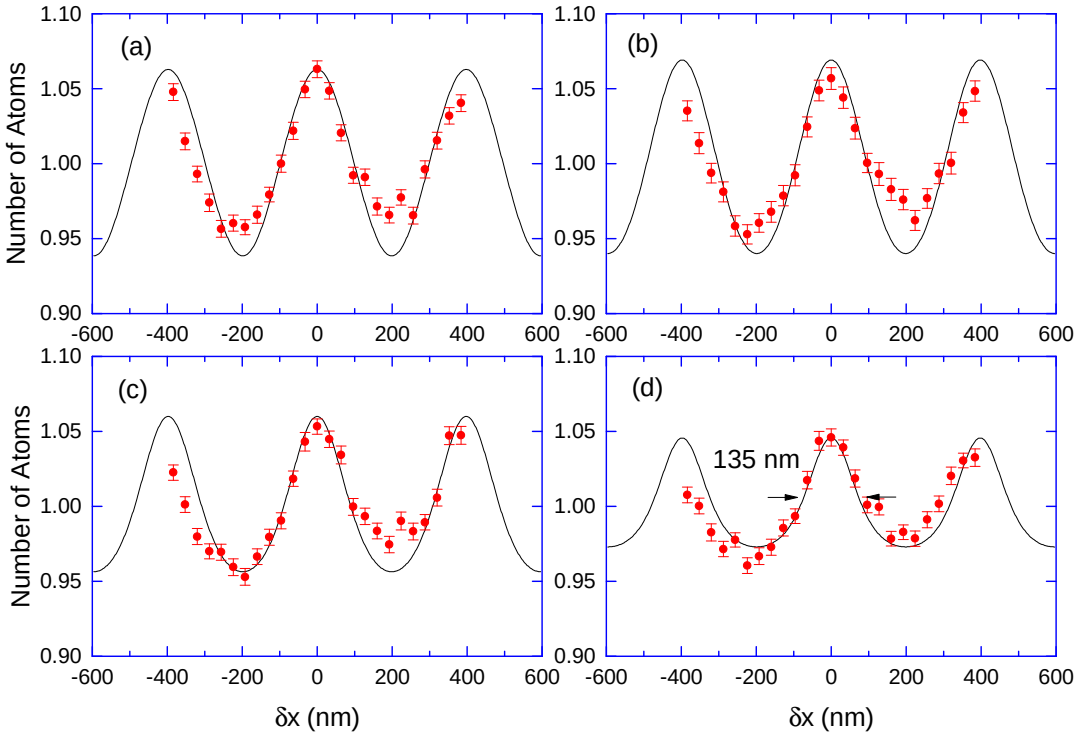

FIGURE 8.13: Experimentally measured correlation traces for four different ranges of the standing wave: (a) 1 mW to 10 mW, (b) 1 mW to 20 mW, (c) 1 mW to 40 mW, and (d) 1 mW to 80 mW , with coupling beam Rabi frequency (a) 2.89Γ to 9.11Γ (b) 2.89Γto 12.9Γ (c)2.89Γ to 18.2Γ and (d) 2.89Γto 25.8Γ respectively. The solid black lines are the numerical simulations of the density matrix without any adjustable parameters.

transfer results are used to generate the simulations of the correlation traces as shown in Fig. 8.13. For coupling power range of 1 mW to 80 mW, Fig. 8.14(d) shows that the transfer is localized to a region with a width of 70 nm, which is a factor of 11.3 times smaller than the wavelength of the coupling and probe lasers.

In conclusion, we experimentally transferred atoms between hyperfine levels of cold ^{87}Rb atoms within a spatial width of 70 nm, a factor of 11.3 times smaller than the wavelength of the lasers used to perform the transfer, thereby overcoming the standard diffraction limit. This was achieved using $150 - ns$ EIT pulses and with an inferred

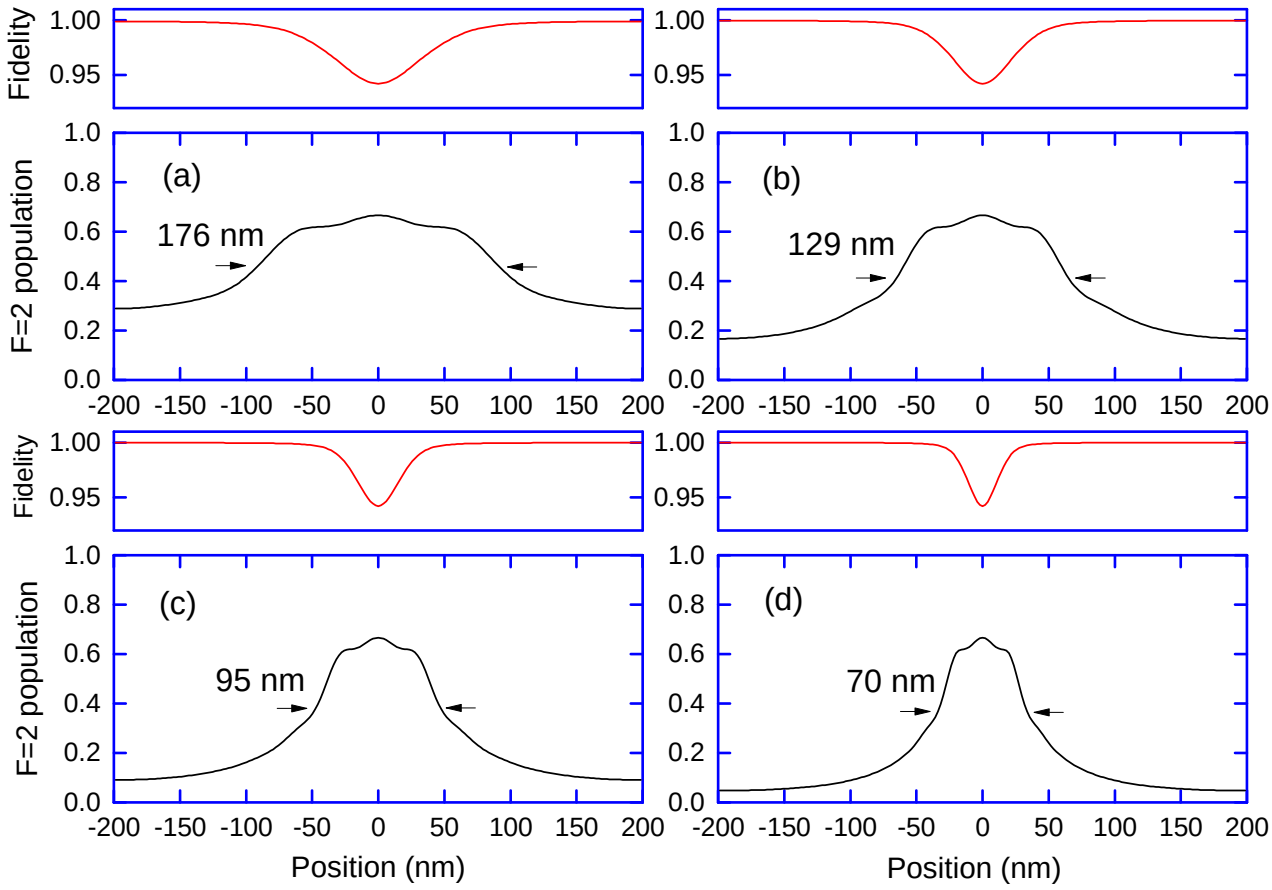

FIGURE 8.14: The inferred population transfer to the F = 2 level as a function of the position in the standing-wave for coupling power ranges same as those displayed in Fig. 8.13. Zero in the horizontal axis coincides with the intensity minimum of the standing-wave and the results are displayed over one period. These simulated features produce the correlation traces that match the experimental results as shown in Fig. 8.13. In (d) [coupling laser power range of 1 to 80 mW], the transfer is localized to a region with a width of 70 nm, $\sim$ 11.3 times smaller than the wavelength of the coupling and probe beams. The top plots show the calculated fidelity of the system to be in the dark state. The fidelity is above 94% at all points along the standing wave.

dark-state preparation fidelity exceeding 94% across the spatial extent of the atoms in the region of interest. As discussed in Chapter 7, dark-state based approach has several advantages that may be especially useful for quantum computing experiments in which nanoscale-level addressing with low decoherence and spontaneous emission losses are required. Experiments discussed here (published in [68, 70]) as well as works such as [82] that implements a similar protocol in a solid state system, provide a stepping stone towards such realizations of dark state based quantum information processing.

Chapter 9

Coherent control and quantum gates using EIT

We discuss methods to use the dark state of EIT to generate coherent control of quantum state of neutral atoms. The non linear dependency of the dark state on the intensities of the coupling beam is going to be the key factor. The inspiration behind the scheme is the work presented in [65]. Dark state based protocols are presented in [66] and [67]. Experimental progress is discussed in [68] and [70] and in the next chapter

9.1 The phase qubit

Here we describe a phase gate protocol that applies a phase on a qubit in an array. The key feature of this protocol is its operation with subwavelength spatial resolution and minimal error due to spontaneous emission. A schematic of the level structure is given in figure 9.3. There are two qubit levels $|0\rangle$ and $|1\rangle$ with states $|1\rangle$, $|r\rangle$ and $|e\rangle$ forming the Λ system of the EIT Hamiltonian. The Hamiltonian, in the co-rotating frame after making the RWA in the basis $|0\rangle$, $|1\rangle$, $|r\rangle$ and $|e\rangle$ is given by (see Chapter 7 for details). In our Hamiltonian we assume the coupling beam is in the form of a spatially varying standing wave giving a spatially varying Ω_c. Both the probe and

coupling beams are pulses of finite duration and the corresponding Rabi frequencies are therefore functions of time.

$$H(x,t) = \hbar \begin{bmatrix} 0 & 0 & 0 & 0 \\ 0 & 0 & 0 & \frac{1}{2}\Omega_p(t) \\ 0 & 0 & \delta & \frac{1}{2}\Omega_c(x,t) \\ 0 & \frac{1}{2}\Omega_p(t) & \frac{1}{2}\Omega_c(x,t) & \Delta + i\frac{\Gamma_e}{2} \end{bmatrix} \tag{9.1}$$

For perfect EIT we need two photon detuning $\delta = 0$

If we start in the initial state

$|\psi(t=0)\rangle = \frac{1}{\sqrt{2}}[|0\rangle + |1\rangle]$

The time evolution over a pulse duration τ is given by

$|\psi(t)_{final}\rangle = e^{-\int_\tau iH(x,t)dt}|\psi(t=0)\rangle$

At the node of the standing wave (assume $\Omega_c = 0$ for simplicity) we can apply a phase ϕ by Stark shift on atom 1, the atom located at the node. For $\tau \sim \phi\frac{\Delta}{\Omega_p^2}$ we have $|\psi(t)_{final}\rangle = e^{-\int_\tau iH(x,t)dt}|\psi(t=0)\rangle = \frac{1}{\sqrt{2}}[|0\rangle + e^{i\phi}|1\rangle]$.

For the atom located away from the node adiabatic pulses ensure that the atom always remain in the dark state and is thus transparent to both beams. The atom sees no phase shift.

For atom 2 we have

$|\psi(t)_{final}\rangle = e^{-\int_\tau iH(x,t)dt}|\psi(t=0)\rangle = \frac{1}{\sqrt{N}}[|0\rangle + |D(x,t)\rangle]$ where the dark state of the system $|D(x,t)\rangle \sim [\Omega_c(x,t)|1\rangle - \Omega_p(t)|r\rangle]$

The system remains in the dark state at all times provided the adiabaticity conditions (described in 7) is satisfied. We can calculate a region of excitation, the spatial extent

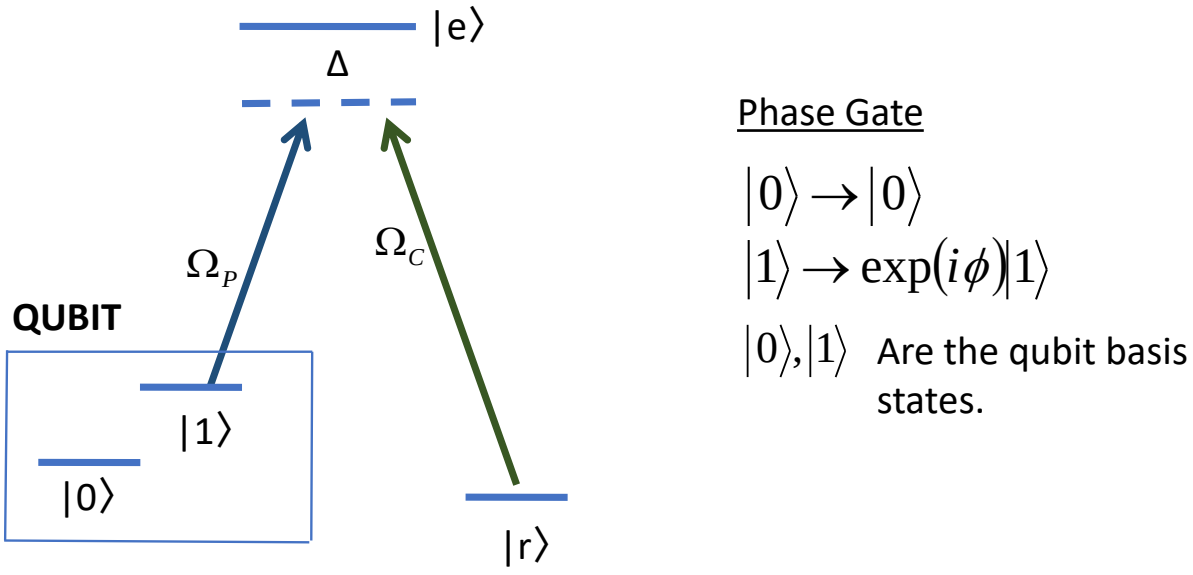

FIGURE 9.1: The qubit level schematic. Qubit state $|1\rangle$ is one of the states of the Λ system addressed by the probe beam detuned by Δ from the excited state $|e\rangle$.

around the node where we expect active phase gate operation. This is given by

$$R_{exc} = \frac{\Omega_p}{\Omega_{c,max} k} \tag{9.2}$$

where $k = \frac{2\pi}{\lambda}$ with λ being the wavelength of the coupling beam. $\Omega_{c,max}$ correspponds to Rabi frequency at the position of peak coupling beam intensity. We can see that the region of excitation can be made arbitrarily small by increasing the peak coupling beam intensity.

9.2 Phase qubit in a Rb array

In this section we discuss implementation of the phase qubit with subwavelength resolution in an array of Rb single atoms. We carry out density matrix simulations

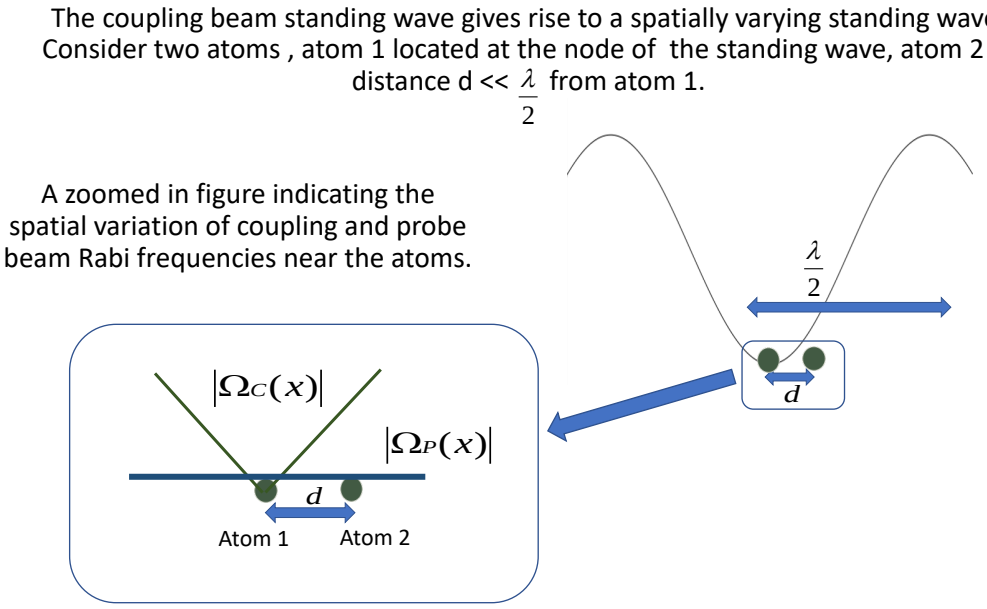

FIGURE 9.2: Spatial variation of probe and coupling beam intensities around the atoms. (Phys. Rev. Lett. 100, 093005 (2008))

with real experimental parameters. The time evolution of the density matrix is give by $\dot{\rho} = \frac{-i}{\hbar}[H_{EIT}(t), \rho] - \frac{1}{2}\{\Gamma_e, \rho\}$.

Here Γ_e is a matrix that takes into account decay from the excited state $|e\rangle$]. We assume equal branching ratios. We analyze the phase gate using realistic experimental parameters. The scheme can be useful for an array of qubits in an optical lattice where the qubit separation of $\lambda_{lattice}/2$ makes it difficult to address qubits by focused laser beams. $\lambda_{lattice}$ is the wavelength of beam forming the optical lattice. For qubit levels we choose

For the qubit level $|0\rangle$ we choose ^{87}Rb ground state $5^2S_{1/2}, F = 1, m_F = -1$ and for level $|1\rangle$ we work with $5^2S_{1/2}, F = 1, m_F = 1$. Level $|r\rangle$ is $5^2S_{1/2}, F = 2, m_F = -1$ and $|e\rangle$ is $5^2P_{1/2}, F = 1, m_F = 0$.

We choose a detuning $\Delta = 15\gamma$ where γ is the decay rate from the excited state

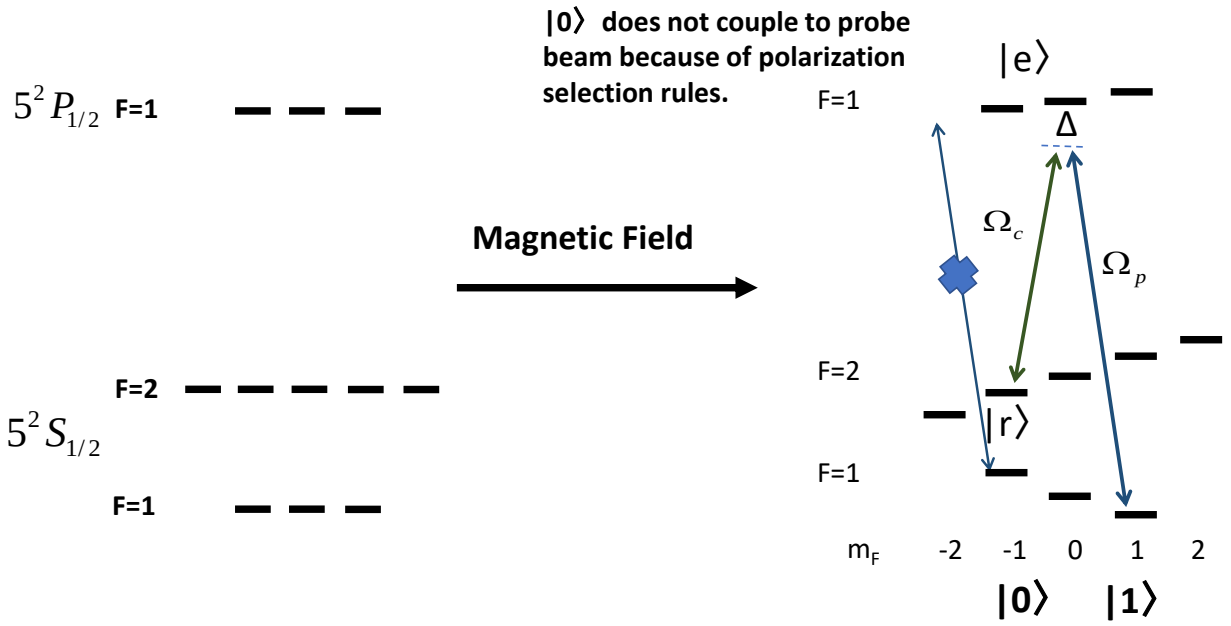

FIGURE 9.3: The qubit levels in a ^{87}Rb atom. A bias field is used to split the m-levels.

$|e\rangle$. The probe pulse duration is assumed to be $\tau = 0.5\ \mu s$, giving a gate speed ~ 2 Mhz. For this we assume a probe power of 5 nW, $1/e^2$ radius of 0.8 mm, giving a probe Rabi frequency of $\Omega_p = 2.6\gamma$. For now we assume ideal case of $\Omega_c = 0$ at the node. We'll discuss errors due to a non zero node in the next section. The Coupling beam power: Standing wave power varied from 0 mW at node to 70 mW maximum standing wave with $1/e^2$ radius of 0.8 mm giving $\Omega_c = 23\gamma$. The ^{87}Rb decay rates, C-G coefficients and dipole matrix elements obtained from D.Steck's Rubidium 87 d line data available online.

Figure 9.4 shows a measure of the phase ϕ applied to as a function of spatial position of the atom relative to the coupling beam standing wave. The region of excitation is clearly subwavelength.

Figure 9.5 shows a measure of the region of phase excitation applied to the second

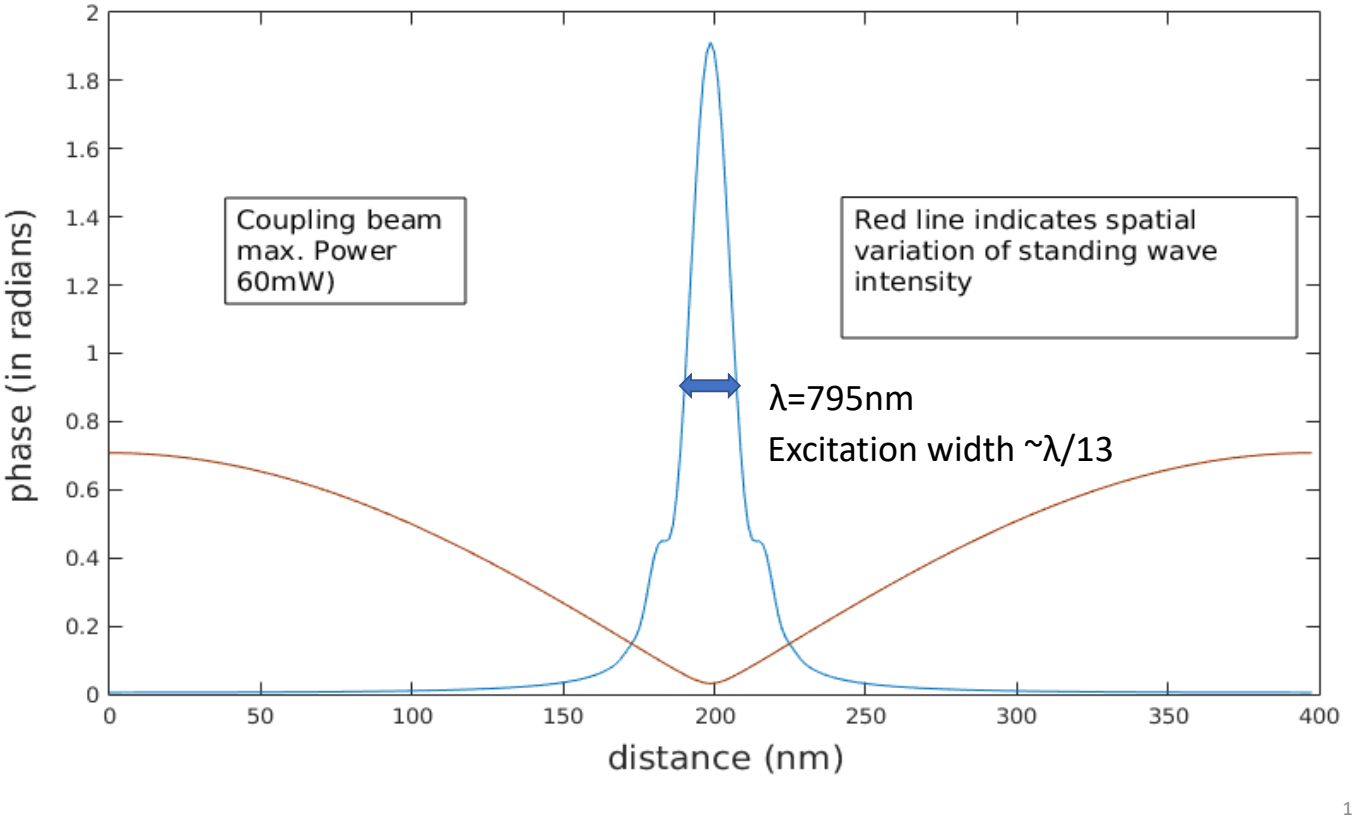

1

FIGURE 9.4: Applied phase as a function of distance . The red line is an indication of coupling beam standing wave. A phase is applied at the node of the standing wave and it drops to zero as we move away form the node.

qubit over the pulse duration as a function intensity maxima of the coupling beam standing wave. The region of excitation is clearly subwavelength and we see that the width decreases as we increase coupling beam power, as expected from Eq.9.2.

9.3 Error budget

To analyze the errors we need to calculate the possibility of leakage to the bright state for atoms that we need to be in the dark state. We analyze the errors separately for

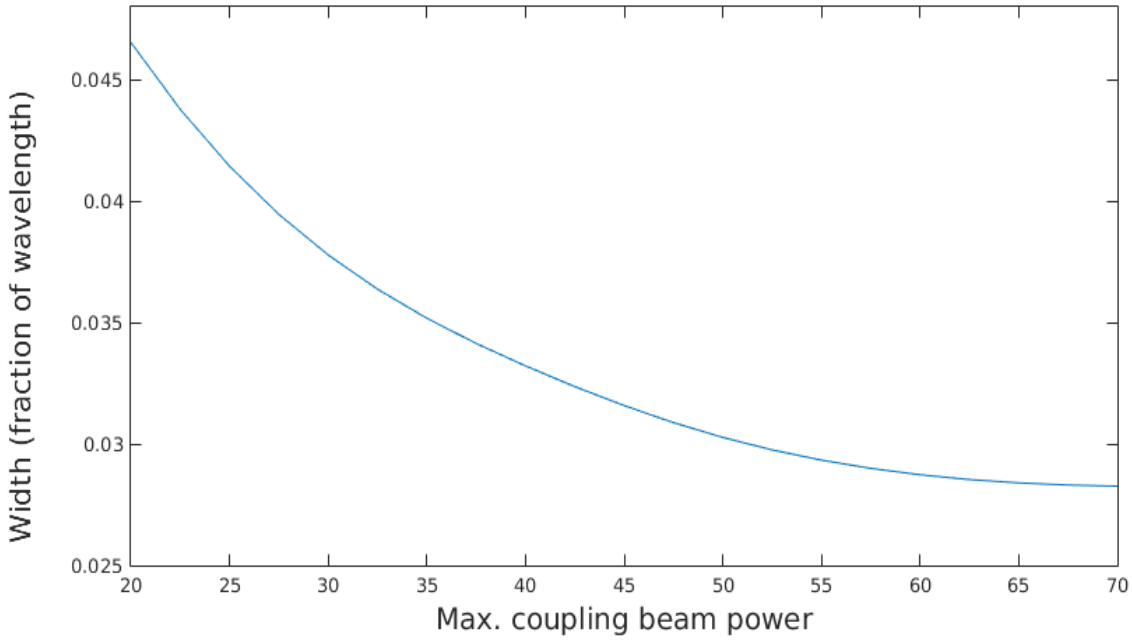

FIGURE 9.5: Region of excitation as a function of maximum coupling beam intensity.

the two atoms.

9.3.1 Error on atom at the node

Spontaneous emission from the excited level

For detuning $\Delta >> \Omega$ we expect probability of excitation to the upper state $|e\rangle$ to be very small. When the Stark-shift beams are turned on there is a small probability of excitation to state $|e\rangle$. The corresponding rate of spontaneous emission is given by $p_e\gamma\tau$, where p_e is the probability of excitation to state $|e\rangle$ and $\tau \sim \Delta/\Omega_p^2$ is the gate time. For detuning $\Delta >> \Omega$ we get $p_e = \gamma/\Delta$ giving an error of γ/Δ. For detuning $\Delta = 15\gamma$ we have an error of 6.67%. This is fairly high but can be improved by increasing power in the probe pulse or by increasing the gate time. This will however affect the region of localization and the coupling beam power needs to be increased

according to eq 9.2. For instance for a gate time of $\tau \sim 12.5\mu s$ we can increase Δ by a factor of 10 and Ω_p by a factor of 2 to reduce the gate error by a factor of 10. This of course requires Ω_c to be increased by a factor of 2 as well.

Non-adiabatic transitions

The pulses have a finite turn-on and off time that needs to be slow compared to the Dark-Bright energy splitting. The non-adiabatic coupling to the bright state is of the order of $(\dot{\Omega}_p/\Delta)$, with $\dot{\Omega}_p$ being a characteristic rise time of the pulse, giving to a probability of leakage to the bright state of $(\dot{\Omega}_p/\Delta)\tau$ and an error of $(\dot{\Omega}_p/\Delta)\tau\gamma$. This is negligible for our experimental parameters.

Non-zero value of coupling beam power at the node

Experimentally we expect the coupling beam intensity at the node to be finite as it is not easy to balance the standing wave intensity exactly. We can realistically achieve $I_c = 1mW$, where I_c is the coupling beam intensity. The error will be due occupation of dark state. Note that this analysis will be important to account for finite atomic velocities even if $\Omega_c = 0$ at the node. If $\Omega_c(0) \neq 0$ the atom may end up in the dark state where no phase is applied. The probability of the atom being in the dark state is $\sim (\frac{\Omega_c(0)}{\Omega_p})^2$ which gives an error of $\sim 0.02\%$.

Intensity fluctuations and timing jitters in the Stark shift beam

We expect fluctuations in beam power to be less than 2%. In that case get an error on the phase $(\delta\phi)/\phi \sim 0.1\%$. This is fairly large and can be managed by keeping gate time low or by intensity stabilization techniques like noise eaters etc. Assuming pulse timing fluctuations of about $\sim 1ns$ we get an error in phase of $\sim 0.04\%$.

9.3.2 Error on atom 2

Non-adiabatic transitions

The pulses have a finite turn-on and off time that needs to be slow compared to the Dark-Bright energy splitting. The non-adiabatic coupling to the bright state is of the order of $(\Omega_p/T_{rise}\Omega_c)$, with T_{rise} being a characteristic rise time, giving to a probability of leakage to the bright state of $(\Omega_p/\Omega_c)^6$.

Spontaneous emission from the excited level $|r\rangle$

The spontaneous emission rate from $5^2S_{1/2}, F = 2$ to $F = 1$ level is very small. The error $\sim (\frac{\Omega_p}{\Omega_c})^2\gamma_r\tau$, with γ_r the spontaneous emission rate from the excited state $|r\rangle$.

9.4 Conclusion

There are several advantages of the scheme for implementing quantum gates. The coherent nature of the operations ensure high fidelity gate operations with high spatial resolution. The scheme works with very little probability of spontaneous emission as the excited state population is zero in the ideal case.

Two qubit gates may benefit from the possibility of qubits being placed closer to each other.

Chapter 10

Future work

10.1 Part I

Here we discuss future works. We have demonstrated a measure of collective effects in very dilute ultracold atom samples in a regime that has not been explored before. The excited cloud showed signatures of superradiance and subradiance. There is a lot of scope for improvement though. First, directional effects mentioned in Chapter 5 can be studied by placing the photon counter at varying angles possibly mapping a 360° radiation profile. Collective effects can be studied in 2-D or 3-D optical lattices. An immediate aim could be a sharper control of pulse intensities to achieve a higher excitation fraction and possibly an inverted sample along with a better control of optical depths, atom number and cloud size. The experimental aspects can be improved by using a Multi-channel scalar counting module that can speed up the data acquisition process.

On a fundamental level we can study collective effects in few atom samples. Extension of our results to mesoscopic ultracold clouds, with atom numbers in the range of 100-1000 would be very interesting. Such a mesoscopic system can be studied by loading the atoms to a far-off-resonant dipole trap, which is formed by focusing a detuned laser overlapping with the MOT. By moving one of the mirrors of the

focusing optics, the beam size at the focus, and therefore the size of the trap, can be precisely controlled. This would allow independent control of the number (N) and density (n) of atoms in the trap. Such highly controlled mesoscopic systems will likely allow for better probing of many of the physics that we have explored in this paper, including the superradiance-to-subradiance transition.

Subradiant states have gained renewed attention over the last decade since they are less susceptible to decoherence and can provide a robust framework for quantum information processing. Our work experimentally shows that such states can, in principle, be prepared even in the large-sample, very dilute limit.

Collective effects could be studied more systematically in optical lattices where exact spacing between atoms can be controlled in a precise manner [83]. Making an estimate of the prepared state with exact phases has been a problem for our simple set-up. With precise control of positions in a lattice a better estimate of the initial state can be obtained enabling a better understanding of the physical processes involved.

10.2 Part II: Nanoscale Quantum gates

As of now we are working towards implementing a localization protocol for single atoms in a dipole trap. As mentioned in Chapter 7 we were limited by beam power in the dipole trap beam. We are looking to use a fiber amplifier to achieve beam powers of $\sim$ 1 W, a significant improvement on the 150 mW that we have at the moment. The localization protocol can be implemented in a pair of single atom dipole traps or in a 1-D optical lattice. Once we have demonstrated localization we can implement the phase qubit protocol. A long term goal will be a neutral atom qubit array that uses Dark state of the EIT to carry out fast and efficient gate operations. Coherent operations of quantum gates with low dephasing rates are going to be vital

components of quantum computers and quantum devices. Further progress requites two qubit operations that can also be implemented using dark state protocols [65].

Apart from quantum computing dark state based localization protocols can have applications in subwavelength imaging in biology and high resolution lithography and as mentioned before the dark state based protocol can be adapted to other quantum systems like solid state spin qubits or NV centers in diamond.

Quantum computers with neutral atoms may or may not become a reality as there are other candidates with their own advantages and disadvantages. However, precise control of quantum states and measurements can help us have a better understanding and appreciation of the beauty in the quantum world.

Appendix A

Experiments using EMCCD camera

In this section we look at some early experiments conducted in our lab. These experiments were carried our using high N.A optics and EMCCD camera. A discussion of EMCCD camera is carried out in Appendix D. EMCCD cameras are fascinating tools with highly sensitive CCDs cooled down to -20^0C to reduce electronic dark noise. Though it is an excellent device for low signal imaging, using it for time resolved measurements is a fairly inefficient. Here we report a protocol for observing superradiance and subradiance using EMCCD and some results that showed both superradicance and subradiance.

The problems in using EMCCD camera is fairly obvious. Though it is a fairly sensitive device it needs to be triggered for every point on the time axis for the decay curve. This, is to be done several hundreds of times for averaging and obtaining a satisfactory signal to noise ratio. We have, however, observed superradiance and subradiance in the data we obtained.

The data is fit to a time varying decay rate. We observe (A.2) an early time constant of $\sim 9ns$, which is clearly superradiant. The system becomes subradiant at later times showing decay timescales of around $\sim 35ns$. Apart from the inefficient

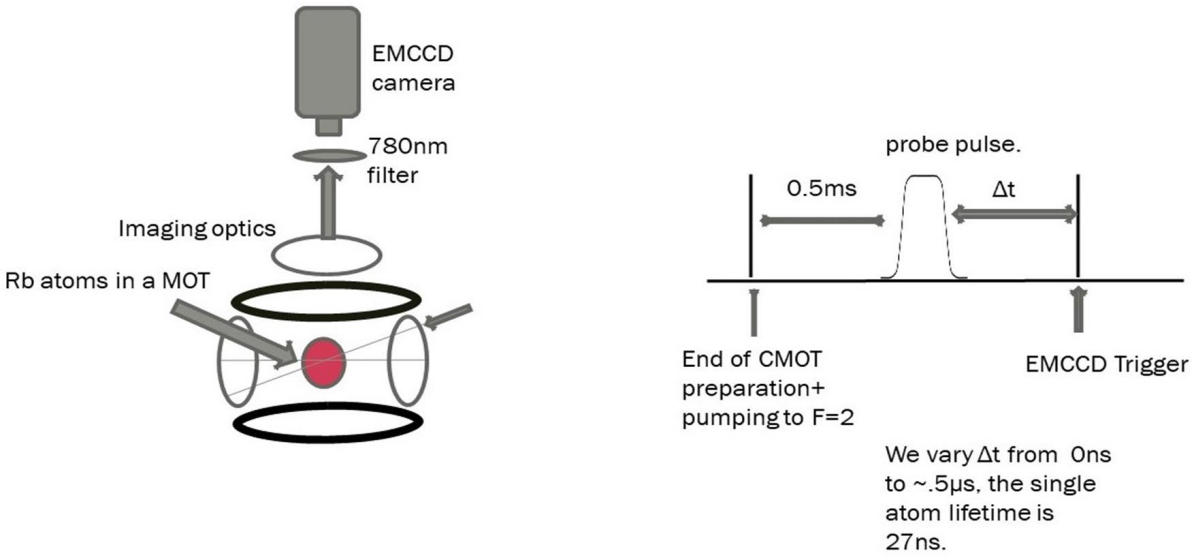

FIGURE A.1: A schematic for experiment using EMCCD

data acquisition process, the EMCCD has other issues.

The EMCCD readout seems to have "remnants" of signal the sensor possibly received before it was triggered to take data. Thus the sensor data seems to have an offset that cannot be determined.

We found that the offset signal is present only when the sensor was exposed to a source of significant brightness,like fluorescence from the MOT, inevitable during the MOT loading cycle, but we could not be sure whether some offset noise is present during exposure to weaker signals or not. If the offset remains constant over time, it can just be subtracted from the final data. We could not ensure that the offset was a constant and not time varying.Protecting the sensor from exposure using shutters and beam blocks significantly reduced the offset. For our analysis we assumed the offset to be constant as our analysis is over a period of just a microsecond. We did not expect the offset to vary a lot over that period.

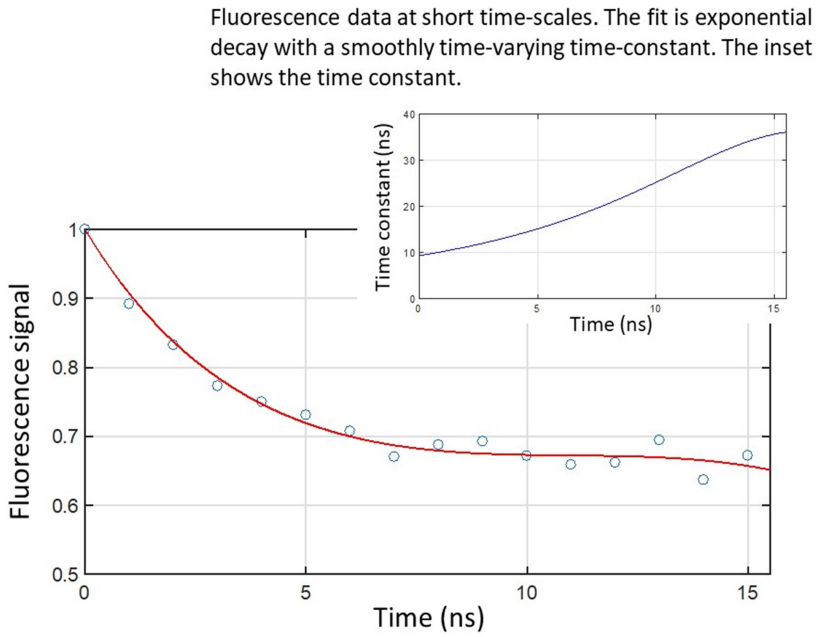

FIGURE A.2: The data is fit to a time varying decay rate, showing The data is fit to a time varying decay rate, showing an early time constant of $\sim 9ns$, which is clearly superradiant. The system becomes subradiant at later times.

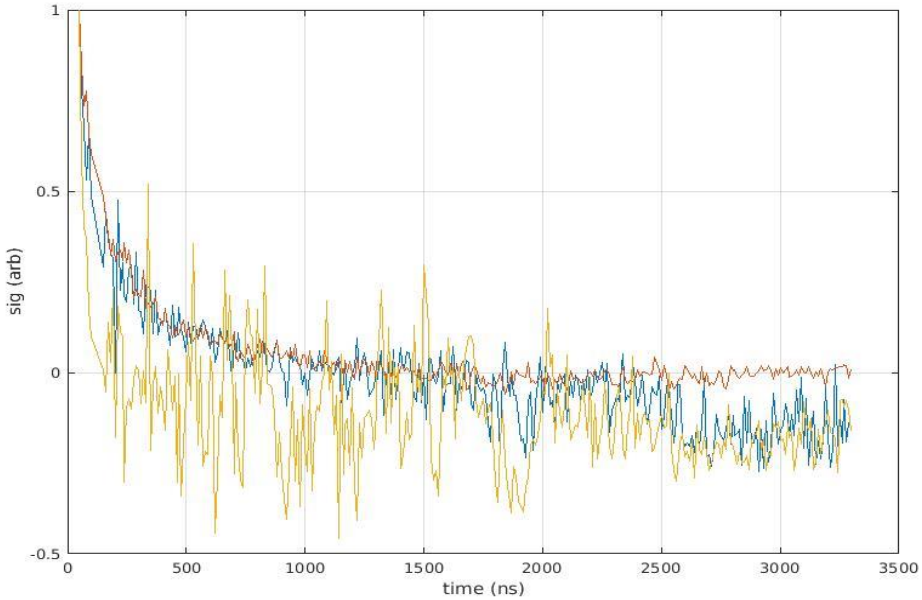

FIGURE A.3: EMCCD raw data taken for long time.

Appendix B

Photon counting module

B.1 Functioning

We use an Excelitas SPCM-AQRH-11 photon counting module. The following must be kept in mind to ensure smooth operation of the module and also keep it safe.

The digital OUTPUT pulse (BNC connector, TTL levels, ¿1.5V) should be terminated into a 50Ω load to avoid distortion and ringing. A 1.0V triggering level is recommended on counters and oscilloscopes to avoid triggering on noise. For observing the signal in an oscilloscope we use a 50Ω termination resistor.

The GATE input (BNC connector) impedance is 50Ω and is internally connected to the +5 volt supply through a 50Ω pull-up resistor (standard module versions). It can be driven by standard TTL level signals. The gate drive must be capable of sinking 100 mA to gate the module "off" (5V/ 50Ω). The Quantum Control QC95 Pulse Generator TTL pulses are not able to drive the required current. A Buffer circuit needs to be used. Counting is enabled at TTL high and disabled at TTL-low.

Saturation: The photon count decreases at higher incoming light levels. The saturation counts may appear on the scope as a train of pulses spaced by $\sim 22ns$. The count at which the output rate starts to decrease is called the saturation point. If the module is exposed to intense light the count rate will fall to zero. While the

module is protected against light overload, precautions should be taken to avoid any excessive light level. After an over exposure, the dark count of the module could increase temporarily for up to an hour. We carry out our experiments in a dark room and cover up the path between the chamber and fiber as much as possible.

B.2 Calibrating pulse delay

We have a finite delay between the time a photon event is initiated in the counter and it's detection in the DAQ. The delay is due to several factors like building up of photon pulse current in the detector, time taken for the pulse to travel the length of fiber, etc. The delay was found to be around $36ns$ with an error of $\pm 2ns$. The correction needs to be made in the data by a simple shift in the time axis.

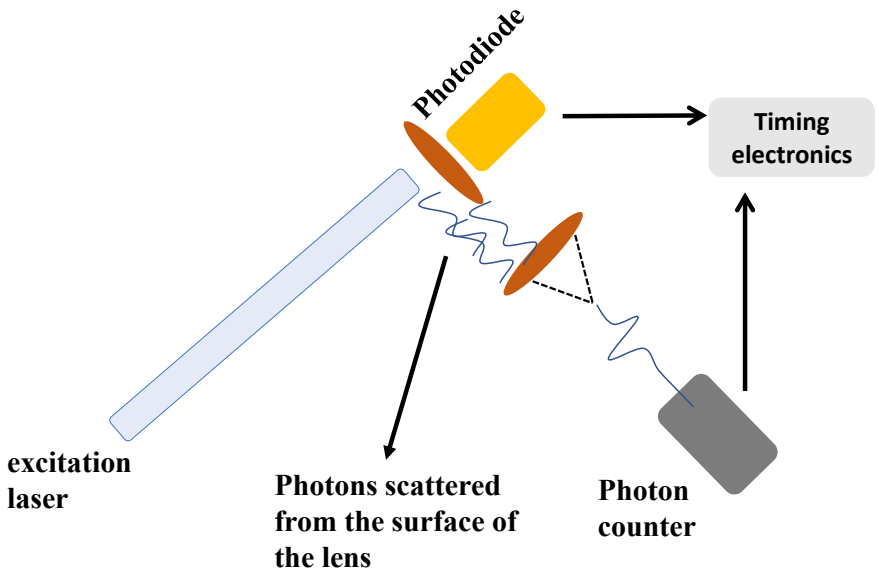

FIGURE B.1: A schematic for calibrating photon counter delay.

To measure the delay we have set-up similar to Fig. B.1. We send a laser pulse to a Photodiode. A converging lens focuses the beam into the diode. Photons scattered off the surface of the lens is detected by the photon counter. Over several hundreds of cycles of pulses we replicate a pulse shape upon integrating the photon counter signal. The lag between the pulse measured in the photodiode and that of the integrated photon counter signal is a good measure of the delay. The delay was found to be around $36ns$ with an error of $\pm 2ns$. The correction needs to be made in the data by a simple shift in the time axis.

Appendix C

MOT/dipole trap parameters

In this section we discuss measurement of number of atoms in a MOT or dipole trap using fluorescence techniques and measuring cloud temperature using Time of flight technique.

C.1 Atom number calculation

We use standard fluorescence imaging techniques to estimate the number of atoms in dipole trap or MOT/CMOT. The protocol is to shine resonant light of intensity greater than saturation intensity on the atoms for a certain duration. We theoretically estimate the photon scattering rate. Radiation is emitted independently by atoms isotropically at a fixed rate. We collect a fraction of the emitted photons as the collectiopn optics not not cover the entire $4\pi steradians$. We estimate the number of scattered photons in the duration of the pulse and take into account losses due to optics in between as well as quantum efficiency of the EMCCD camera at that wavelength.

We use a retroreflected imaging beam of power 180 and $1/e^2$ diameter of $0.9mm$

$\Gamma_{sc} = \frac{s}{1+s^2+4(\frac{\Delta}{\gamma})^2}$

We have a lens of diameter 4 inches at a distance of 17cms from the cloud. Only about 90% of the lens can be used for collecting light. This gives a solid angle of

.036 steradians, about 2% of the total solid angle (we call it the $collectionfraction$). The exposure time τ_{exp} is the time duration for which photons are collected. We also assume losses of 50% ($lossfraction$). So a straightforward counting calculation can be carried out as follows

Number of photons emitted by the cloud in the duration of excitation that reach the EMCCD sensor

$N_{photons}$ =N$_{atoms} * \Gamma_{sc} * \tau_{exp} * collectionfraction * lossfraction$

At $780nm$, the quantum efficiency of the detector is 50%, i.e one photoelectron is emitted for two photons. Number of photo-electrons emitted per atom in the given exposure time

N_{pe} =N$_{photons} * quantumefficiency$

At EMCCD gain zero 1.6 photo-electrons give 1 count. We read the total EMCCD counts (N_{counts}) from the camera software. $N_{counts} = N_{pe}/1.6$

Therefore we can estimate the number of atoms from the number of counts

N_{atoms} = (N$_{counts}$*1.6)/(Γ_{sc}*τ_{exp}*$collectionfraction$*$lossfraction$*$quantumefficiency$)

Of course, N_{counts} is the background subtracted number of counts.

C.2 Measuring temperature of atoms in a MOT/dipole trap

The temperature of the cloud is estimated by the time-of-flight technique. The cloud is released from all trapping beams and fields and is allowed to expand freely The radius of the cloud is measured by the EMCCD camera at each time interval. Usually this measurement interval is $1ms$. The cloud radius is measured by fitting the EMCCD fluorescence image with a Gaussian. The current imaging set-up has a magnification of 0.9 that has to be taken into account.

We measure cloud radius as a function of time. The data can be fit the function $R(t)^2 = R(t=0)^2 + \frac{k_B T}{m} t^2$

where R is the radius, k_B the Boltzmann constant and m is the mass of the atom. The slope of $R(t)^2$ vs t^2 is then used to estimate the temperature. The method can be used for both the CMOT and dipole trap.

Bibliography

[1] J.Dalibard and C.Cohen-Tannoudji *Laser cooling below the Doppler limit by polarization gradients: simple theoretical models*, J. Opt. Soc. Am. B Vol. 6, No. 11/November (1989)

[2] Metcalf, Harold J., Straten, Peter van der *Laser Cooling and Trapping*. (1999)

[3] R. H. Dicke, *Coherence in Spontaneous Radiation Processes*, Phys. Rev. **93**, 99 (1954).

[4] M. Gross and S. Haroche, *Superradiance: An Essay on the Theory of Collective Spontaneous Emission*, Physics Reports **93**, 301 (1982).

[5] E. Wolfe and S. F. Yelin, *Certifying Separability in Symmetric Mixed States of N Qubits, and Superradiance*, Phys. Rev. Lett. **112**, 140402 (2014).

[6] R. T. Sutherland and F. Robicheaux, *Coherent Forward Broadening in Cold Atom Clouds*, Phys. Rev. A **93**, 023407 (2016).

[7] I. E. Mazets and G. Kurizki, *Multi-atom Cooperative Emission Following Single Photon Absorption: Dicke-State Dynamics*, J. Phys. B: At. Mol. Opt. Phys. **40**, F105 (2007).

[8] N. Skribanowitz, I. P. Herman, J. C. MacGillivray, and M. S. Feld, *Observation of Dicke Superradiance in Optically Pumped HF Gas*, Phys. Rev. Lett. **30**, 309 (1973).

[9] R. Friedberg, S. R. Hartmann, and J. T. Manassah, *Frequency Shifts in Emission and Absorption by Resonant Systems of Two-level Atoms*, Phys. Rep. **7**, 101 (1973).

[10] W. Guerin, M. O. Araujo, and R. Kaiser, *Subradiance in a Large Cloud of Cold Atoms*, Phys. Rev. Lett. **116**, 083601 (2016).

[11] P. Weiss, M. O Araujo, R. Kaiser and W. Guerin, *Subradiance and Radiation Trapping in Cold Atoms*, New J. Phys. **20**, 063024 (2018).

[12] B. Lemberger and D. D. Yavuz, *Effect of Correlated Decay on Fault-tolerant Quantum Computation*, Phys. Rev. A **96**, 062337 (2016).

[13] B. McGuyer, M. McDonald, G. Iwata *et al.*, *Precise Study of Asymptotic Physics with Subradiant Ultracold Molecules*, Nature Phys. **11**, 32 (2015).

[14] R. G. DeVoe and R. G. Brewer, *Observation of Superradiant and Subradiant Spontaneous Emission of Two Trapped Ions*, Phys. Rev. Lett **76**, 2049 (1996).

[15] D. Pavolini, A. Crubellier, P. Pillet, L. Cabaret, and S. Liberman, *Experimental Evidence for Subradiance*, Phys. Rev. Lett. **54**, 1917 (1985).

[16] P. Solano, P. Barberis-Blostein, F. K. Fatemi, *et al.*, *Super-radiance Reveals Infinite-range Dipole Interactions Through a Nanofiber*, Nat. Commun. **8**, 1857 (2017).

[17] S. D. Jenkins, J. Ruostekoski, N. Papasimakis, S. Savo, and N. I. Zheludev, *Many-Body Subradiant Excitations in Metamaterial Arrays: Experiment and Theory*, Phys. Rev. Lett. **119**, 053901 (2017).

[18] P. Wolf, S.C. Schuster, D. Schmidt, S. Slama, and C. Zimmermann, *Observation of Subradiant Atomic Momentum States with Bose-Einstein Condensates in a Recoil Resolving Optical Ring Resonator*, Phys. Rev. Lett. **121**, 173602 (2018).

[19] S.J. Roof *et al.*, *Observation of Single-Photon Superradiance and the Cooperative Lamb Shift in an Extended Sample of Cold Atoms*, Phys. Rev. Lett. **117**, 073003 (2016).

[20] S. L. Bromley *et al.*, *Collective Atomic Scattering and Motional Effects in a Dense Coherent Medium*, Nat. Commun. bf 7, 11039 (2016).

[21] C. Bradac, M. T. Johnsson, M. V. Breugel, *et al.*, *Room-temperature Spontaneous Superradiance From Single Diamond Nanocrystals*, Nat. Commun. **8**, 1205 (2017).

[22] A. Angerer, K. Streltsov, T. Astner, T. *et al.*, *Superradiant Emission From Color Centres in Diamond*, Nat. Phys. **14**, 1168 (2018).

[23] Z. Wang *et al.*, *Controllable Switching Between Superradiant and Subradiant States in a 10-qubit Superconducting Circuit*, Phys. Rev. Lett. **124**, 013601 (2020).

[24] M. O. Scully and A. A. Svdzinsky, *The Super of Superradiance*, Science **325**, 1510 (2009)

[25] M. O. Scully, E. S. Fry, C. H. Raymond Ooi, and K. Wódkiewicz, *Directed Spontaneous Emission from an Extended Ensemble of N Atoms: Timing Is Everything*, Phys. Rev. Lett **96**, 010501 (2006).

[26] E. Akkermans, A. Gero, and R. Kaiser, *Photon Localization and Dicke Superradiance in Atomic Gases*, Phys. Rev. Lett. **101**, 103602 (2008).

[27] A. A. Svidzinsky, J.-T. Chang, and M. O. Scully, *Cooperative Spontaneous Emission of N Atoms: Many-body Eigenstates, the Effect of Virtual Lamb shift Processes, and Analogy with Radiation of N Classical Oscillators*, Phys. Rev. A **81**, 053821 (2010).

[28] A. A. Svidzinsky and J.-T. Chang, *Cooperative Spontaneous Emission as a Many-Body Eigenvalue Problem*, Phys. Rev. A **77**, 043833 (2008).

[29] H. Cai, D.-W. Wang, A. A. Svidzinsky, S.-Y. Zhu, and M. O. Scully, *Symmetry Protected Single Photon Subradiance*, Phys. Rev. A **93**, 053804 (2016).

[30] P. A. Vetter *et al.*, *Single Photon Subradiance and Superradiance Revisited: a Group Theoretic Analysis of Subradiant States*, Phys. Scr. **91**, 023007 (2016).

[31] F. Cottier, R. Kaiser, and R. Bachelard, *Role of Disorder in Super-and Subradiance of Cold Atomic Clouds*, Phys. Rev. A **98**, 013622 (2018).

[32] M. O. Araujo, W. Guerin, and R. Kaiser, *Decay Dynamics in the Coupled-Dipole Model*, J. of Modern Opt. **65**, 1345 (2018).

[33] W. Guerin, M. T. Rouabah, and R. Kaiser, *Light Interacting with Atomic Ensembles: Collective, Cooperative and Mesoscopic Effects*, J. of Modern Opt. **64**, 895 (2017).

[34] W. Guerin and R Kaiser, *Population of Collective Modes in Light Scattering by Many Atoms*, Phys. Rev. A **95**, 053865 (2017).

[35] T. Bienaime, M. Petruzzo, D. Bigerni, N. Piovella, and R. Kaiser, *Atom and Photon Measurement in Cooperative Scattering by Cold Atoms*, J. of Modern Opt. **58**, 1942 (2011).

[36] J. H. Eberly, *Emission of One Photon in an Electric Dipole Transition of One Among N Atoms*, J. Phys. B **39**, S599 (2006).

[37] T. Bienaime, N. Piovella, and R.Kaiser, *Controlled Dicke subradiance from a large cloud of two-level systems*, Phys. Rev. Lett. **108**, 123602 (2012).

[38] M. O. Scully, *Collective Lamb Shift in Single Photon Dicke Superradiance*, Phys. Rev. Lett. **102**, 143601 (2009).

[39] M. O. Scully, *Single Photon Subradiance: Quantum Control of Spontaneous Emission and Ultrafast Readout*, Phys. Rev. Lett. **115**, 243602 (2015).

[40] A. A. Kalachev and V. V. Samartsev, *Quantum Memory and Quantum Computations in the Optical Subradiance Regime*, Quantum Electron. **35**, 679 (2005).

[41] V. V. Temnov and U. Woggon, *Superradiance and Subradiance in an Inhomogeneously Broadened Ensemble of Two-Level Systems Coupled to a Low-Q Cavity*, Phys. Rev. Lett. **95**, 243602 (2005).

[42] P.-O. Guimond, A. Grankin, D.V. Vasilyev, B. Vermersch, and P. Zoller, *Subradiant Bell States in Distant Atomic Arrays*, Phys. Rev. Lett. **122**, 093601 (2019).

[43] A. Asenjo-Garcia, M. Moreno-Cardoner, A. Albrecht, H.J. Kimble, and D. E. Chang, *Exponential Improvement in Photon Storage Fidelities Using Subradiance and selective radiance in Atomic Arrays*, Phys. Rev. X **7**, 031024 (2017).

[44] S. D. Jenkins and J. Ruostekoski, *Controlled Manipulation of Light by Cooperative Response of Atoms in an Optical Lattice*, Phys. Rev. A **86**, 031602 (2012).

[45] D. Plankensteiner, L. Ostermann, H. Ritsch, and C. Genes, *Selective Protected State Preparation of Coupled Dissipative Quantum Emitters*, Sci. Rep. **5**, 16231 (2015).

[46] R. J. Bettles, S. A. Gardiner, and C. S. Adams, *Cooperative Ordering in Lattices of Interacting Two-Level Dipoles*, Phys. Rev. A **92**, 063822 (2015).

[47] R. J. Bettles, S. A. Gardiner, and C. S. Adams, *Cooperative Eigenmodes and Scattering in One-Dimensional Atomic Arrays*, Phys. Rev. A **94**, 043844 (2016).

[48] G. Facchinetti, S. D. Jenkins, and J.Ruostekoski, *Storing Light with Subradiant Correlations in Arrays of Atoms*, Phys. Rev. Lett. **117**, 243601 (2016).

[49] H. Zoubi and H. Ritsch, *Metastability and Directional Emission Characteristics of Excitons in 1D Optical Lattices*, Europhys. Lett. **90**, 23001 (2010). .

[50] H. Zoubi and H. Ritsch, *Lifetime and Emission Characteristics of Collective Electronic Excitations in Two-Dimensional Optical Lattices*, Phys. Rev. A **83**, 063831 (2011).

[51] D. F. Kornovan, A. S. Sheremet, and M. I. Petrov, *Collective Polaritonic Modes in an Array of Two-Level Quantum Emitters Coupled to an Optical Nanofiber*, Phys. Rev. B **94**, 245416 (2016).

[52] S. Prasad and R. J. Glauber, *Polarium Model: Coherent Radiation by a Resonant Medium*, Phys. Rev. A **61**, 063814 (2000).

[53] D. Bhatti, R. Schneider, S. Oppel and J. von Zanthier , *Directional Dicke Subradiance with Nonclassical and Classical Light Sources*, Phys. Rev. Lett. **120**, 1136 (2018).

[54] R. Wiegner, J. von Zanthier, and G. S. Agarwal, *Quantum-interference-initiated Superradiant and Subradiant Emission from Entangled Atoms*, Phys. Rev. A **84**, 023805 (2011).

[55] C. E. Maximo, R. Bachelard, F. E. A. dos Santos, and C. J. Villas-Boas, *Cooperative Spontaneous Emission via Renormalization Approach: Classical Versus Semi-Classical Effects*, arXiv:1906.05719 (2020).

[56] A. Lagendijk, B A van Tiggelen, *Resonant Multiple scattering of light*, Phys. Rep. 270143–215 (1996)

[57] N. A. Proite, Z. J. Simmons, and D. D. Yavuz, *Observation of Atomic Localization Using Electromagnetically Induced Transparency*, Phys. Rev. A **83**, 041803(R) (2011).

[58] J. A. Miles, Z. J. Simmons, and D. D. Yavuz, *Subwavelength Localization of Atomic Excitation Using Electromagnetically Induced Transparency*, Phys. Rev. X **3**, 031014 (2013).

[59] B. E. Unks, N. A. Proite, and D. D. Yavuz, *Generation of High-Power Laser Light with GHz Splitting*, Rev. Sci. Instrum. **78**, 083108 (2007).

[60] S. Utsunomiya, C. P. Master, and Y. Yamamoto, *Algorithm-Based Analysis of Collective Decoherence in Quantum Computation*, J. Opt. Soc. Am. B **24**, 198 (2007).

[61] I. M. Sokolov, M. D. Kupriyanova, D. V. Kupriyanov, and M. D. Havey, *Light Scattering From a Dense and Ultracold Atomic Gas*, Phys. Rev. A **79**, 053405 (2009).

[62] L. H. Pedersen and K. Molmer, *Few Qubit Atom-Light Interfaces with Collective Encoding*, Phys. Rev. A **79**, 012320 (2009).

[63] Y. Yamamoto and A. Imamoglu, *Mesoscopic Quantum Optics* (John Wiley & Sons, 1999).

[64] Diptaranjan Das, B. Lemberger, and D. D. Yavuz, *Subradiance and superradiance-to-subradiance transition in dilute atomic clouds*, arxiv: 2001.09946

[65] A. V. Gorshkov, et al, *Coherent Quantum Optical Control with Subwavelength Resolution*, Phys. Rev. Lett. 100, 093005 (2008).

[66] D.D.Yavuz and N.A.Proite, *Nanoscale resolution fluorescence microscopy using electromagnetically induced transparency*, Phys. Rev. A76, 041802(R)(2007)

[67] J.Cho, *Addressing Individual Atoms in Optical Lattices with Standing-Wave Driving Fields*, Phys. Rev. Lett.99, 020502 (2007)

[68] J. A. Miles, Z. J. Simmons, and D. D. Yavuz, Localization of Atomic Excitation Using Electromagnetically Induced Transparency Phys. Rev X 3, 031014 (2013).

[69] M. Paternostro, *Localize and Conquer*, Physics 6, 99 (2013).

[70] J. A. Miles, Diptaranjan Das, Z. J. Simmons, and D. D. Yavuz,*Localization of Atomic Excitation Beyond the Diffraction Limit Using Electromagnetically Induced Transparency*, Phys. Rev. A 92, 023838 (2015).

[71] G. S. Agarwal and K. T. Kapale, *Subwavelength Atom Localization via Coherent Population Trapping*, J. Phys. B: At. Mol. Opt. Phys. 39, 3437 (2006).

[72] D. D. Yavuz and N. A. Proite, *Nanoscale Resolution Fluorescence Microscopy Using Electromagnetically Induced Transparency*, Phys. Rev. A 76, 041802(R) (2007).

[73] H. Li, V. A. Sautenkov, M. M. Kash, A. V. Sokolov, G. R. Welch, Y. V. Rostovtsev, M. S. Zubairy, and M. O. Scully, Imaging Beyond the Diffraction Limit via Dark States, Phys. Rev. A 78, 013803 (2008).

[74] N. A. Proite, Z. J. Simmons, and D. D. Yavuz, *Observation of Atomic Localization Using Electromagnetically Induced Transparency*, Phys. Rev. A 83, 041803(R) (2011).

[75] M. Fleischhauer, A. Imamoglu, and J. P. Marangos,*Electromagnetically Induced Transparency: Optics in Coherent Media*, Rev. Mod. Phys. 77, 633 (2005).

[76] M.A.Nielsen and I.L.Chuang, *Quantum Computation and Quantum Information (Cambridge University Press, 2000).*

[77] F. Jendrzejewski et. al. *Subwavelength-width optical tunnel junctions for ultracold atoms*, Phys. Rev. A 94, 063422 (2016).

[78] K.T.Kapale and G.S.Agarwal, *Subnanoscale resolution for microscopy via coherent population trapping*, Opt. Lett. 35, 2792 (2010).

[79] D. E. Chang, J. D. Thompson, H. Park, V. Vuletić, A. S. Zibrov, P. Zoller, and M. D. Lukin, *Trapping and Manipulation of Isolated Atoms Using Nanoscale Plasmonic Structures* Phys. Rev. Lett. 103, 123004 (2009).

[80] M. Lacki, M. Baranov, H. Pichler, and P. Zoller, *Nanoscale "Dark State" Optical Potentials for Cold Atoms*, Phys. Rev. Lett. 117, 233001 (2016)

[81] Jared Miles, PhD thesis UW Madison. (available at *http://yavuzlab.physics.wisc.edu*)

[82] Yale et al. *All-optical control of a solid-state spin using coherentdark states*, PNAS May 7, 110 (19) 7595-7600 (2013).

[83] Jun Rui *et. al. A subradiant optical mirror formed by a single structured atomic layer* arxiv: 2001.00795 (2020).